Master of Science Thesis

Coherent Structures at the Serrated Trailing-Edge of a NACA 0012

Stefan Pröbsting

June 14, 2011

Aerodynamics

Faculty of Aerospace Engineering

TU Delft

Delft University of Technology

Coherent Structures at the Serrated Trailing-Edge of a NACA 0012

Master of Science Thesis

For obtaining the degree of Master of Science in Aerospace Engineering
at Delft University of Technology

Stefan Pröbsting

June 14, 2011

Faculty of Aerospace Engineering · Delft University of Technology

Delft University of Technology

DELFT UNIVERSITY OF TECHNOLOGY
DEPARTMENT OF AERODYNAMICS

The undersigned hereby certify that they have read and recommend to the Faculty of Aerospace Engineering for acceptance the thesis entitled **"Coherent Structures at the Serrated Trailing-Edge of a NACA 0012"** by **Stefan Pröbsting** in fulfillment of the requirements for the degree of **Master of Science**.

Dated: June 14, 2011

Supervisors:

Prof. dr. F. Scarano

dr. ir. B. van Oudheusden

S. Ghaemi, MSc

Preface

I would like to dedicate this thesis to my family for having supported me over the course of the past five years that it took me to become an engineer. I am grateful to Wenjing for coping with the unavoidable frustration during the work on the thesis.

Furthermore, I would like to thank Prof. Scarano for his supervision and giving me the opportunity to start the work on this thesis at a relatively early stage of the MSc program. This work was embedded in the studies of Sina, who shared his experience during the preparation of the experiments and the numerous hours we spent in the wind-tunnel. Especially, I am grateful for the extensive introduction to the various kinds of PIV.

Finally, I'd like to thank the technical staff at the aerodynamics department for their support with the instrumentation of the models and set-up of the experiments, and the DelFly team for providing the hot-wire cutting machine.

Working on this thesis to conclude my studies with the up-to-date knowledge and technology available in Delft has been a valuable and rewarding experience.

Summary

In the past, different modifications of trailing-edges have been investigated with the aim to reduce noise emissions. One promising solution, which has been shown to reduce the intensity of trailing-edge noise, is the application of so-called sawtooth serrations with different proportions and sizes. Current research aims at applying new tools of flow field interrogation, first of all tomographic PIV, to the problem of trailing-edge noise and at creating links between the phenomenological description of the flow field in terms of coherent structures and noise spectra in order to improve understanding of the noise generating mechanisms. In the framework of this thesis, sawtooth serrations applied to a NACA 0012 airfoil have been investigated and compared to the straight trailing-edge of the unmodified NACA 0012 baseline model. Acoustic far-field, surface pressure and a series of PIV measurements have been performed for this purpose.

In a first step, acoustic far-field measurements on a large selection of serrated models have been performed. On one hand, tonal narrowband noise associated to the shedding of vortices from the blunt parts of the trailing-edge poses a large penalty for the reduction in overall sound pressure level. On the other hand, the acoustic measurements have indicated a small reduction in noise level originating from the serrated trailing-edge for frequencies in the broadband spectrum exceeding the tonal range, which is in agreement with Howe's theory of trailing-edge noise. Overall, a decrease in total sound pressure level could not be observed.

In a second step, PIV measurements of the boundary layer close to the trailing-edge have been performed in order to identify a subset of coherent structures, which can be linked to the production of noise and in particular to the the production of tonal noise. Large coherent structures appearing close to the trailing-edge or in between the serrations have been visualized, dominate in terms of vorticity level and show the shape of horseshoe vortices. Most of these structures show a large spanwise coherence on the order of the distance between two serrations and reappear at the frequency of the tonal noise. This suggests a link between this category of coherent structures and the tonal noise observed in the acoustic spectra.

Table of Contents

List of Figures

List of Tables

List of Symbols

Abbreviations

BTE	Blunt trailing-edge
DNS	Direct numerical simulation
FFT	Fast Fourier Transform
LSM	Large scale motion
PIV	Particle image velocimetry
PSD	Power spectral density
SPL	Sound pressure level
TBL	Turbulent boundary layer
TE	Trailing-edge
VDR	Velocity dynamic range

Greek symbols

α	Angle of attack
δ	Boundary layer thickness
δ_ν	Viscous wall unit
$\delta^\star$	Boundary layer displacement thickness
Δt	Time separation
Δx	Pixel shift
δ_z	Depth of field
λ	Distance from tip to tip of a serration
λ	Wavelength of light
λ_a	Acoustic wavelength
μ	Dynamic viscosity
ν	Kinematic viscosity
Ω	Asymmetric component of velocity gradient tensor
ω	Angular frequency
Φ	Angle between the freestream vector and the serration edge
ρ	Correlation coefficient
ρ	Fluid density
ρ_p	Particle density

σ	Eigenvalue of velocity gradient tensor
τ_s	Relaxation time
θ	Boundary layer momentum thickness

Roman symbols

$\mathbf{a}$	Local acceleration of fluid parcel
a	Speed of sound
c	Airfoil chord length
d_{diff}	Diffraction limited image diameter
d_i	Distance between sensor and lens
d_o	Distance between object in focus and lens
d_p	Particle diameter
d_τ	Diameter of particle image
f	Focal length
f	Frequency
$f_\#$	Numerical aperture
H	Distance from root to tip of a serration
h	Half of the distance from root to tip of a serration
$\mathbf{k}$	Wavenumber vector
L	Characteristic length
L	Wetted span
l_3	Turbulence correlation length
M	Mach number
M	Optical magnification
p	Static pressure
p_0	Reference pressure
p_{ref}	Reference pressure
R	Correlation function
r	Distance between source and observer
Re	Reynolds number
S	Symmetric component of velocity gradient tensor
SPL	Sound pressure level
St	Stokes number
St	Strouhal number
T	Measurement time
t	Trailing edge thickness
T_{deform}	Deformation time
T_{diff}	Diffusion time
U	Velocity
U_c	Characteristic eddy convection velocity
U_∞	Freestream velocity

u^+	Velocity in inner scaling
u_τ	Wall friction velocity
y^+	Wall-normal coordinate in inner scaling

Chapter 1

Introduction

Aviation noise is an increasing problem in today's society. The ever increasing demand for fast transportation of goods and for travelling to far or remote places leads to an annual increase in the number of flights. Along with this trend comes the need for expansion of global transportation hubs, large airports located in the vicinity of or even close to the center of large metropolitan areas, which have to increase their capacity in terms of take-offs and landings. Unfortunately, it happens nowadays that aircraft reach a peak of noise emittance during these two phases of flight where high-lift devices are used and the landing gear is deployed. Furthermore, the aircraft's trajectory passes unavoidably through the vicinity of urban areas at moderate height. Finally, the exposure to noise audible in the cabin of an airliner during cruise flight is a well-known nuisance to every passenger.

Besides aviation, noise is a problem in the design and certification process of wind energy parks in the vicinity of urban areas. As wind turbines are nowadays widely spread in Europe, the swishing noise emitted by the rotating blades is well-known and a reason for complaints. Along with the ever denser population and need for alternative energy supply comes the necessity to build wind parks close to urban areas and therefore the need to reduce unwanted noise.

In this introduction the effect of noise on human beings and its sources in current day applications connected to the aviation and wind turbine industry are pointed out. Methodologies to reduce the noise emissions in these fields are desired and subject to present research. One particular device to reduce the trailing-edge noise of actual airfoils are so-called sawtooth serrations or chevrons. In this thesis the occurrence of coherent flow structures in the vicinity of sawtooth serrations and their possible relation to noise generation mechanisms is investigated experimentally as outlined in 1.3.

Chapter 2 starts with an overview of the source mechanisms of noise emitted from the trailing-edge of an airfoil and gives an overview of the past efforts concerned with noise reduction in this area. In chapter 3 present knowledge about coherent structures, which persist in time and

space, is cited. Chapter 4 continues with a description of the diagnostic techniques employed in the course of this thesis work, before the individual experiments and airfoil models are described in detail in chapter 5. Results are presented in chapter 6 and the conclusions are summarised in the final chapter 7.

1.1 Noise and nuisance

Noise can be defined as pressure disturbances in the form of waves, which can have a harassing effect on humans either due to their intensity or due to long term exposure. Sound waves are weak pressure perturbations travelling through media at a velocity termed the speed of sound, which is specific for the propagation medium and ambient conditions. In air at sea level the speed of sound is about $340m/s$. The propagation of sound waves can be influenced by air convection and obstacles located in the sound field. Noise intensity in free space generally decreases with the inverse square of the distance travelled. Additionally, absorption effects due to viscosity contribute to the reduction, but in general its attenuation by viscous effects is relatively low. Therefore, aviation noise can be a serious problem in populated areas located in the vicinity of airports.

Short term exposure to noise of a high intensity or long term exposure to noise of medium intensity veritably has a detrimental effect on the health of human beings and can lead to severe disorders or permanent damage. One might think that only a small part of the population is affected by aviation noise. However, a study conducted in a relatively densely populated country, in this case Germany, has shown that a paramount 37% of its population feels harassed by aviation noise, while 7% indicate to feel heavily disturbed (see Lerch et al. (2009)). Aviation authorities, aircraft manufacturers and research institutes have realized the problems connected to aviation noise and a number of initiatives now aim for a drastic decrease of the noise level for future generations of aircraft.

1.2 Sources of noise on aircraft and wind turbines

In order to tackle the challenge of noise reduction it is of importance to identify the noise sources present on current aircraft configurations. In case of propelled flight one of the dominating noise sources is the propulsion system in the form of a jet engine, a propeller engine or a turbo-fan. In the past, turbo-fans with high by-pass ratio have led to a considerable decrease in noise levels as pointed out by Dobrzynski (2010). However, this development currently encounters its limitations posed by size and structural issues. A second major noise source is the so-called airframe noise, for instance the noise generated by the landing-gear, which can be reduced by streamlined fairings. Figure 1.1 shows the paramount examples of airframe noise for present aircraft configurations. Apart from the landing-gear also high-lift devices such as slotted slats, flaps and spoilers contribute to the noise production by various aeroacoustic source mechanisms. One of these aeroacoustic sources is the noise scattered at the trailing-edge of wings, which is subject to research in this thesis. Typically flaps are

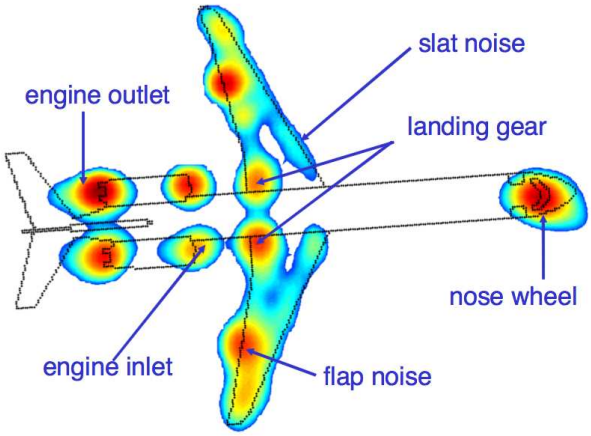

Figure 1.1: Typical sources of airframe noise [Oerlemans (2009)]

extended and large angles of attack are necessary due to relatively low velocities. Nevertheless, Reynolds numbers during the approach and landing phase based on the mean chord can be on the order of 10^6 to 10^7 for commercial airliners. A recent and comprehensive review about noise sources on aircraft and the progress made during the last four decades is given by Dobrzynski (2010).

Aviation noise is not the only nuisance that poses a challenge for the near future. A second large branch of engineering, which suffers from noise pollution, is related to wind energy, e. g. the well-known swishing noise produced by large wind turbines with its periodic re-occurrence. In the past, law suites have been opened against owners of wind farms and stringent regulations in terms of noise protection are the consequence. In order to protect people living in the vicinity of wind turbines and at the same time being able to make use of scarce land resources in the proximity of metropolitan areas, it is of importance to find ways of reducing the noise emission of next generation wind turbines. A study on the noise sources on a typical wind turbine has been conducted by Oerlemans (2009).

Figure 1.2 zooms in on a typical wing and displays the mechanisms generating noise which can be encountered for aircraft as well as wind turbines. It should be noted that the trailing-edge location is one of the major sources of noise on the wing. A large number of previous works have dealt with the prediction and reduction of noise and the identification of its sources at the trailing-edge of two-dimensional flat-plates, airfoils or three-dimensional wings.

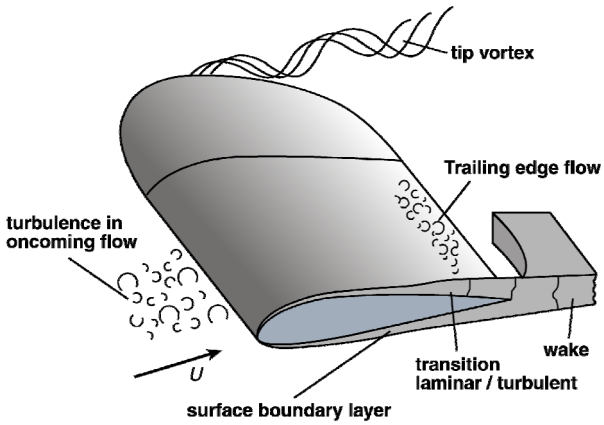

Figure 1.2: Sources of noise on a typical wing [Oerlemans (2009)]

1.3 Research objectives

In the past, different devices and modifications of trailing-edges have been investigated with the aim to reduce noise emissions. One promising solution, which has been shown to reduce the intensity of trailing-edge noise, is the application of so-called sawtooth serrations which appear in different proportions and sizes in literature and are also termed chevrons in the context of jets and nozzles. Current research aims at applying new tools of flow field interrogation (tomographic PIV) to the problem of trailing-edge noise and at creating links between the phenomenological description of the flow field in terms of coherent structures and noise spectra in order to improve understanding of the noise generating mechanisms.

In the framework of the present thesis sawtooth serrations applied to a NACA 0012 airfoil are investigated and compared to the straight trailing-edge of the unmodified NACA 0012 baseline model with respect to the presence of coherent structures. In a fist step, the noise emitted by a relatively large series of trailing-edge serrations is measured. In a second step, it is attempted to identify the coherent structures present at the serrated trailing-edge. Evidence is provided for the causal link between a subset of these structures and the production of tonal noise. Finally, correlations between surface pressure and velocity are presented and related to the coherent events identified in the second step. For this purpose, acoustic measurements are performed on a series of trailing-edge serration designs to investigate the relevance of different scaling parameters for noise generation. A second measurement campaign, restricted to a smaller number of selected designs, is investigated employing PIV for the velocity field and surface mounted microphones for the surface pressure fluctuations.

Chapter 2

Trailing-edge noise

Trailing-edge noise belongs to the sources of airframe noise on the wing of typical aircraft and wind turbines. This chapter first gives an overview and physical interpretation of the different mechanisms of noise production at the trailing-edge (section 2.1) followed by an overview of noise attenuation methods (section 2.2). Thereafter, the results of an important contribution to the theory of trailing-edge noise and resulting scaling laws, which dominant parameters, are given in section 2.3 with an emphasis on serrations. Finally, section 2.4 provides an overview of the literature dealing with trailing-edge serrations from experimental and numerical points of view.

2.1 Mechanisms of noise production at the trailing-edge

For arbitrary geometries and flow conditions there are many possible mechanisms of noise production in the vicinity of the trailing-edge, such as vortex shedding by separation, laminar boundary layer vortex shedding, blunt trailing-edge noise, turbulent boundary layer interaction noise and turbulent boundary layer trailing-edge noise. The latter one is also termed pure trailing-edge noise in Roger (2009). It arises from the fact that this source is even present for the case of an infinitely thin plate.

For the applications mentioned in chapter 1, the characteristics and mechanisms of trailing-edge noise especially at low Mach numbers are important. Wind turbines do not usually encounter flows of high Mach numbers while the flight Mach number of aircraft during take-off, approach and landing is usually limited to $M < 0.3$. Therefore, the assumption of incompressible flow is assumed to be generally valid for the cases of interest. In most cases the boundary layer experiences transition to the turbulent state.

Source mechanisms possess different characteristics in terms of magnitude, directivity and shape of the frequency spectrum of the emitted noise. In general, sources can be interpreted in

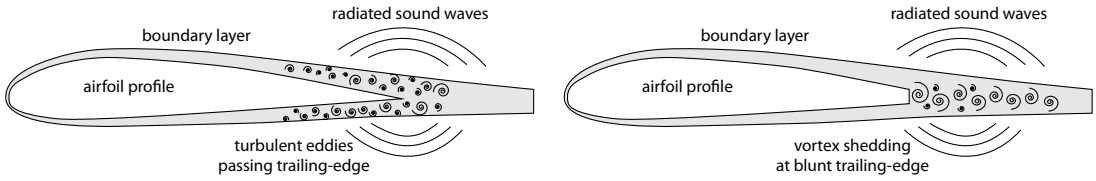

(a) TBL-TE noise (b) BTE noise

Figure 2.1: Schematics of noise sources at the trailing-edge

terms of monopoles, dipoles or quadrupoles with decreasing strength in this order as explained in basic texts on aeroacoustics such as Howe (2003) or Rienstra and Hirschberg (2004). The principle source mechanisms in this case, which are of dipole character, are listed below. Figure 2.1 shows a graphical representation.

1. Turbulent boundary layer convecting over the trailing-edge (TBL-TE noise)
2. Vortex shedding from the blunt trailing-edge (BTE noise)

While the TBL-TE (figure 2.1(a)) noise has a broadband character, meaning no distinct peak is visible in the frequency spectrum, the BTE noise is of narrowband nature centring around a dominant frequency, which is often expressed in terms of the non-dimensional Strouhal number. TBL-TE noise tends to be drowned in the presence of strong BTE noise, depending on the ratio of trailing-edge bluntness and boundary layer thickness. BTE noise has a tonal, sometimes singing character.The broadband nature of TBL-TE noise indicates the influence of various scales of turbulence, while the tonal nature of BTE noise indicates that the mechanism is associated to discrete scales and velocities. This fact makes it possible to identify the source and physical principle of BTE noise, e. g. the vortex roll-up behind blunt bodies such as cylinders as first investigated by Strouhal (1878) or behind blunt parts of the trailing-edge as depicted in figure 2.1(b). These vortices usually posses the similar or coherent length and velocity scales and introduce pressure disturbances in the flow which can be interpreted as noise sources of approximately constant frequencies.

2.1.1 Turbulent boundary layer trailing-edge noise

The problem of trailing-edge noise produced by a turbulent boundary layer convecting over the edge of an airfoil (see figure 2.2) or flat plate has frequently been subject to experimental or theoretical research. In the latter case, simplifications are introduced, such as representations of the airfoil by a semi-infinite rigid plate or half-plane. Results derived under this assumption are only valid in cases where the acoustic wavelength is relatively small compared to the chord of the airfoil, i. e. for non-compact bodies. Furthermore, due to the assumption of low Mach number flow motivated in the introduction of this chapter effects of order $O(M^2)$, which are related to compressibility effects, are usually neglected in the analysis. A comprehensive

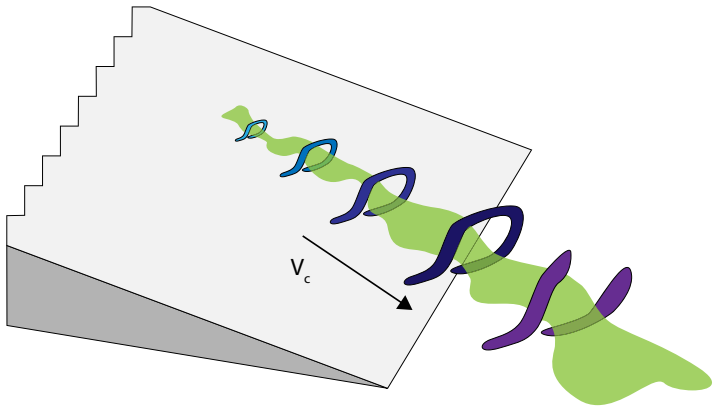

Figure 2.2: Boundary layer turbulence convecting over the trailing-edge

review on the theory of trailing-edge noise under these conditions was published by Howe (1978).

A part of the pressure fluctuations induced on the surface of the airfoil by vortices and eddies contained in the turbulent boundary layer convecting at a characteristic velocity. These structures and events in the boundary layer are often termed coherent structures and a brief overview of present knowledge is provided in chapter 3. An assumption which is often applied at this point in different theories is Taylor's hypothesis of frozen turbulence: In the vicinity of the trailing-edge the turbulence in the boundary layer is assumed to merely convect at a characteristic velocity without changing within an interval in front of and behind the trailing-edge.

Further, it is assumed that the characteristic wall pressure field can be regarded as induced by the structures in the boundary layer and convects at the same characteristic velocity near the trailing-edge. These pressure fluctuations can be described in the form of a spectrum dependent on wavenumber vector and frequency and is related to the distribution of vortices. They have been measured and modelled for locations far upstream of the trailing-edge applying for the case of an infinite flat plate, for instance by Chase (1987). A comprehensive review on the topic of pressure spectra in the turbulent boundary layer referring to both, models and experiments, was published by Bull (1996). While the flow convects over the singularity, the trailing-edge, the wall boundary condition disappears, implying a non-equilibrium situation in the fluid due to these small pressure disturbances. As a result the pressure disturbances are scattered in the form of acoustics waves, where the spectrum and directivity depends on the scattering properties of the specific trailing-edge and airfoil geometry as well as on the turbulence spectra in the boundary layer.

From the above outline the underlying physics involved in this type of noise generation becomes apparent. At least two factors have a major influence on the intensity and directivity of the noise of which one is of fluid dynamic nature, the other one of aero-acoustic nature:

1. Fluid mechanical properties of the boundary layer and incident turbulence

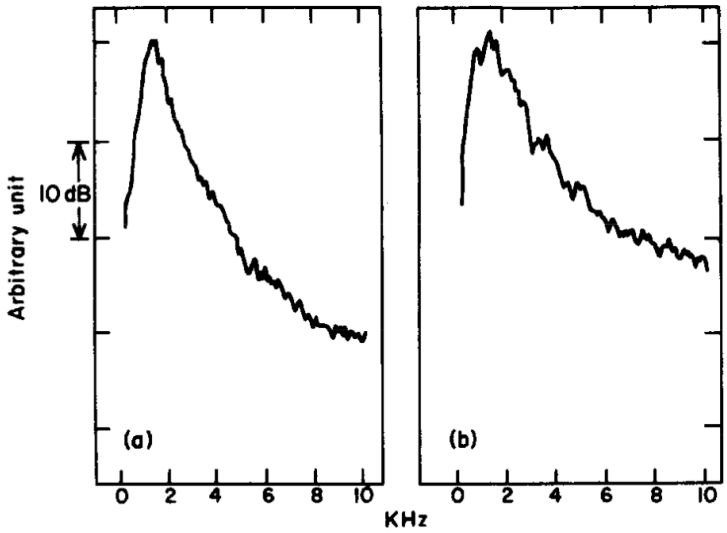

Figure 2.3: Comparison of the surface pressure spectrum (a) and the far-field acoustic spectrum (b) [Yu and Tam (1977)]

2. Aero-acoustic scattering properties of trailing-edge and airfoil geometry

It can be deduced that for the case of the straight trailing-edge a relation between the surface pressure spectrum and the far-field acoustic spectrum must exist, which is sometimes reflected in the shape of the spectra. Figure 2.3 depicts the results of a comparison of both spectra which can be found in Yu and Tam (1977). Howe (1998) derives expression 2.1, relating the far-field spectrum to the pressure spectrum under the assumption of a flat plate of finite span with non-compact chord. Here, M is the Mach number, L the length wetted by the flow along the span, l_3 the spanwise correlation length, θ and ψ define the position of the observer, and Φ_{BL} the surface pressure spectrum.

$$\Phi\left(\mathbf{x},\omega\right) \approx \frac{ML\sin^2\theta\sin\psi l_3}{2\pi^2|\mathbf{x}|^2}\Phi_{BL}\left(\omega\right) \tag{2.1}$$

Powell (1959) was first with his investigation which resulted in a proposed scaling of the noise intensity with $U^{4.6}$, where U is the freestream flow velocity, while the power spectral density should reduce with the inverse of the frequency in the limit of high frequencies. The $U^{4.6}$ dependence is in contrast to the findings in a number of publications, for instance Ffowcs Williams and Hall (1970), which predict a dependence on U^5 instead.

Howe (1978) includes additional effects such as the flight Mach number and finds it to be in agreement with the results obtained by other researchers before. According to this analysis the edge noise scales with the parameters given in equation 2.2, where L is the wetted span, l_3 is the turbulence correlation length scale in the direction of the edge, U_c the characteristic eddy convection velocity, M_0 the flight Mach number and M_{v_1} the component of the boundary

layer Mach number perpendicular to the edge.

$$\langle p^2 \rangle \sim L l_3 U_c^5 \left(1 - M_0 - M_{v_1}\right) \tag{2.2}$$

The well-known Kutta condition applying at the trailing-edge of an airfoil or flat plate prevents singularities to occur at this point in the flow field by the action of viscous forces. It has been shown by Ffowcs Williams and Hall (1970) that in the presence of the Kutta condition the noise intensity of TBL-TE noise is substantially modified compared to the high Reynolds number limit for which the authors found the mentioned U^5 dependence. However, the viscous effects acting to reduce the the intensity of TBL-TE noise in turn trigger the other noise generation mechanism, i. e. unsteady vortex shedding or BTE noise and it is suggested that vortex shedding reduces the noise intensity of TBL-TE noise by effectively increasing the length of the plate, i. e. decreasing the gradient of the normal velocity component at the trailing-edge. In a summation of these effects, it is concluded in Howe (1978) that the noise intensity maintains the scaling with U^5 when the Kutta condition applies.

2.1.2 Blunt trailing-edge noise

Noise generation at the blunt trailing-edge is a process which can be understood rather intuitively because of its discrete nature. As a result of the shear layers originating at blunt parts of the trailing-edge vortices of discrete time and length scales develop in a often periodic fashion. These larger vortices are superimposed on the turbulence convecting inside the boundary layer and can have a considerable influence on the wall pressure field and the scattering process at the trailing-edge.

The most important length scale is the bluntness, for instance the thickness of the trailing-edge t, which determines the typical size of the vortex structures shed from the edge. Together with a characteristic velocity scale, for example the convection velocity of the boundary layer U_c, it determines the frequency of the tonal noise ω, first investigated by Strouhal (1878), through the relation in equation 2.3 (see figure 2.4).

$$\frac{\omega t}{U_c} \approx 1 \tag{2.3}$$

An important question to ask is under what conditions BTE noise is important compared to TBL-TE noise. This ratio is governed by another non-dimensional quantity termed bluntness parameter $\frac{t}{\delta^\star}$ where $\delta^\star$ is the boundary layer displacement thickness. A trailing-edge is considered to be sharp if the bluntness parameter $\frac{t}{\delta^\star} < 0.3$. The noise production due to the BTE mechanism is then negligible according to Blake (1986).

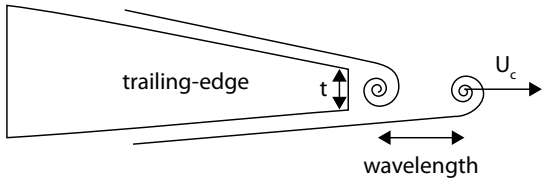

Figure 2.4: Parameters for vortex shedding from the blunt trailing-edge

2.2 Trailing-edge modifications for noise reduction

In order to reduce the noise generation at the trailing-edge it is necessary to deal with the two fundamental mechanisms described in section 2.1 and to modify the conditions such that their effect is reduced as much as possible.

In the case of BTE noise one solution seems to be obvious: Reducing the bluntness of the trailing-edge to a small percentage of the boundary layer thickness greatly reduces the possibility of large, coherent vortices being shed from the edge and therefore reduces the part of noise generated due to vortex shedding. Therefore, an efficient means of reducing BTE noise is to avoid blunt trailing-edges in the design of airfoil configurations or rotor blades. In cases where this is impossible, the relative contributions of BTE noise and TBL-TE noise have to be evaluated to estimate whether reduction of the overall noise intensity can be obtained by applying means to reduce TBL-TE noise only.

Several attempts have been undertaken in the past to reduce the broadband noise generated by the turbulent boundary layer passing over the trailing-edge. Early research has been performed on noise-abating porous edge extensions by Bohn (1976) and Fink (1980). Later, sawtooth serrations appeared as means to reduce the exhaust noise of a jet engine in Ver (1987) and research related to jets has continued since then.

After a theoretical treatment of sawtooth serrations or chevrons for a simplified model in Howe (1991a) and Howe (1991b) research has been directed towards this type of noise reduction device. Experimental and numerical studies on the topic have been performed by Dassen et al. (1996), in the framework of the STENO (Serrated Trailing-Edge NOise) project by Braun et al. (1997) and Braun et al. (1999), by Schröder et al. (2004), with focus on wind turbine applications of present interest by Oerlemans et al. (2008) and recently by Gruber et al. (2010) and Jones and Sandberg (2010). Since sawtooth serrations are subject to research in this study, more details are provided in section 2.4.

Another type of trailing-edge modifications, which has been investigated in the past, are termed brushes. Wind tunnel experiments have been conducted in the framework of the RAIN (Reduction of Airframe and Installation Noise) project and have been successfully applied by Mau and Dobrzynski (2003). Further research for this type of modification has been conducted by Herr and Dobrzynski (2005).

2.3 Howe's theory of trailing-edge serrations

Howe (1991a) introduced a theory to predict the effect of a generic serrated trailing-edge on noise production and applied it to the special case of sawtooth serrations in Howe (1991b). According to this theory significant reductions are possible when trailing-edge serrations are applied. This is attributed to a reduction in effective trailing-edge length which can contribute to the production of noise, although the physically wetted trailing-edge length increases. For an eddy with a characteristic wavenumber spectrum $\mathbf{k} = (k_1, 0, k_3)$ it is found that this eddy contributes significantly to noise production only if $\mathbf{k}$ is normal to the edge. The partial information on the wavenumber spectrum which is characteristic for a turbulent boundary layer, namely $\frac{k_3}{k_1} < 1$, indicates that the dominating part of the noise production occurs at the parts of trailing-edge which are inclined at angles at larger angles to the mean flow.

From these findings it becomes apparent that serrations of sawtooth profile with inclinations less than 45° of the trailing-edge with respect to the mean flow should be effective in reducing the noise. For serrations of wavelength λ and root-to-tip distance $H = 2h$ and given $\frac{\lambda}{h} < 4$, where the inclination of the trailing-edge with respect to the flow fulfils the criterion $\Phi < 45°$, Howe (1991b) gives the estimate for the noise reduction potential provided in equation 2.4.

$$\Delta SPL = 10 \cdot log_{10}\left(1 + \left(\frac{4h}{\lambda}\right)^2\right) dB \tag{2.4}$$

2.4 Experimental and numerical results for serrations

A large number of researchers have tackled experimentally and numerically the noise reduction potential of trailing-edge serrations and many have confirmed the principle statement of Howe's theory.

Dassen et al. (1996) showed the noise reduction potential for more realistic configurations by the application of serrated blade trailing-edges at Mach numbers of $M = 0.12,\ 0.18,\ 0.22$ and corresponding Reynolds numbers of $Re_c = 0.7 \cdot 10^6,\ 1.0 \cdot 10^6$ and $1.4 \cdot 10^6$. This study was conducted as part of a preliminary evaluation for the JOULE III project *Investigation of Serrated Trailing Edge Noise* (STENO) For this purpose, wind tunnel measurements on the self-noise for different airfoils (NACA 0012, 63018, 63618, 4418) and flat plates ($c = 250mm$ for all models) have been conducted with serrated trailing-edges of varying dimensions and at various angles with respect to the chord line. The serrations had a length of $50mm$ (equal to $0.2c$) and a tip spacing or wavelength of $\lambda = 5mm$ yielding a flow angle of approximately $\Phi = 3°$ in the standard configuration.

All serrated airfoils were found to yield an overall reduction of the emitted noise level in the range of $3dB$ to $8dB$ while the shape of the spectra, the dependency on the flow angle and on the angle of attack varied for different airfoil types. For the flat plate models higher reductions up to $10dB$ in the band from $1kHz$ to $6kHz$ were found while an angle of attack of 10°, a swept trailing-edge geometry and misalignment of the teeth with respect to the flow

direction by 10° only showed a minor detrimental effect below $2dB$. However, misalignment by 15° lead to an increase of the noise level.

As part of the STENO project Braun et al. (1997) and Braun et al. (1999) performed an optimization study on the serration design at the tip of wind turbine plates. A combination of numerical and experimental investigations yielded an optimum geometry where the serrations have a length of 20% of the chord aligned in chord-wise direction and a length-to-base ratio of 2. Following far-field microphone measurements showed a reduction of up to $3dB$ in the sound pressure level for frequencies below $2kHz$ for different angles of attack, but an increase in noise level for high frequencies contrary to theory. Since the low frequencies dominated the overall acoustic emission of the blade, the total sound pressure level was reduced for angles of attack ranging from 3° to 13° (about $2dB$), but increased for lower angles of attack.

The measured reductions were less than predicted by Howe's theory which was partially attributed to the fact that the serrations have been aligned with the suction side surface of the airfoil, assuming that boundary layer perturbations on this side dominate the overall noise production. Since it was discovered before that high frequency perturbations of the pressure side dominate the emitted noise level in this frequency domain, noise reduction can only be expected if the perturbation on the pressure side are also accounted for. Furthermore, it was believed that serrations do influence the fluid mechanics of the system like the boundary layer characteristics, which is in contrast to Howe's assumptions. For instance, increasing pressure differences between pressure and suction side at higher angles of attack might lead to a distortion of the streamlines with a detrimental effect to the noise reduction.

Herr and Dobrzynski (2005) presented an evaluation of the noise reduction potential for different design concepts of trailing-edges, namely brushes. Brush-type trailing-edges are similar to serrations as both of them resemble a porous design. In a way brushes can be considered as a limiting case of serrations for wavelengths tending to zero. The measurements were conducted in the open jet Aeroacoustic Wind Tunnel of the DLR in Braunschweig on flat plate models at Reynolds numbers of $Re_c = 2.1 \cdot 10^6$ up to $7.9 \cdot 10^6$ ($c = 0.8m$,$1.2m$,$1.6m$ and $2.0m$, $U_{\text{inf}} = 40m/s$,$50m/s$, and $60m/s$) and 0° angle of attack. Brush-type devices appeared to be highly effective in reducing both, BTE narrowband and TBL-TE broadband noise. They showed a broadband noise reduction of $2dB$ - $10dB$ from $1kHz$ to $16kHz$ in $SPL_{1/3}$. The noise reduction potential was found to be limited to a range of Strouhal numbers $0.02 \leq St \leq 0.2$ while for higher Strouhal numbers $St > 0.2$ an increase in broadband noise was observed.

Oerlemans et al. (2008) experimentally compared the noise reduction potential of trailing-edge serrations on the blade of a wind turbine to shape optimized airfoils. Acoustic field measurements were conducted on a wind turbine of $94m$ diameter. It was shown that both configurations bear noise reduction potential at low frequencies, which was more significant for the serrations. The measured noise reduction with respect to the reference blade were on the order of $3dB$ in the sound pressure level.

Recent effort has been made by Gruber et al. (2010) comparing measured trailing-edge self-noise reduction of a NACA 651210 airfoil with sawtooth trailing-edge (flat plate attachments) to theoretical predictions based on Howe's theory. The study demonstrated reductions of up

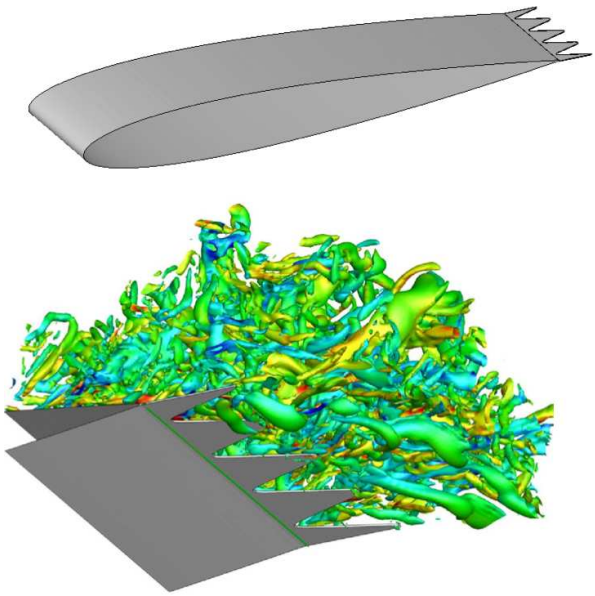

Figure 2.5: Geometry and visualization of vortices between serrations (Q-criterion) [Jones and Sandberg (2010)]

to $5dB$ over a wide frequency range which is below the expectations derived from theory. It is suggested that vorticity generated along the wetted edges of the trailing-edge poses an additional noise source, therefore reducing the noise reduction potential of the serrations. In particular, it is observed that noise levels increase for frequencies above a critical frequency dependent on $f_0\delta/U_c \approx 1$.

A numerical attempt to study the influence of serrations (flat plate extensions aligned with the chord line of length $0.06c$ and $0.12c$, see figure 2.5) on the noise production has been recently presented by Jones and Sandberg (2010). A NACA 0012 profile was subject to their investigation at $Re = 5 \cdot 10^4$, $M = 0.4$ and angle of attack of $5°$. The solution of a two-dimensional Direct Numerical Simulation (DNS) of the entire flow domain including the airfoil after a certain number of time-steps was used as initial data for a three-dimensional DNS in a restricted computational domain near the trailing-edge. No significant differences between the turbulent boundary layers for the straight and serrated models were reported upstream of the trailing-edge leading to the conclusion that any change in the noise level must be caused by either a modification of the scattering process or by a change in the hydrodynamic behaviour directly at the trailing-edge. Compared to the straight trailing-edge an increased number of horseshoe-type vortices was observed in the spaces between the serrations and additionally the maximum spanwise extent of large coherent structures seems to be limited to the distance between two adjacent tips.

Chapter 3

Organisation of the turbulent boundary layer

In this chapter, a short review on the characteristics of the turbulent boundary layer and its organisation is presented. Section 3.1 starts with the explanation of inner and outer scaling and the division of the boundary layer into different regions according to the velocity gradient in wall-normal direction. In section 3.2 the properties of the coherent structures reported in literature are presented. According to a particular school of thought in fluid dynamics (Adrian (2007)), these coherent structures have an important impact on the events in the boundary layer by giving some order to its seemingly random nature. Section 3.3 points out the relation between the various structures and motions. Since some coherent structures are related to the concept of a vortex, vortex identification criteria are needed to examine experimental and numerical data. A selection of the available criteria is provided in section 3.4.

3.1 Boundary layer scaling and division

In boundary layer studies it is a common practise to denote the coordinate tangential to the wall by x and the wall-normal coordinate by y. Depending on the use of left- or right-handed coordinates the orientation of the spanwise coordinate varies, but is commonly denote by z. In the inner region, close to the wall, variables related to the conditions at the wall determine the scaling of flow variables in similarity laws, namely the wall shear velocity u_τ, which can be expressed as ν/δ_ν. Here, δ_ν is the so-called viscous wall unit and ν the kinematic viscosity. Variables in inner scaling are often called "plus"-units for reasons of notation and are defined in equation 3.1. For certain canonical flows the viscous wall unit can be derived analytically, but if experimental data is available its value is obtained by fitting procedure.

$$\begin{aligned} y^+ &= \frac{y u_\tau}{\nu} = \frac{y}{\delta_\nu} \\ u^+ &= \frac{u}{u_\tau} \end{aligned} \tag{3.1}$$

Table 3.1: Division of the boundary layer [Pope (2009)]

Inner layer	$\frac{y}{\delta} < 0.1$	Scaling with u_τ and y^+
Viscous sublayer	$y^+ < 5$	Reynolds stress negligible compared to viscous stress
Buffer layer	$5 < y^+ < 30$	Overlap between viscous sublayer and log-law region
Viscous wall region	$y^+ < 50$	Viscous contribution to shear stress important
Outer layer	$y^+ > 50$	Direct effects of viscosity negligible
Overlap region	$y^+ > 50, \frac{y}{\delta} < 0.1$	Overlap between wall and outer region
Log-law region	$y^+ > 30, \frac{y}{\delta} < 0.3$	Log-law region

In the so-called outer scaling, velocity and wall-normal coordinate are normalised with the velocity outside the boundary layer u/U_δ and the boundary layer thickness y/δ.

Different regions in the boundary layer can be distinguished. The extension of each region within the boundary layer has relatively universal limits in terms of non-dimensional coordinates in wall-normal direction. Pope (2009) gives the division shown in table 3.1. For any particular case more appropriate extensions can be found by comparing measured velocity profiles to the theoretical scaling laws in the individual regions.

In order to fit an experimentally obtained velocity profile in the outer region, Cole's law of the wake in equation 3.2 is used as given in White (2006) which accounts for the presence of a pressure gradient at the trailing-edge of the airfoil. The logarithmic law constitutes the first and second term of the equation while the third term is a correction for factors such as the presence of a pressure gradient.

$$\begin{aligned} u^+ &\approx \frac{1}{\kappa}\ln y^+ + B + \frac{2\Pi}{\kappa} f\left(\frac{y}{\delta}\right) \\ f(\eta) &\approx \sin^2\frac{\pi}{2}\eta \approx 3\eta^2 - 2\eta^3 \end{aligned} \tag{3.2}$$

In the above equation, von Karman's parameter $\kappa \approx 0.41$ and the constant $B \approx 5.0$ are fairly universal for all turbulent boundary layer profiles. The additional parameter Π is termed Clauser's equilibrium parameter for which the relation $\delta^\star/\delta \approx (1+\Pi)/\kappa\lambda$ holds, with $\lambda = (2/C_f)^{\frac{1}{2}}$, obtained by integrating equation 3.2 across the boundary layer. This latter relation can be used together the evaluation of equation 3.2 at the edge of the boundary layer to relate the friction coefficient C_f to Π and the Reynold's number based on the boundary layer thickness, defined as $Re_\delta = U_e\delta/\nu$. This relation is shown in equation 3.3 and can be used together with the previously mentioned relations to determine Clauser's equilibrium parameter Φ and λ simultaneously.

$$\frac{U_e}{u_\tau} = \lambda = \left(\frac{2}{C_f}\right)^{\frac{1}{2}} = \frac{1}{\kappa}\ln\frac{Re_\delta}{\lambda} + B + \frac{2\Pi}{\kappa} \tag{3.3}$$

3.2 Coherent structures and motions in boundary layers

Several authors have compiled reviews on the type and characteristics of coherent structures and motions observed in boundary layers, both in experiment and in simulation (Robinson (1991), Adrian (2007)). In general, the first problem encountered is adapting a firm definition resembling the nature of coherent structures or events. Pope (2009) adapts the following, very general definition:

> [A coherent structure is a] region of space and time within which the flow field has a characteristic coherent pattern.

Another definition of a similarly general nature stems from Robinson (1991):

> [A coherent motion is a] three-dimensional region of the flow over which at least one fundamental flow variable (velocity component, density, temperature, etc.) exhibits significant correlation with itself or with another variable over a range of space and/or time that is significantly larger than the smallest local scales of the flow.

This definition implies that we are looking for patterns in space and time which can be of, for instance, periodic nature or show reoccurring features. Furthermore, it answers the question why coherent structures are of interest and focus of many experimental and numerical investigations: Given any form of these structures can be observed in the flow of a particular situation, then these structures, due to their coherence in space or time, can have an important impact on the macroscopic behaviour of the fluid.

In literature many coherent structures satisfying the above definition have been identified, named and characterized. Table 3.2 gives a short overview based on several review articles on the topic, for instance Robinson (1991), Pope (2009) and Adrian (2007).

Relatively early the so-called low-speed streak has been identified. A region of relatively low-speed fluid whose streamwise extension exceeds the spanwise coherence by far. Its streamwise dimensions and dependence on parameters such as adverse pressure gradient and Reynolds number remain to date unclear, but the spanwise spacing is often reported to be relatively constant $100 \pm 20\delta_\nu$, for instance by Smith and Metzler (1983), while the width certainly depends on the chosen threshold level of velocity and distance from the wall. For this reason the spacing rather than the ambiguous width is used to characterize the spanwise correlation of low-speed streaks. Smith and Metzler (1983) found the above mentioned spacing for $y^+ \leq 30$, using hydrogen-bubble wire visualisation as shown in figure 3.1, to have the tendency to increase with the distance from the wall. From their perspective, a clear definition of the low-speed streaks beyond $y^+ \approx 30$ was not possible. Streamwise extensions in channel flow have been reported to be $2000 - 3000\delta_\nu$, exceeding the spanwise extension by an order of magnitude.

Table 3.2: Characterisation of coherent structures in boundary layers

Name	Description
Low speed streaks	Coherent region with velocity lower than mean wall region, $\lambda_1 \approx 4\delta$, $\lambda_3^+ \approx 100$
Ejections	lifting motion in buffer and logarithmic region dominant in $y^+ > 12$
Sweeps	inrushes of high-speed fluid, motion towards wall dominant in $y^+ < 12$
Vortical structures	hairpin or horseshoe shaped, often asymmetric canes inclination 45°, package growth angle $10° - 30°$ individual growth angle 1°
Shear-layer backs	separating inrushing and out-rushing fluid
Large-scale motions	bulges, packages of hairpins scales of $2 - 3\delta$

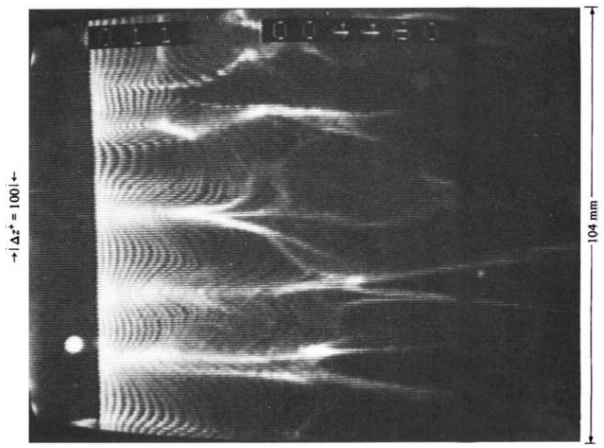

Figure 3.1: Low-speed streak patterns with spanwise hydrogen-bubble wire visualisation $y^+ = 5$, $Re_\theta = 740$, $f = 60Hz$ [Smith and Metzler (1983)]

Close to the wall low-speed streaks are believed to originate in the viscous sublayer as a consequence of instabilities and resulting streamwise vortices, which suggests a connections to other coherent structures as will be explained in section 3.3. It is believed that these coherent streamwise vortices lift low-speed fluid from the region extremely close to the wall, generating long streaks within the wall region. The origin of these streamwise vortices is not ultimately determined yet and discussion continues on whether they are related to another kind of coherent structure frequently discussed in literature - hairpin vortices. Further away from the wall, above the buffer layer, packets of hairpins can induce the generation of new low-speed streaks.

Hairpin vortices owe their name to the shape which becomes apparent under suitable visualisation methods. Smoke visualisation used in early research could not reveal the dynamics and importance of hairpins through the boundary layer, but visualisation on top of bulges in the outer region of the boundary layer was possible as shown in figure 3.2(a). Hairpins can

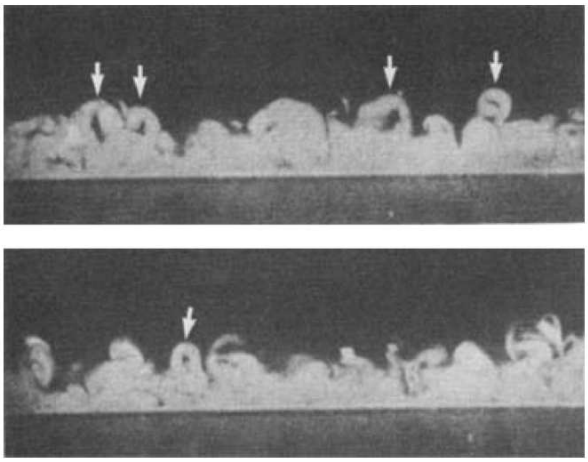

(a) Smoke visualisation of hairpin vortices in the outer region, Head and Bandyopadhyay (1981)

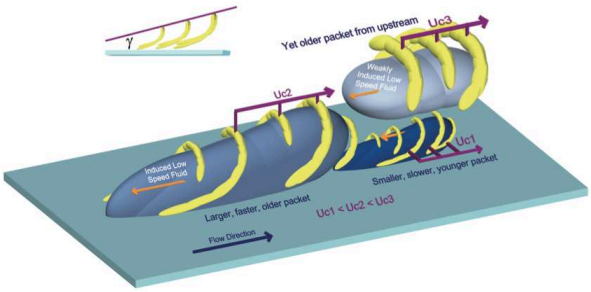

(b) Hairpin packets on low-speed streaks, Adrian et al. (2000)

Figure 3.2: Hairpin vortices as coherent structures in the turbulent boundary layer

be thought of as vorticity tubes with that particular shape convecting through the boundary layer, while being deformed by the shearing mean velocity profile. Some examples of hairpin vortices with the canonical, almost perfectly symmetric shape are depicted in figure 3.2(b) on the backs of low-speed streaks, where they are observed to occur in most cases. The arch-like piece of the hairpin is also termed head while the streamwise extensions of the vortex are called legs and the connection between these parts is termed neck. Adrian (2007) claims that perfectly symmetric structures are an exception in real boundary layers and that asymmetric structures with legs of different lengths, called canes, are most probable in nature.

The relative positioning of hairpin vortices and low-speed streaks as shown in the figure is no coincidence but due to the fact that hairpin vortices induce low-speed streaks and vice versa as will be explained in section 3.3. Knowing the typical spanwise spacing of low-speed streaks, it is therefore not surprising that the width of fully developed hairpin vortices is on

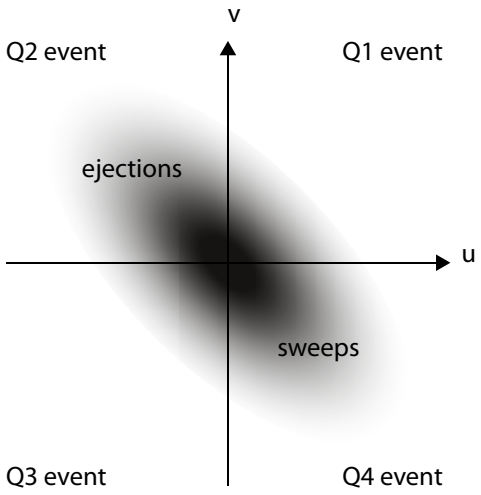

Figure 3.3: $u'v'$ quadrant splitting

the same order, namely $100 - 150\delta_\nu$. Another marking characteristic of hairpin structures is the relatively constant inclination of about 45° with respect to the wall. More disputed is the rate of growth that a hairpin experiences during its life-time. Elsinga (2008) reports a physical growth rate of about 1° in a boundary layer flow. For multiple hairpins in a so-called hairpin packet Adrian and Liu (2002) reported angles of $10° - 12°$ for channel flow in wall-normal direction connecting the heads and in spanwise direction between the legs while Smith et al. (1984) claimed $15° - 30°$.

Ejections and sweeps can be represented by the $u'v'$ quadrant splitting shown in figure 3.3 which points out the conceptional relation to dominant Reynolds stresses. An event in the second quadrant, i. e. negative u' and v' over a coherent region in space and time, is called ejection due to its typically rapid upward motion, while sweeps are connected to inward rushes of high-speed fluid. Together, they account for 25% of the dominant turbulent shear stress $-\overline{u'v'}$ while occupying less than 5% of the area in the streamwise-wall-normal plane. While ejections are dominant in parts of the buffer, logarithmic and outer region $y^+ > 12$, sweeps occur preferably for $y^+ < 12$. The origin of ejections is related to the hairpin vortices described above generating an upward movement of the flow behind them due to their inclination which for strong aligned vortices can have amplifying, strong effects which in that case are also termed rushes. Due to the principle of mass continuity sweeps are necessary to transport fluid from the outer parts of the boundary closer to the wall.

At the backs of hairpins the rising, out-rushing fluid might encounter inrushing fluid from regions remote from the wall. Where these oppositely directed fluid motions encounter a so-called shear-layer back is created which is often inclined with respect to the wall, rising in downstream direction.

In relatively recent works, attention has turned towards large scale motions (LSM) or even very large scale motions (VLSM) which are a macroscopic feature of the boundary layer and responsible for some of its properties. So-called bulges, packages of large hairpins, can have scales of $2 - 3\delta$ and are relatively simple to visualize by various methods. For instance, in

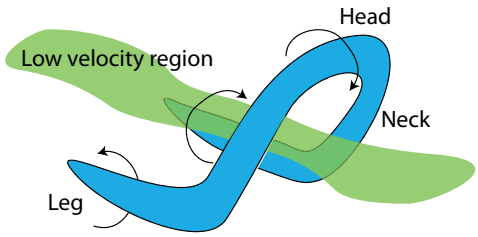

Figure 3.4: Hairpin eddy attached to the wall

smoke visualisations deep valleys of irrotational fluid and, conversely, hills can be be identified as shown in figure 3.2(a).

3.3 Relation between low-speed streaks, ejections, sweeps and hairpins

As mentioned in the previous section, some of the coherent structures and motions in the boundary layer can be related to each other. Figure 3.4 shows the typical arrangement of low-speed streak and hairpin. Consider a quiescent fluid and superimpose a single annular vortex tube. As a result a velocity in the center of the ring-shaped vortex would be induced. Similarly, a hairpin vortex of proper orientation can induce a region of relative low-speed fluid with respect to the mean velocity profile of the boundary layer.

This process might also happen in reversed order. An existing low-speed region creates shear layers which might ultimately lead to the formation of a hairpin vortex. This cycle has been termed auto-generation by Adrian (2007): If a low-speed streak or hairpin exists, there is a possibility for new hairpins to be created which are most likely aligned in streamwise direction. Through this process a series of hairpins can be created on a single low-speed streak which is then called hairpin packet. From the point of view of coherent structures this is an amplification since coherence through periodicity in space is augmented.

The legs of such hairpins, if assumed to be located alongside low-speed streaks, tend to lift the fluid in between upwards while the hoop can cause rapid ejections of fluid as depicted in figure 3.4. These legs might also be responsible for the initiation of the reproduction process in the form of streamwise vortices very close to the wall. Once a streamwise vortex near the wall exists it has the potential to lift fluid with a very low velocity from the vicinity of the wall to regions of higher velocity, therefore creating low-speed streaks. In order to satisfy conservation of mass an inrush of fluid is necessary for balancing, which in turn creates shear-layers as described in the previous section.

3.4 Vortex identification criteria

An important type of coherent structure in turbulent boundary layers is the hairpin vortex due to its relation with other coherent structures such as low-speed streaks and ejections. It is therefore desirable to have criteria at hand which facilitate the identification of these hairpin vortices. Some criteria have been based on the Galilean-invariants of the velocity gradient tensor $\bigtriangledown u$, a review of which can be found in Jeong and Hussain (1995).

A first method derives from the eigenvalues σ of the velocity gradient tensor which can be written in the form shown in equation 3.4 where $P = u_{ii}$ ($= 0$ for incompressible flow), $Q = \frac{1}{2}(u_{ii} - u_{ij}u_{ji})$ and $R = |\bigtriangledown u|$ are the invariants of the velocity gradient tensor mentioned above.

$$\sigma^3 - P\sigma^2 + Q\sigma - R = 0 \tag{3.4}$$

According to Chong et al. (1990) a vortex core is characterized by complex eigenvalues which occur when the determinant Δ is positive, leading to the criterion in equation 3.5.

$$\Delta = \left(\frac{1}{3}Q\right)^3 + \left(\frac{1}{2}R\right)^2 > 0 \tag{3.5}$$

A second method was proposed by Hunt et al. (1988) which makes use of only the second invariant Q, therefore also termed Q-criterion, but in its original formulation bears the additional condition that the pressure should attain a minimum in a vortex core. In velocity field measurement techniques such as particle image velocimetry the pressure field is not available and thus only the part of the definition based on the invariant is taken into account. Q itself represents a measure for the importance of the vorticity magnitude opposed to the shear strain rate in a given point as the decomposition in equation 3.6 shows, where $S = \frac{1}{2}(u_{ij} + u_{ji})$ and $\Omega = \frac{1}{2}(u_{ij} - u_{ji})$ are the symmetric and anti-symmetric components of the velocity gradient tensor $\bigtriangledown u$, respectively, and $\| \cdot \| = tr(\cdot\cdot^T)^{\frac{1}{2}}$. Therefore S contains the shear and dilatation components while Ω represents the rotational components.

$$Q = \frac{1}{2}(u_{ii} - u_{ij}u_{ji}) = \frac{1}{2}\left(\|\Omega\|^2 - \|S\|^2\right) \tag{3.6}$$

Chapter 4

Experimental techniques

In the course of this study, a variety of experiments are conducted to assess the acoustic properties of various serration designs and the related flow structure. While microphone measurements are used to determine the noise spectra in the far-field, particle image velocimetry (PIV) measurements are designed to measure the velocity field and derive appropriate quantities to visualize turbulence in the form of coherent structures. A third technique, also employing microphones as measurement devices, seeks to determine the pressure fluctuations on the surface of the airfoil models.

This chapter gives a short introduction to the various measurement techniques mentioned above, while chapter 5 continues with the set-up of the experiments and configuration of facilities and models in particular. In section 4.1 the principle of microphone measurements and adequate data reduction procedures are described. Section 4.2 continues with the principle of the PIV technique for velocity field measurements and closes with an explanation of the particularities regarding stereoscopic PIV and tomographic PIV, which measure three velocity components in a plane or volume, respectively.

4.1 Microphone measurements

Microphones have nowadays adapted a substantial role in our daily lives and can be found in different kinds of electrical devices from mobile phones to notebooks. Various types of microphones subdivided according to their working principle, or type of transducer, and directivity. The most important types of microphones are of condenser type (also called capacitor or electrostatic microphones) and electret condenser microphones. A comprehensive treatment of different types of microphones, their working principles and measurement techniques can be found in Lerch et al. (2009). A schematic of a typical condenser microphone is shown in figure 4.1.

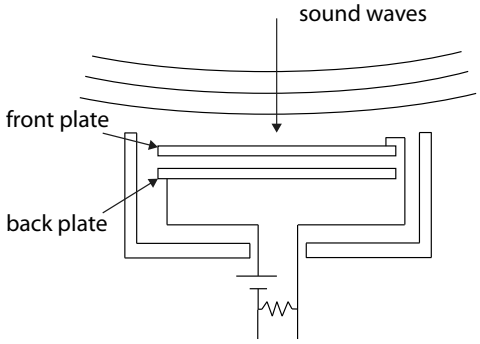

Figure 4.1: Schematic of typical condenser microphone

The working principle of a condenser microphone is relatively simple: A diaphragm serves as one plate of a capacitor and can be excited to vibrate, following pressure disturbances on one side of the diaphragm. Often, a microphone is designed in such a way that the opposite side of the diaphragm also reacts to pressure disturbances with a delay while being insensitive to fast vibrations. Hence, the pressure difference between opposite sides of the diaphragm p', often equivalent to the fluctuating part of the static pressure, is measured rather than the static pressure itself. When the diaphragm starts to vibrate, therefore inducing a change in the distance d between the condenser plates, the capacity changes continuously with these vibrations since $C = \frac{\epsilon A}{d}$ with ϵ being the dielectric constant specific to the substance between the plates and A the area of the capacitor plates.

Assuming that the charge of the condenser stays approximately constant at all times since the mechanical vibrations induced by sound pressure waves usually have high frequencies between $20Hz$ and $20kHz$, the voltage V over the condenser is prescribed by the capacity law, proportional to the distance between the plates as shown in equation 4.1.

$$V = \frac{Q}{C} = \frac{Q}{\epsilon A} d \tag{4.1}$$

The voltage variations can be measured and due to the linear relationship between voltage and pressure the measurements can be converted to units of pressure after calibration. Calibration is performed using a defined sound source emitting pressure waves of a specified amplitude and frequency. Electret microphones use a polarized ferroelectric material such that no externally applied voltage to charge the capacitor is required.

4.1.1 Far-field microphone measurements

Acoustic measurements are frequently conducted such that the microphones are positioned in the far-field, since the results usually relate to everyday applications, for instance an aircraft during take-off or landing. The far-field is a term for the region sufficiently remote from the source region, where the sound is generated and where interference effects are present. If $\frac{\lambda_a}{2\pi r} << 1$, where λ_a is the acoustic wavelength and r the distance between the source and observer, the observer is said to be located in the far-field, where pressure and velocity

fluctuations are in phase. On the other hand, for $\frac{\lambda_a}{2\pi r} >> 1$ the observer is said to be in the near-field. Due to the factor 2π the far-field condition is in practice usually fulfilled for middle and high-frequency sounds as stated in Roger (2009) (example: For $f = 1kHz$ at $r = 1m$, $\frac{\lambda_a}{2\pi r} = 0.05 << 1$). In the acoustic far-field the phases of velocity and pressure perturbations are assumed to coincide. In the geometrical far-field additionally the assumption of plane waves holds.

Furthermore, the size of the microphone itself should be sufficiently smaller compared the wavelength of the sound waves which are subject to the measurements since otherwise the presence of the microphone has an effect on propagation of the sound waves. If for instance $d = 0.01m$ is the diameter of the microphone directed towards the sound source the condition can be formulated as $f << \frac{a}{d} = 34kHz$, where a is the speed of sound, which is usually fulfilled for frequencies of interest and common types of microphones.

4.1.2 Surface microphone measurements

For the measurement of pressure fluctuations on the surface, there are in general two options of devices to choose from: As a first option one might consider the use of pressure transducers, which measure the difference in pressure with respect to an arbitrary reference pressure but are expensive compared to microphones for a particular sensitivity. Microphones, on the other hand, measure pressure fluctuations also with respect to a reference pressure which however is commonly the time-average of the local static pressure due to the working principle using a membrane and small ventilation holes.

The working principles of surface mounted microphones is identical to the principles discussed above for microphones in general. However, in addition these microphones have to be very small in order to fit in the space between the surfaces of a wing profile close to the trailing edge such that the boundary layers on both sides of the profile are disturbed as little as possible. The orifice of the cavity has to be small to avoid excessive averaging due to the relatively small wavelengths present in the wall-pressure spectrum.

4.1.3 Data reduction procedures

Data obtained by measurements of a single microphone can be reduced in different ways yielding information about the frequency content and intensity of the signal. The result of this kind of reduction procedures is called the power spectral density (PSD) of the signal. Discrete methods to obtain the spectrum are based on the Fast Fourier Transform (FFT), a discrete version of the Fourier transform in continuous space. Before applying any of the reduction procedures for microphone measurements, the time mean value of the pressure signal is subtracted removing the constant component of the signal, but generally this component is close to zero.

An example for such a method to estimate the spectrum is Welch's algorithm, where the

input signal vector is divided into a number of overlapping segments. A windowing function can be applied to each of these segments in order to avoid the effects of windowing for short time series. Consequently the periodograms are computed for each segment independently by means of the FFT and finally averaged to yield an estimation for the PSD Φ of the signal. In the case of noise measurements, the amplitude of the signal for different frequency components can differ by orders of magnitude which makes it often necessary to display the data on a logarithmic scale with respect to a reference level resulting in the unit decibel (dB) as shown in equation 4.2. The reference level for noise measurements is often defined as $p_0 = 2 \cdot 10^{-5} Pa$, which is the definition of the audibility limit of human hearing.

$$\Phi_{dB/Hz} = 10 \log_{10} \frac{\Phi_{Pa^2/Hz}}{p_0^2} \tag{4.2}$$

Alternatively, one might be interested in the power contained in certain frequency bands. For this purpose the 1/3-octave spectrum is often used which integrates the PSD over frequency bands defined by $\frac{f_{n+1}}{f_n} = 2^k$ with $k = \frac{1}{3}$, where f_n is the lower limit and f_{n+1} is the upper limit, and associates the resulting value with the frequency $f_{n+1/2} = 2^{k/2} f_n = 2^{-k/2} f_{n+1}$. In this way it is possible to discriminate bands of low, middle and high frequency noise in the evaluation.

Another quantity of interest is the sound pressure level (SPL) indicating the overall noise level. It is usually expressed in decibels and can be obtained by integrating the PSD over the entire frequency range or, alternatively, by computing the root-mean-square (RMS) of the mean subtracted time signal $p\,(t)$ as given in equation 4.3. Ideally, both approaches should yield the same value which, however, is not the case in practise since the computed spectrum is not exact.

$$SPL = 20 \log_{10} \frac{p_{rms}\,(t)}{p_0} \tag{4.3}$$

Besides the spectral and noise level properties mentioned above, which can be computed for each individual microphone, it can be useful to compute the cross-correlation and the correlation coefficient between the signals of two microphones located at different points in space. This type of cross-correlation is also termed 2-point-time-correlation and defined in equation 4.4 where $x(t)$ and $y(t)$ are the mean subtracted time signals recorded by different microphones and T is for instance the measurement time.

$$R_{xy}(\tau) = \lim_{T \to \infty} \frac{1}{T} \int_0^T x(t) y(t+\tau) dt \tag{4.4}$$

The cross-correlation of a signal with itself, for instance the data of a single microphone, is called the auto-correlation given in equation 4.5.

$$R_{xx}(\tau) = \lim_{T \to \infty} \frac{1}{T} \int_0^T x(t) x(t+\tau) dt \tag{4.5}$$

Normalising the cross-correlation of two signals with the roots of the auto-correlation with zero shift of both signals yields the correlation coefficient ρ_{xy} defined in equation 4.6, which

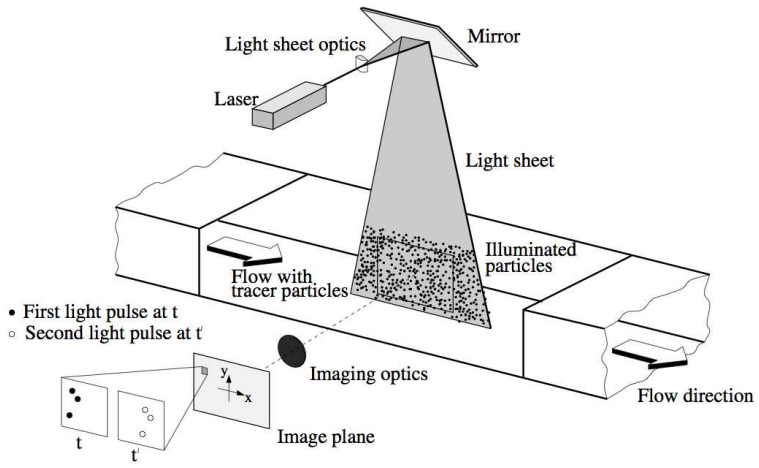

Figure 4.2: Schematic of typical arrangement for 2C-PIV [Raffel et al. (2006)]

is restricted to values $-1 \leq \rho_{xy} \leq 1$. A value of 1 indicates a perfect correlation of the two signals while a value of -1 indicates a perfect inverse correlation.

$$\rho_{xy}(\tau) = \frac{R_{xy}(\tau)}{\sqrt{R_{xx}R_{yy}}} \tag{4.6}$$

4.2 Particle image velocimetry

Particle image velocimetry (PIV) has experienced a rapid development during the past 20 years which was supported by the permanent increase in computing power, the development of more powerful and faster lasers and the introduction of high-speed sensors in cameras. It is a particle-based field measurement technique. An extensive treatment of PIV, its development during the past decades, the underlying physical principles, and its use in practise was published by Raffel et al. (2006) in collaboration with many internationally recognized experts in the field of PIV.

Figure 4.2 displays the typical set-up for a 2-Component PIV system which consists of several sub-systems, namely a seeding system (not depicted) which intersperses small particles called tracer particles into the flow, an illumination system consisting of a laser (short for Light Amplification by Stimulated Emission of Radiation) and light-sheet optics, and the digital imaging and recording system consisting of one or multiple cameras and imaging optics. The tracer particles are illuminated by laser pulses at least twice, with a short time separation in between and the camera records the light scattered by the particles in one or multiple images, also called frames. By comparison of an image pair the displacement of the particles within the short time interval between the laser pulses can be determined and from the known displacement and time separation the velocity of the fluid can consequently be derived under the assumption that the particle tracers follow the fluid motion sufficiently accurate. A formalisation of the post-processing technique to determine the particle displacement is the

based on cross-correlation.

Section 4.2.1 describes the seeding process, important considerations regarding the tracer particles and different particle generator systems currently used. Correctly adjusted, illumination, which is shed light on in section 4.2.2, is an important part of the PIV system, since the power limitations of the laser system especially in high-speed applications, reflections on model surfaces or unbalanced light distribution can have a detrimental effect on the quality of the results. Section 4.2.3 describes the equipment needed for imaging and image recording while section 4.2.4 gives insight on cross-correlation and data reduction procedures commonly employed. Finally, section 4.2.5 and 4.2.6 give an indication of the peculiarities encountered for advanced PIV techniques stereoscopic PIV (Stereo-PIV) and tomographic PIV (Tomo-PIV) repectively, which in general yield more information by the use of multiple cameras than the two velocity components.

4.2.1 Seeding

For the seeding of the flow a number of choices have to be made regarding the particle substance and size, the method of adding and mixing the particles with the fluid and the desired density of the particle seeding, usually expressed in units of *particles per pixel* (*ppp*). For the selection of the particle type and size it is important to have an estimation on the ability of the particles to follow the fluid accurately and on their light scattering behaviour.

For low speed motions the Stoke drag dominates the motion of the particles with respect to the fluid by inducing a velocity lag which is related to the difference in density between the fluid and the particles, the acceleration experienced by the fluid, its viscosity, and the typical diameter of the particles as shown in equation 4.7 where d_p is the particle diameter, ρ_p density of the particles, ρ the density of the fluid, μ the dynamic viscosity and $\mathbf{a}$ the local acceleration of a fluid parcel.

$$U_s = U_p - U = d_p^2 \frac{\rho_p - \rho}{18\mu}\mathbf{a} \tag{4.7}$$

The quantity $\tau_s = d_p^2 \frac{\rho_p}{18\mu}$ is called the relaxation time and the related Stokes number $St = \frac{\tau_s}{T}$, where T is a typical time-scale of the fluid motion, is a good indication for the ability of the tracers to follow the fluid given that $St << 1$. As a practical limit $St < 0.1$ is used. In the case of a turbulent boundary layer the flow time-scale is given by $T \approx \delta/U$, δ being the boundary layer thickness and U the freestream velocity.

Light scattering depends on various factors, such as the ratio of the refractive index of the particles to that of the surrounding medium and the particle size, shape and orientation. Usually, there is little control over the latter two properties, but the average size depends on the type of tracer. The average intensity approximately increases with the square of the particle diameter but also the relative angle between the illuminating light beam and the camera axis has an important influence. Mie's scattering theory can be applied for particles whose diameter d_p is greater than the wavelength of the incident light λ. As pointed out in Raffel et al. (2006), this analysis shows that intensity can be gained by placing cameras in

the so-called for- or backward scattering positions opposed to the side scattering positions, where the scattered light intensity reaches a minimum.

From the above considerations, it becomes clear that a trade-off is involved regarding the size of the tracer, namely between its abilities to follow the flow accurately and to scatter sufficient light. Tracer materials commonly employed in PIV experiments include smoke particles, oil or glass micro-spheres amongst others.

The seeding process itself is dependent on the chosen material and can be accomplished using condensation generators, smoke generators or atomizers. As stated in Raffel et al. (2006), neglecting particle in- and out-of-plane displacement it was found for double exposure PIV images that the particle image pair density should exceed 8 particles per interrogation spot in order to yield a valid detection probability of at least 95%. The particle density can only be increased as long as typical particle patterns are still recognizable in a way that the particles do no blend to a uniform fog, which would make correlation impossible. Increasing the number of particles per interrogation spot beyond this limit results in lower signal-to-noise ratios.

4.2.2 Illumination

As a light source a variety of monochromatic lasers are used which differ in the laser material, geometrical dimensions, power consumption and the resulting pulse energy, pulse repetition rate and wavelength of the emitted light. Some lasers can be used in continuous wave mode (CW) while others emit light only in the form of short pulses with a duration from a few nanoseconds up to a hundred microseconds. Also the quality of the laser beam intensity profile can vary significantly from the desired top-hat shape from one laser type to the other.

In figure 4.2 it can be seen that the light beam emitted by the laser has to be formed into a shape suitable for illuminating the field of view, typically a thin sheet, expanding or with constant width. The thickness $t$of the sheet is typically adjusted such that $t/FOV \approx 2\%$, where FOV is the field of view, such that the measurement plane approximates a plane in the flow domain. A system of lenses and mirrors is used to form and transmit this light sheet. Typically, an arrangement of one negative focal length cylindrical lens (expanding the beam) and two orthogonal positive cylindrical lenses (converging) are used or, alternatively, an arrangement of a negative spherical lens, a positive cylindrical lens and a positive spherical lens.

4.2.3 Image interrogation

For the imaging of the particles it is important to realize that the imaging is limited by diffraction due to the small particle diameters implying that the wavelength λ of the light has an influence on the size of the particle image as well as the aperture of the camera. Assuming a thin, single lens and a distance of d_i between the sensor and the lens the criterion for focussing on a particle at distance of d_o from the lens is given by equation 4.8 where f is the

focal length.

$$\frac{1}{f} = \frac{1}{d_i} + \frac{1}{d_o} \tag{4.8}$$

Besides the focal length, wavelength and aperture, the ratio between object distance d_o and sensor distance d_i is an important parameter characterizing the set-up of the imaging system and is termed the magnification M, as defined in equation 4.9. Equivalently, the magnification can be expressed as the ration between the linear dimensions of the field of view and the physical sensor size.

$$M = \frac{d_i}{d_o} \tag{4.9}$$

The typical diameter of a particle in the image d_τ is then given by equation 4.10, where the geometric image of the particle Md_p is often negligible compared to the diffraction limited image diameter $d_{diff} = 2.44 f_\#(M+1)\lambda$.

$$d_\tau = \sqrt{(Md_p)^2 + d_{diff}^2} \tag{4.10}$$

Finally, the depth of field δ_z should be greater than the thickness of the light sheet to have all particles in focus and can be estimated by equation 4.11. A large value of the numerical aperture is desired to obtain a higher depth of field while a small value has a positive effect on the light intensity collected by the sensor, posing another trade-off which is especially critical for recordings at high repetition-rates where the power per light pulse decreases.

$$\delta_z = 2 f_\# d_{diff}(M+1)/M^2 \tag{4.11}$$

4.2.4 Image interrogation procedures

To find the shift of the tracer pattern between two frames recorded at a known time separation of Δt, the cross-correlation operator is applied and the correlation peak indicates the particle shift Δx in units of pixels. Since the velocity is usually not uniform over the entire interrogation region, the area is subdivided into so-called correlation windows of a certain size, with or without overlap between the individual correlation windows, leading to an increase of velocity vector resolution. The minimum size of the correlation windows is limited by the criterion for the minimum number of tracer particles required for accurate and reliable cross-correlation and with that on the seeding density and magnification. With known particle shift Δx, time separation Δt, magnification factor M and physical pixel size l_{px} which is a property of the sensor, the average velocity of a fluid in the correlation volume is determined by 4.12. The influence of magnification and pixel size is attributed for during the calibration procedure. $\epsilon \approx 1px$ is a constant error which becomes dominant for small time separation Δt.

$$U = \frac{\Delta x M l_{px}}{\Delta t} + \frac{\epsilon M l_{px}}{\Delta t} \tag{4.12}$$

Now, in general a higher vector resolution is desired, requiring small correlation windows without large overlap to obtain statistically independent velocity vectors. This requirement

gives rise to the problem that tracer particles might travel further than the linear dimension of the correlation window during the defined time separation, making cross-correlation between the correlation windows impossible as long as the windows are centred on identical pixels in both frames. This effect decreases the signal-to-noise ratio and is called loss-of-correlation. A solution to this issue is the so-called multi-pass iteration procedure, in which the correlation process is repeated for windows of different sizes. A relatively large window is used in the first step generating an initial guess for the velocity vector which is used to apply a shift between the correlation windows in the second iteration step. Now, it is possible to reduce the correlation window size in the second iteration step without losing the correlation peak. The particle displacement must not be too small since this decreases the accuracy due to the constant error ϵ.

In order to improve the image quality and therefore the quality of the cross-correlation, certain pre-processing operations are often applied to the raw images recorded by the cameras. Pre-processing includes the subtraction of the time minimum for each individual pixel in order to remove spurious light. Furthermore, normalisations such as multiplication by a constant and division by the average are used to increase the reliability of vectors close to reflecting surfaces.

Post-processing of the vector field includes smoothing filters based for instance on Gaussian kernels to remove for subsonic flows non-physical discontinuities in the data.

4.2.5 Stereoscopic PIV

In the stereoscopic PIV technique two cameras are used to measure the three velocity components in a planar field of view illuminated by the light sheet of the laser. The cameras are arranged at different angles with respect to the field of view. From the frames recorded by each camera the velocity component of the particles which is orthogonal to the optical axis of the camera can be derived by means of cross-correlation. Using information about the positioning of the cameras, which is obtained by calibration and self-calibration, the velocity vectors in the plane of the light sheet can be computed. In order to correlate particles travelling normal to the light sheet its thickness is usually chosen greater than in the case of 2C-PIV.

4.2.6 Tomographic PIV

Tomographic PIV is a very recent technique which allows for 3-dimensional imaging with velocity vectors in all three dimensions. Availability of high-speed lasers and cameras offers the possibility to record time-resolved 3-dimensional flow images which can be seen as a full description of the velocity field in the limits of measurement accuracy and resolution. An early study on the use of tomographic PIV, also with application to turbulent boundary layers, was performed by Elsinga (2008).

A difference with respect to the 2C-PIV and Stereo-PIV techniques described above is that a volume has to be illuminated in contrast to a plane as it is the case for the other techniques, which can lead to limitations on the extent of the volume caused by restrictions in available laser power. Maximum use of the emitted light beam can be made by using an amplification system consisting of two mirrors on either side of the illuminated volume which create multiple reflections of the beam, which makes it unnecessary to expand the beam to large diameters leading to a dramatic loss in intensity.

The post-processing features a fundamental difference to the other PIV techniques in that at first the position of particles in the 3-dimensional space has to be reconstructed from the 2-dimensional frames recorded by multiple cameras. Due to the necessity to reconstruct the location of every single particle in space, the seeding density has upper limits above which the reconstruction quality decreases rapidly due to the presence of ghost particles. Typical seeding densities are between $0.05ppp$ and $0.1ppp$. Consecutively, the 3-dimensional cross-correlation function can be evaluated to yield a correlation peak between two adjacent frames and with that a displacement vector.

Chapter 5

Experimental set-up

In this study, the flow structure and its effect in terms of noise generation at the serrated trailing-edge of a NACA 0012 airfoil is investigated and compared to the straight trailing-edge. The experiments conducted for this purpose can coarsely be divided in two categories: Noise measurements and flow field measurements, where the latter includes besides PIV measurements also surface pressure measurements. Noise measurements aim to determine the effect of serrations and influence of certain design parameters with respect to noise reduction, while flow measurements seek to determine the cause, properties and mechanisms that lead to this effect. An overview of the experiments with reference to the sections containing detailed information is given in table 5.1.

For the above mentioned noise measurements, the vertical low turbulence wind tunnel facility (V-Tunnel, section 5.1.1) together with a relatively large number of models, namely 12 serrations and the straight trailing-edge (section 5.2.1), was used. Due to the more stringent requirements on model quality and time limitations for flow measurements, which were conducted in the open-section low speed W-tunnel (section 5.1.2) the range of models was reduced to include three serrations and the straight trailing-edge (section 5.2.2).

Table 5.1: Overview of experiments

Description	Model	Facility	Section
Far-field noise measurements	12 serrated and straight TE	V-Tunnel	section 5.3
2C-PIV	straight TE	W-Tunnel	section 5.4
Stereo-PIV	3 serrated TE	W-Tunnel	section 5.5
Tomo-PIV	3 serrated and straight TE	W-Tunnel	section 5.6
Surface pressure measurements	3 serrated and straight TE	W-Tunnel	section 5.7

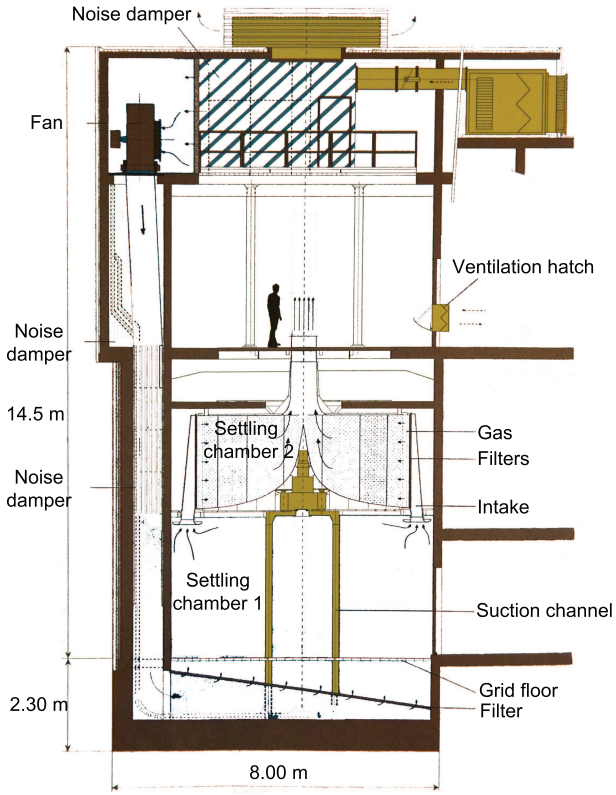

Figure 5.1: Vertical low turbulence wind tunnel

5.1 Experimental facilities

All experimental facilities and equipment used for this study is located at Delft University of Technology. For far-field noise measurements the vertical low turbulence wind tunnel facility is used due to the quiet overall sound level compared to the other facilities available. All PIV measurements are carried out in the W-Tunnel located in the High-Speed Laboratory.

5.1.1 V-Tunnel

The V-Tunnel, which stands for vertical low turbulence wind tunnel facility, is located at the low Low Speed Laboratory of Delft University of Technology. A schematic of the facility is shown in figure 5.1, presenting the unconventional layout extending over four floors.

Test section and control area are located on the third floor with the free stream directed upward towards the ceiling. Air enters the test section through a circular exit nozzle in the middle of the chamber with a diameter of $0.6m$. The large settling chambers located below the test section allow for a large contraction ratio and therefore for a high flow quality in terms of turbulence level which is specified to be smaller than $u'_{rms}/U_\infty < 0.1\%$.

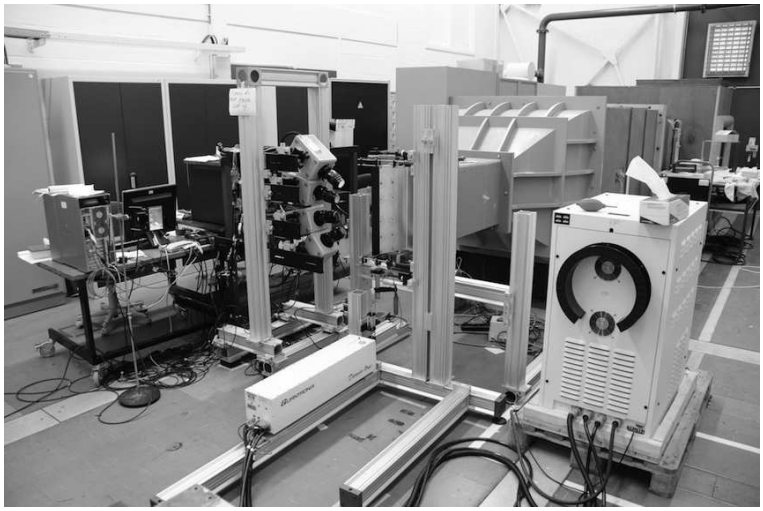

Figure 5.2: Open-section low-speed facility W-tunnel

For aeroacoustic experiments the V-Tunnel is the first choice due to a relatively low background noise level at low flow velocities. At the high end the facility has a maximum velocity of $45\frac{m}{s}$, where the background noise level dominates due to structural vibrations inside the testing chamber and at the ceiling.

5.1.2 W-Tunnel

The PIV and surface pressure measurements are conducted in the W-tunnel, an open-section low-speed wind tunnel at the High Speed Laboratory of Delft University of Technology. Figure 5.2 shows a photograph of the facility.

Air flows from the inlet in the form of a plenum ($2 \times 1.5 \times 2m^3$) through a decelerating diffuser into the settling chamber, where two grids contribute to a reduction in turbulence intensity ($u'_{rms}/U_\infty < 0.2\%$). Behind the settling chamber the flow enters the contraction nozzle where acceleration takes place and finally enters the test section through the tunnel exit nozzle ($0.4 \times 0.4m^2$). It has been shown that the part of the flow in the central part of the exit area ($0.32 \times 0.32m^2$) can be treated as uniform. The pressure difference driving the flow is created by a centrifugal fan driven by an electrical motor ($16.5kW$). Based on experience, the minimum stable velocity of the W-tunnel is about $5m/s$. Prior to the experiments the W-Tunnel was calibrated using a simple 2-Component PIV set-up. Figure 5.3 shows the results relating the shaft speed to the measured free-stream velocities.

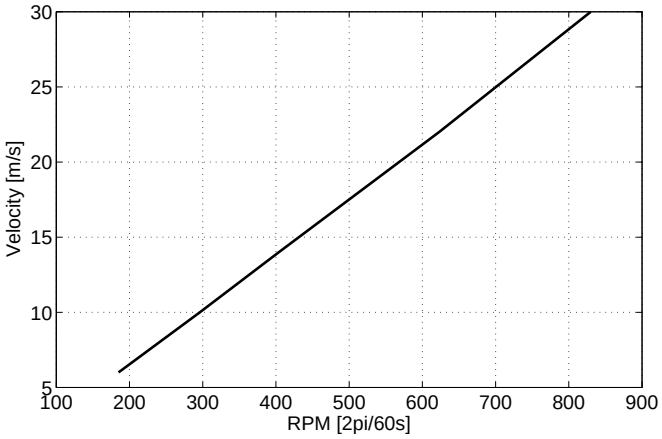

Figure 5.3: Calibration of W-tunnel

5.2 Airfoil and trailing-edge models

An airfoil with a NACA 0012 profile and a chord length of $c = 400mm$ is used as the baseline model for all experiments. A tripping wire is placed at $0.3c$. The model airfoil is designed such that the trailing-edge part of $60mm$ length ($> 0.85c$) is modular and can be exchanged easily. A slot at the blunt trailing-edge of the airfoil's main part allows for the attachment of the trailing-edge sections.

Figure 5.4(a) shows a typical trailing-edge model and the characteristic dimensions of the chevrons: First, the serration length $H = 2h$ equals twice the serration amplitude h. Second, the serration angle Φ is the angle between the free-stream flow direction and the serration edge. A third parameter is the serration wavelength $\lambda = 2H \tan \Phi$, e. g. the distance between the tips of two adjacent tips. Any two of the parameters mentioned above can be defined independently, yielding different serration designs. In this work the serration length H and the serration angle Φ are used as the independent parameters to define the designs.

5.2.1 Models for far-field microphone measurements

For the far-field acoustic measurements the baseline airfoil model and trailing-edge models are produced from foam (StyroDur, see figure 5.4(b)) using a hot-wire cutting technique. Two-dimensional profiles are cut from foam blocks by tracing the outline of the model with thin wire which is heated through the Joule effect, therefore melting the foam in its proximity. When the foam blocks match the shape of the NACA 0012 profile and have solidified, glue is applied to attach a thin foil covering the rough surface of the cut foam and thus smoothing the surface of the airfoil. In case of the trailing-edge models, the serrations are cut by knife in the final step of the manufacturing process after applying the surface cover. Unsupported estimates of inaccuracies occurred during the process which are summarized in the list below:

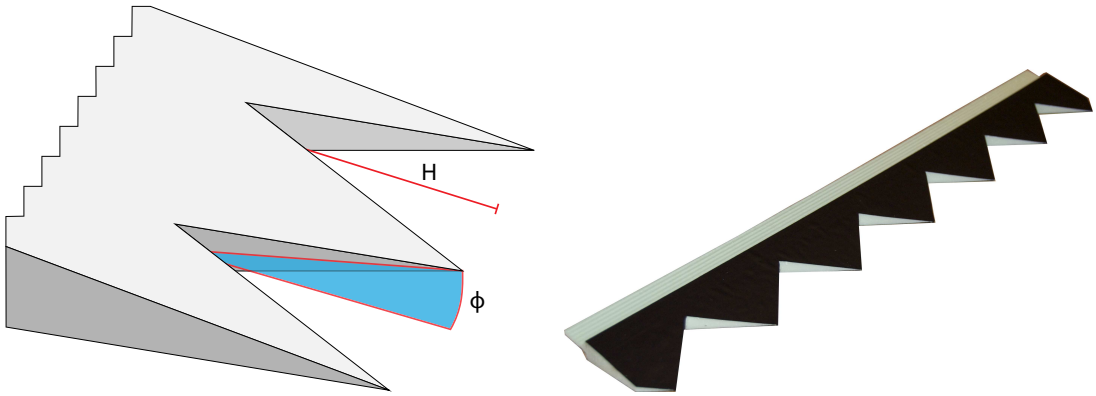

(a) Parameters describing geometry of serrations

(b) Photograph of serration models made of foam

Figure 5.4: Model of the serrated trailing-edge

Table 5.2: Trailing-edge models for acoustic measurements: Constant H

$H[mm]$	$\Phi[deg]$	$\lambda[mm]$
50	10	17.6
50	20	26.4
50	30	57.7
50	40	83.9
50	50	119.2

- Deviations in serration amplitude and length due to limited measurement accuracy and knife thickness ($\pm 1mm$)
- Inaccuracies in the shape of the surface due to bumps created by undesired agglomeration of glue ($< 0.5mm$)
- Inaccuracies in hot-wire cutting process, especially at sharp and thin edges ($\pm 1mm$)

Requiring a high accuracy, the above inaccuracies cannot be neglected. However, it is the purpose of this experiment to explore the general behaviour of serrated trailing-edges with respect to noise reduction and to test if previous results can be reproduced for the models at hand.

In order to investigate the influence of the different design parameters on the noise production, two series of serrated trailing-edges are tested in the V-Tunnel: Table 5.2 lists the design parameters of the models in the first series with constant serration length $H = 50mm$ but varying serration angle Φ from 10° to 50°.

The parameters of the models belonging to the second series are listed in table 5.3 with a constant serration angle $\Phi = 30°$ but instead varying serration length H from a minimum

Table 5.3: Trailing-edge models for acoustic measurements: Constant Φ

$H[mm]$	$\Phi[deg]$	$\lambda[mm]$
10	30	11.5
20	30	23.1
30	30	34.6
40	30	46.2
50	30	57.7

Table 5.4: Trailing-edge models surface pressure and PIV measurements

$H[mm]$	$\Phi[deg]$	$\lambda[mm]$
40	14	20
40	32	50
40	45	80

of $10mm$, resembling closely a straight trailing-edge, and a maximum of $50mm$ which has a considerable bluntness. For reference, apart from the two types of series described above also a straight trailing-edge model and the blunt version of the baseline airfoil without attached trailing-edge model are tested.

5.2.2 Models for surface pressure and PIV measurements

A high surface quality and manufacturing precision is desired for the models used during PIV and surface pressure measurements since slight inaccuracies can alter the boundary layer characteristics and organisation of the flow. Aluminum models are produced by CNC machining, which implies a higher cost per model. Therefore the range of models has to be restricted to a smaller selection. The base model, the NACA 0012, and the chord dimension of $c = 0.4m$ is identical to the parameters of the models used for far-field measurements.

Since the serration angle Φ is the main design parameter according to Howe's theory, the selection focuses on covering a range of serration angles with constant serration length which are given in table 5.4. The design of the mechanism for trailing-edge attachment differs slightly with respect to the foam models since bolts have to be used for attachment.

Although experiments have been conducted on all of these models, the results presented here will focus on the $\Phi = 14^\circ$ model, which has the greatest noise reduction potential as reported in literature and found in the current investigation.

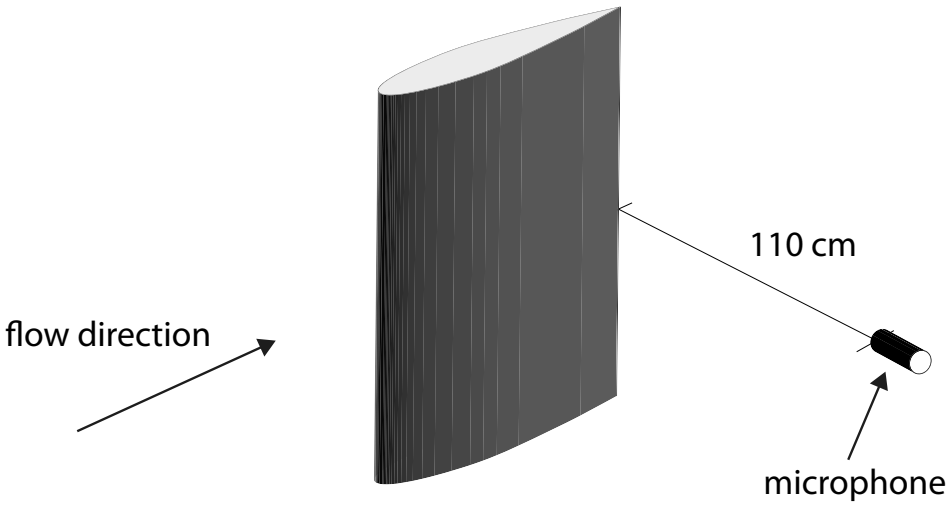

Figure 5.5: Schematic of set-up for acoustic measurements

5.3 Experimental arrangement for far-field microphone measurements

Far-field microphone measurements are carried out in the V-Tunnel facility described in section 5.1.1 due to its quiet background noise level compared to other low-speed facilities available at Delft University of Technology. The model is mounted horizontally with the leading edge pointing downwards at a distance of about $10mm$ from the exit nozzle of the wind-tunnel.

Figure 5.5 shows a schematic of the set-up for the acoustic measurements while figure 5.6 shows a photograph of the implementation including the presence of acoustic dampers material, which was used in order to reduce the reflections from walls, pillars and other structural elements and reduce the background noise level. Nevertheless, reflections and a relatively high background noise level due to electric devices present in the test chamber and aeroacoustic interactions with the surrounding structures pose an obstacle for accurate acoustic measurements. A single microphone is mounted at a distance of $1100mm$ from the trailing-edge at the center of the span normal to the chord plane, therefore fulfilling the far-field condition given in section 4.1.1 for $\lambda_a << 2\pi 1100mm \approx 6900mm$, i. e. for frequencies exceeding $50Hz$.

Tests were conducted at free-stream velocities of $15m/s$, $25m/s$ and $35m/s$ for which the experimental parameters are listed in table 5.5. The velocities are adjusted using a pitot tube which is shown in figure 5.7(a).

For the noise measurements a CESVA MX005 0.5" pre-amplified microphone, shown in figure 5.7(b), was used, which posses a linear range from $1Hz$ up to $20kHz$. It is connected via an amplifier and data acquisition board with D/A-converter to a data storage unit. For control of the data acquisition, calibration and adjustments a LABVIEW program is used.

The microphone is calibrated recording the output of a defined noise source of $114dB$ at $220Hz$

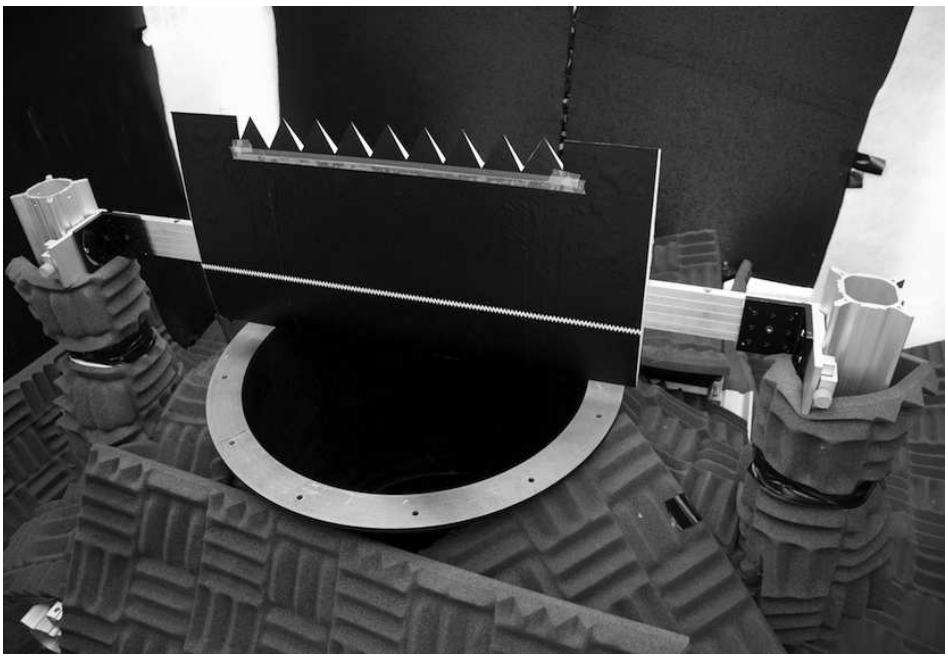

Figure 5.6: Photograph of acoustic measurements

Table 5.5: Experimental parameters for far-field measurements

$q_\infty[Pa]$	$M_\infty[-]$	$U_\infty[m/s]$	$Re_c[-]$
140	0.04	15	$400,000$
390	0.07	25	$666,667$
765	0.10	35	$933,333$

and consecutively relating the measured mean voltage output of the time-varying signal to the known pressure input resulting in the sensitivity of the microphone which is assumed to be constant over range of measured frequencies. Measurements are acquired at a sampling frequency of $20kHz$ and a duration of $10s$ yielding a time-series of $200,000$ samples. The noise level of the MX005 is specified to be less than $40dB$ relative to a reference pressure of $20\mu Pa$ over the linear frequency range.

After subtracting the mean and applying the calibration the power spectrum is computed using Welch's method. The lower limit pressure disturbance of human hearing, i. e. $p_{ref} = 20\mu Pa$, is used as a reference for conversion to decibels.

(a) Pitot tube in V-Tunnel (b) CEVRA MX005 microphone

Figure 5.7: Measurement instruments for far-field microphone experiments

5.4 Experimental arrangement for 2-Component PIV

PIV measurements are carried out in the low speed, open-section facility (W-Tunnel, described in section 5.1.2) of the Aerodynamics Department at Delft University of Technology at a free-stream velocity of $U_\infty = 14m/s$ or $M = 0.04$. Since apart from statistical data also time-resolved sequences are desired for the stereoscopic and tomographic PIV experiments described in the following sections, a high-repetition rate PIV system is used. The purpose of the 2C-PIV experiments is to determine the statistical boundary layer properties close to the trailing-edge.

For structural reasons and convenient positioning of laser and camera, the NACA 0012 airfoil model is placed vertically at the center of test section with its leading edge at a distance of about $5mm$ from the exit nozzle of the wind tunnel. A tripping wire is placed at $120mm$ distance from the leading edge, equivalent to $0.3c$, to ensure the transition from a laminar to a turbulent boundary layer. Geometrical blockage based on the maximum thickness of the airfoil ($0.12c$) and the nozzle exit area of $400 \times 400mm^2$ is 12%. For this configuration XFoil computes a boundary layer thickness of approximately $\delta = 10mm$ at the trailing-edge, corresponding to a flow time-scale of about $T = \delta/U_\infty \approx 70\mu s$ as shown in table 5.6 together with other parameters relevant for the experiment.

Seeding of the flow is provided by a SAFEX smoke generator located in the plenum of the wind-tunnel which produces droplets of a size of about $1\mu m$. Assuming a density of about $10^3 \frac{kg}{m^3}$ the relaxation time defined in section 4.2.1 is $\tau_s = d_p^2 \frac{\rho_p}{18\mu} = 3\mu s$. The resulting Stokes number is $St = \frac{\tau_s}{T} = 0.04 < 0.1$ fulfilling the criterion for tracing particles to accurately follow the flow.

Sufficient illumination is accomplished by a Quantronix Darwin-Duo dual cavity laser high-repetition rate system with a maximum pulse frequency of $10kHz$ emitting visible green light at a wavelength of $527nm$. The average power output of the system is $80W$ at $3kHz$ leading

Table 5.6: Experimental parameters

Parameter	Quantity
M_∞	0.04
U_∞	$14m/s$
c	$40mm$
$\frac{x_{tr}}{c}$	0.3
δ	$\approx 10mm$
$\delta^\star$	$\approx 2mm$
Re_δ	$\approx$9250
Re_θ	≈ 1500
Re_c	$370,000$

Table 5.7: Recording parameters 2C-PIV

Flow geometry	perpendicular to trailing-edge
Velocity	$14\frac{m}{s}$
Field of view	$50 \times 50mm^2$
Magnification	≈ 0.4
Interrogation volume	$0.3 \times 0.3mm^2$
Dynamic velocity range	$0 - 15\frac{m}{s}$
Recording method	double frame / single exposure / $100Hz$
Recording medium	Photron Fastcam SA1
Recording lens	$f = 105mm$, $f_\# = 2.8$
Illumination	Nd:YLF laser, $2 \cdot 15mJ$ per pulse at $2.7kHz$
Pulse delay	$42\mu s$
Seeding material	non-toxic water-glycol based fog ($d_p \approx 1\mu m$)

to an equivalent pulse energy of about $2 \cdot 15mJ$ at a rate of $2.7kHz$. Laser and optics are located in the flow sufficiently far downstream such that the boundary layers on both sides of the airfoil are illuminated. Light-sheet optics consist of a $+200mm$ spherical lens, a $-150mm$ spherical lens and a $-80mm$ cylindrical lens arranged in this order. Laser pulse separation between two frames is $dt = 42\mu s$, which is equivalent to a freestream displacement of about $0.6mm < 1mm$ or a velocity dynamic range of $VDR = \Delta U_{max}/\epsilon \approx 120$ based on a minimum measured velocity of about $0.6U_\infty$ and on a measurement error of $\epsilon \approx 0.1px$.

The measurement plane is located in the at the mid-span of the airfoil in the chord-wall-normal plane and has linear extensions of approximately $50 \times 50mm^2$. A high-speed camera of type Photron Fastcam SA1 with a $1024 \times 1024px$ sensor resolution and a pixel-pitch of $20\mu m$, equivalent to a sensor size of approximately $20.5 \times 20.5mm$, is located under the airfoil with the optical axis pointing upwards as can be seen in the schematic in figure 5.8, while figure 5.9 shows a photograph of the implementation. Therefore, the optical magnification is about 0.4. This type of camera allows the recording at full sensor size in double-frame mode for frequencies up to $2.7kHz$. The camera is equipped with a Nikon lens with fixed

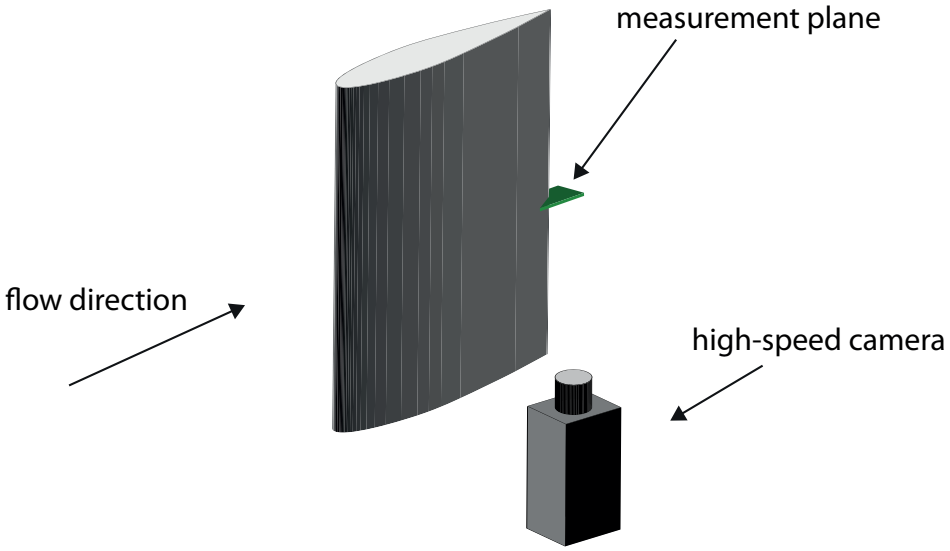

Figure 5.8: Schematic of set-up for 2C-PIV

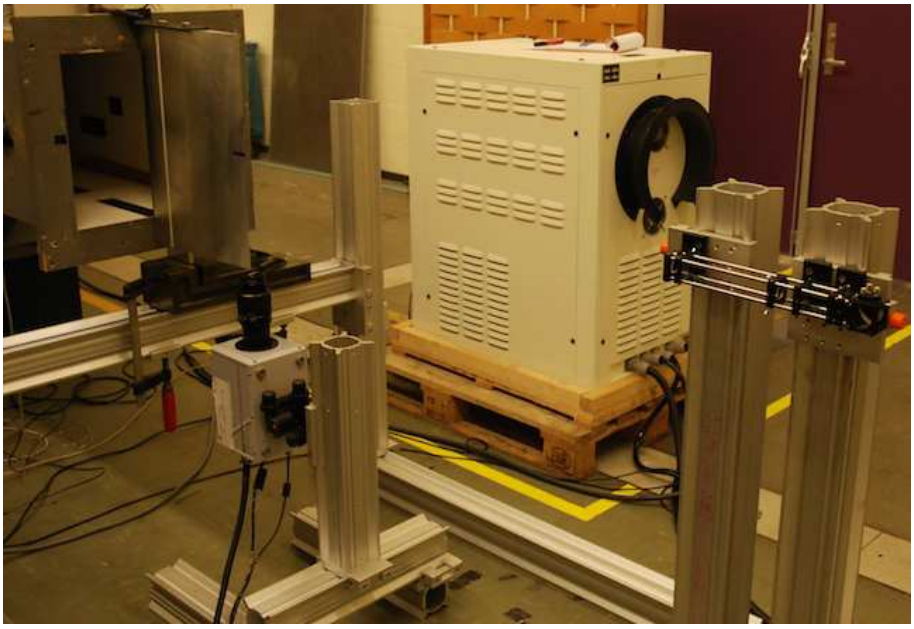

Figure 5.9: Set-up of 2-Component PIV system

focal length of $105mm$ adjusted to a numerical aperture of $f_{\#} = 2.8$. In order to avoid peak-locking the particle images are slightly defocussed to yield particle image diameters of about $2px$. An overview of the parameters related to digital recording is provided in table 5.7.

For the statistical evaluation of the boundary layer properties, 1000 images are recorded in double-frame mode at a frequency of $100Hz$. For recording LaVision Davis 7.2 is used while for processing version 7.4 is used. In a pre-processing step the minimum intensity in the time series for each pixel is subtracted to remove reflections from surfaces present in the

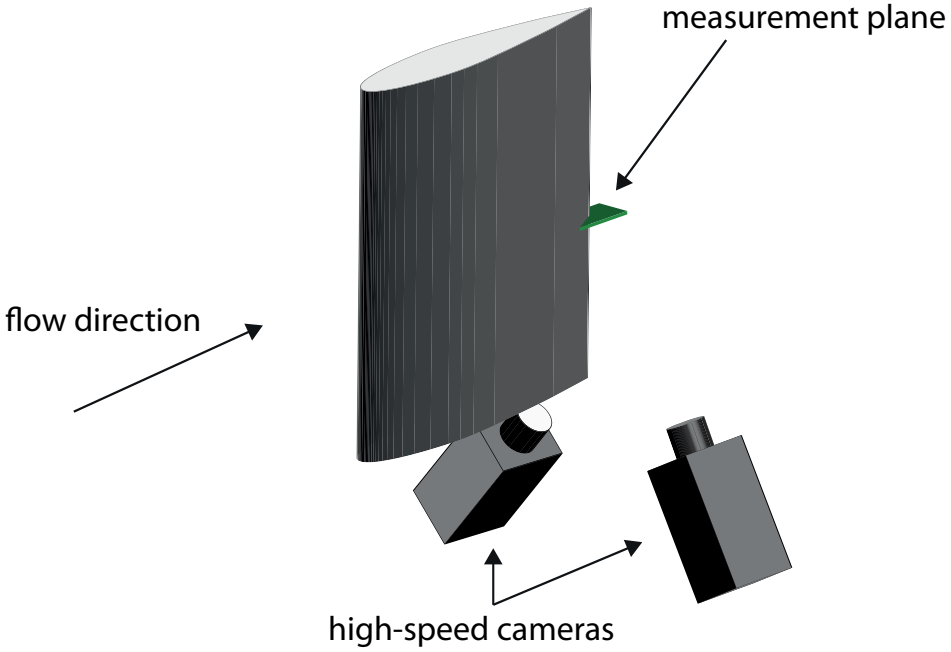

Figure 5.10: Schematic of set-up for stereoscopic PIV

measurement volume. Consecutively, the images are normalised by a time average. The velocity vector fields with a final correlation window size of $6px$ by $6px$ with an overlap of 75%, yielding a vector spacing of approximately $0.073mm$.

5.5 Experimental arrangement for stereoscopic PIV

Also stereoscopic PIV measurements are carried out in the low speed, open-section facility to capture the flow in the streamwise-wall-normal plane between the serrations. To achieve a high repetition rate the high-repetition PIV system consisting of a Quatronix Darwin-Duo dual cavity laser high-repetition rate laser system and two Photron Fastcam SA1 cameras with the specification as mentioned in section 5.4 is used. The velocity is set to $U_\infty = 14m/s$ or $M = 0.04$ as before and therefore the parameters in table 5.6 characterize the experiment. To capture the vortices shed from the blunt part of the trailing-edge in between the serrations is the the primary purpose of this experiment.

Figure 5.10 shows a schematic of the experimental set-up for the stereoscopic PIV measurements while figure 5.11 shows shows photographs of the implementation including the coordinate axes spanning the light-sheet plane. The two cameras are positioned on both sides below the airfoil with the optical axes pointing upwards at an angle of approximately 45° with respect to the trailing-edge. Additionally, the cameras are equipped with Scheimpflug and narrow band-pass filters to filter ambient light at low frequencies. In focus is a plane between the serrations, close to the center of the span, at the middle between root and tip of the tooth exposed to the view of the cameras with linear extensions of approximately $50mm \times 50mm$.

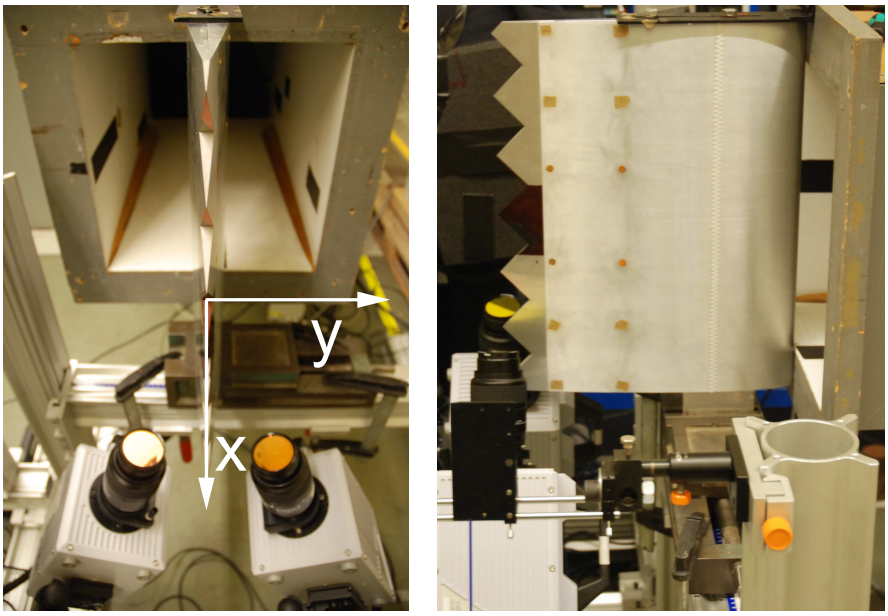

(a) View from back with coordinate system

(b) Side-view showing use of knife edge

Figure 5.11: Photographs of experimental set-up for stereoscopic PIV

During the recordings the numerical aperture of the cameras is set to $f_{\#} = 5.6$.

The laser and light-sheet optics ($-150mm$ spherical, $200mm$ spherical, and $200mm$ cylindrical lenses in this order) are positioned at one side of the airfoil outside the flow. To prevent reflections from the surface a knife edge, which can be seen in figure 5.11(b), is used to cut the light-sheet appropriately. Pulse separation between the recording is $42\mu s$ to achieve a high dynamic range. 1000 images are recorded at a rate of $2.7kHz$ which are used for an analysis of the frequency spectrum while 1000 images recorded at a rate of $100Hz$ are used for statistical analysis. Parameters related to the digital image recording of the stereoscopic PIV experiments are summarized in table 5.8.

Apart from the initial calibration step and the pre- and post-processing of the data is similar to the procedure described in the previous section. However, the correlation window in this case is set to $16px \times 16px$ with an overlap of 50%. Using the time-resolved data at $2.7kHz$, the spectrum of velocity fluctuations is computed using Welch's method.

Table 5.8: Recording parameters Stereo-PIV

Flow geometry	plane between serrations
Velocity	$14\frac{m}{s}$
Field of view	$50 \times 50 \times 2mm^3$
Magnification	≈ 0.4
Interrogation volume	$0.78 \times 0.78 \times 2mm^3$
Dynamic velocity range	$0 - 15\frac{m}{s}$
Recording method	double frame / single exposure / $100Hz$, $2.7kHz$
Recording medium	2 Photron Fastcam SA1
Recording lens	$f = 105mm$, $f_\# = 5.6$
Illumination	Nd:YLF laser, $2 \cdot 15mJ$ per pulse at $2.7kHz$
Pulse delay	$42\mu s$
Seeding material	non-toxic water-glycol based fog ($d_p \approx 1\mu m$)

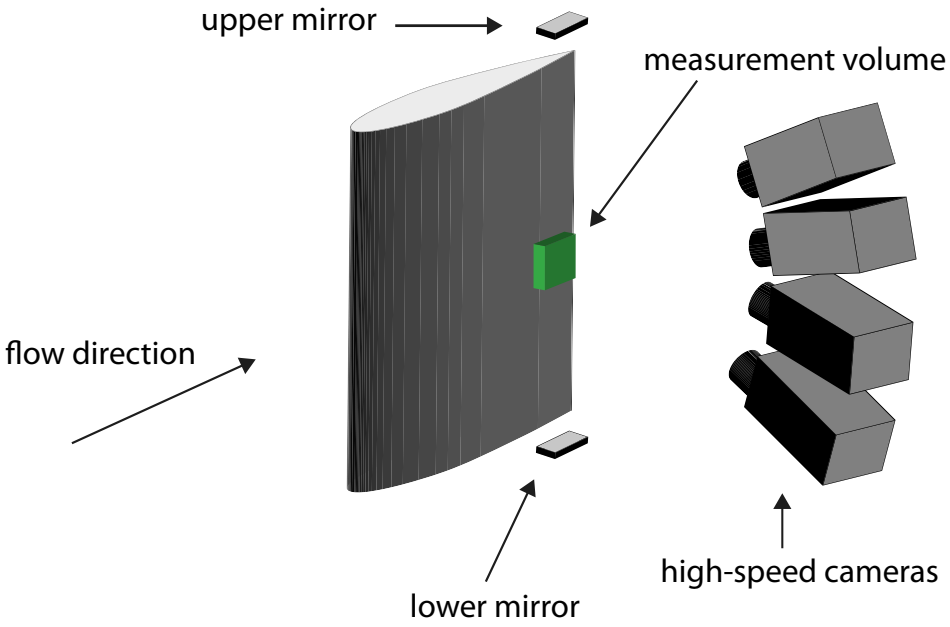

Figure 5.12: Schematic of set-up for tomographic PIV

5.6 Experimental arrangement for tomographic PIV

For tomographic measurements the configuration of the wind-tunnel and the positioning of the model is not changed compared to the experiments described in the previous sections. Figure 5.12 shows the experimental set-up including cameras and light-sheet optics, while figure 5.13 shows photographs of the implementation. Four cameras are positioned at angles of about $-40°$, $-15°$, $15°$, and $40°$ in the spanwise-wall-normal plane with $0°$ defined by the the wall-normal with respect to the local airfoil surface at the trailing-edge.

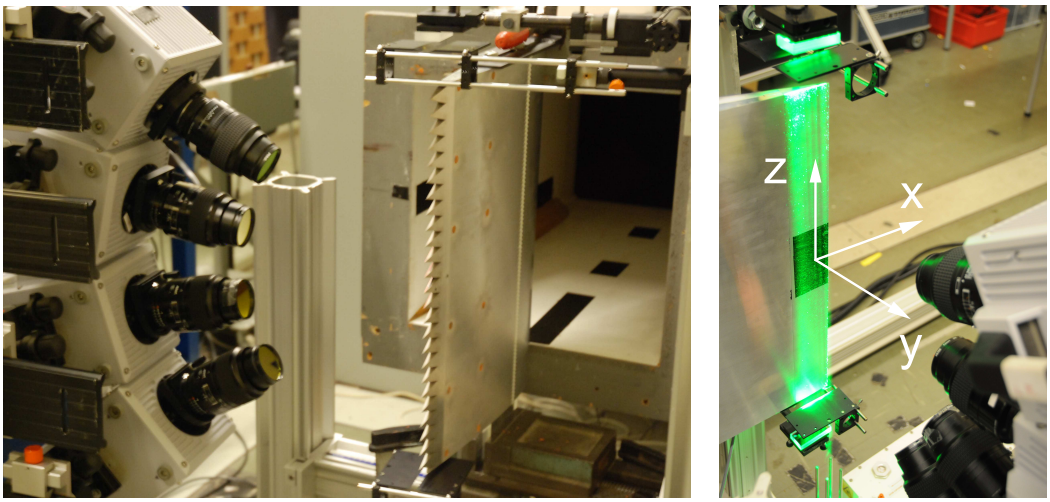

(a) Positioning of cameras, laser and model

(b) Illumination by multiple reflections and coordinate system

Figure 5.13: Photographs of experimental set-up for tomographic PIV

Light is emitted by a laser head positioned on the ground below the model, consecutively expanded and amplified by multiple reflections between two mirrors in such a way that the entire measurement volume is illuminated. Figure 5.13(b) depicts the illumination of the measurement volume and also indicates the coordinate system for the tomographic PIV reconstructions: The streamwise axis is denoted by the x-axis, the spanwise direction by the z-axis and the wall-normal by the y-axis, constituting a left-handed coordinate system. The set-up allows for testing at an angle of attack of 0°, −5° and +5°. Measuring at angles of attack different from 0° implies that the cameras has to be rotated horizontally to maintain the positioning of the cameras described above. A particle concentration of approximately $0.08ppp$ is applied during the experiments.

Linear extensions of the measurement volume are limited by the available laser power and desired resolution, leading to a compromise of $50 \times 50 \times 8mm^3$. The measurement volume is located flush to the trailing-edge surface of the airfoil. Statistical measurements are recorded at a frequency of $100Hz$ and time-resolved sequences at a frequency of $2.7kHz$. For the synchronisation between cameras, laser and the image acquisition system a LaVision programmable timing unit is used, which is controlled by the LaVision Davis 7.2 software also used for calibration.

Emitted from the laser head, the laser beam passes an arrangement of beam-forming optics consisting of a diverging lens ($-150mm$ spherical) and a converging lens ($+200mm$ spherical). To achieve illumination of the entire measurement volume a configuration of two mirrors located on the spanwise axis on each side of the airfoil reflect the beam multiple times, such that the reflections move towards the leading edge and back to the trailing-edge, where the light finally escapes. Due to the presence of a reflecting surface and in order to remove low-

Table 5.9: Recording parameters Tomo-PIV

Flow geometry	flush with surface at trailing-edge
Velocity	$14\frac{m}{s}$
Field of view	$50 \times 50 \times 8mm^3$
Magnification	≈ 0.4
Interrogation volume	$1.56 \times 1.56 \times 1.56mm^3$
Dynamic velocity range	$0 - 15\frac{m}{s}$
Recording method	double frame / single exposure / $100Hz$, $2.7kHz$
Recording medium	4 Photron Fastcam SA1
Recording lens	$f = 105mm$, $f_\# = 22$,16,16,22
Illumination	Nd:YLF laser, $2 \cdot 15mJ$ per pulse at $2.7kHz$
Pulse delay	$42\mu s$
Seeding material	non-toxic water-glycol based fog ($d_p \approx 1\mu m$)
Seeding density	~ 0.08

energy fringes at the outer regions of the circular beam knife-edge slit filters with a width of about $8mm$ in front of the mirrors are applied.

Four Photron Fastcam SA1 cameras are used for imaging. All cameras are equipped with Nikon lenses having a fixed focal length of $105mm$. Due to the increased scattering efficiency for the cameras at 40°, caused by forward and backward scattering as predicted by Mie's scattering theory, and more stringent requirements concerning the depth of field, the numerical aperture for the cameras at the extreme angles are set to $f_\# = 22$ while for the cameras in side scattering position it is set to $f_\# = 16$. Additionally, Scheimpflug adapters are used to place the focal plane in the mid-section of the measurements volume increasing the depth of field of the images and are adjusted according to the Scheimpflug condition. The parameters characterizing the tomographic PIV system used here are summarized in table 5.9.

Self-calibration, reconstruction and correlation of the data is accomplished using the LaVision Davis 7.4 software package. Self-calibration is applied to reduce the residual of the calibration to less than $0.1px$, therefore increasing the quality of the reconstruction. The raw images are pre-processed by subtracting the time-minimum background and a sliding spatial minimum with a kernel size of $51px$ before normalizing the image with a local average computed with a kernel size of $31px$. Reconstruction of the complete volume yields a volumetric resolution of about $1024 \times 1024 \times 164voxels$. Image cross-correlation is performed with a final interrogation volume size of $32 \times 32 \times 32voxels$ and about 16 particles per correlation volume (based on a seeding density of $0.08ppp$) and an overlap-factor of 75% resulting in a vector spacing of about $0.4mm$ ($\approx 0.04\delta$) and $1.6mm$ for independent vectors.

(a) Surface microphones mounted on modular patches

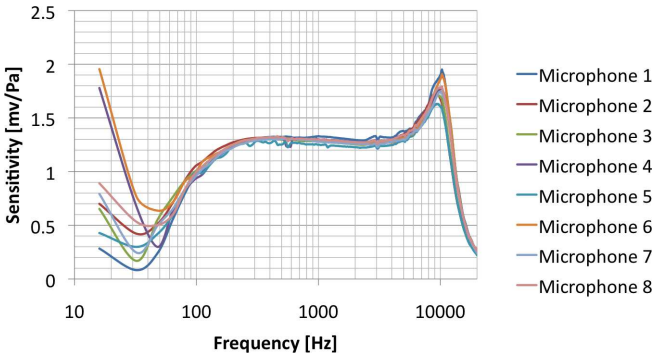

(b) Calibration curves

Figure 5.14: Microphones for surface pressure fluctuations measurements

5.7 Experimental arrangement for surface microphone measurements

Since part of the surface microphone measurements are recorded concurrently with the tomographic PIV measurements of the trailing-edge boundary layer, essentially the same set-up for airfoil, wind-tunnel and PIV system as described in section 5.6 is used. Additionally, the trailing-edge models are equipped with small electret condenser microphones of type SONION 66AC31, which are connected via an amplifier and data acquisition board to the data storage and control unit. Furthermore, the data acquisition unit is connected to the LaVision programmable timing unit for synchronisation with the PIV recordings. As for the far-field noise measurements a LABVIEW program is used to define the settings for the measurement procedure. Figure 5.14(a) shows two panels with four microphones attached to each of them, which can be mounted on the different trailing-edge models described in section 5.2.2.

The microphones have a small orifice of only $1.05 \times 0.45mm^2$ and are calibrated using a defined sound source with varying frequencies, producing the calibration curves shown in figure 5.14. As can be seen the microphones show a similar response from about $70Hz$ up

Table 5.10: Parameters for surface microphone measurements

Number of microphones	8 for straight TE, 4 for serrations
Sampling frequency	$40kHz$
Number of samples	$20,000$ with PIV / $200,000$ for statistics
Recording time	$0.5s/5s$
Spacing	$\approx 7.5mm$

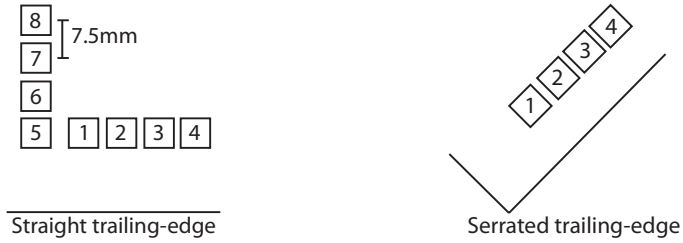

(a) Straight TE (b) Serrated TE

Figure 5.15: Arrangement of surface microphones

to about $8kHz$. For the measurements the sampling frequency is set to $40kHz$ and $20,000$ samples are recorded for simultaneous measurements with the PIV recordings, equivalent to $0.5s$, while $200,000$ samples are recorded for statistical purposes, equivalent to $5s$. Parameters related to the surface microphone measurements are summarised in table 5.10.

The microphones are mounted on the patches in figure 5.14(a) at a distance of about $7.5mm$ measured between the centres of the orifices. For serrated and straight trailing-edge models different numbers of microphones are used in different arrangements as shown in figure 5.15, which is useful for later reference.

Chapter 6

Noise and flow structure at the serrated trailing-edge

In the present chapter, the results of the experiments on noise generation and flow structure at the serrated trailing-edge will be discussed. Section 6.1 presents the results of the far-field noise measurements, explaining the peculiarities of the recorded spectra. Section 6.2 deals with the boundary layer statistics, before section 6.3 continues with the coherent structures at both the serrated and straight trailing-edge. Vortex shedding from blunt parts of the trailing-edge is elaborated on in section 6.4. In section 6.5 the results of the surface pressure measurements are presented. To complete the overall picture of the flow and differences to the straight trailing-edge, section 6.6 presents the average flow field.

6.1 Far-field noise reduction

Data used in this section has been obtained with the experimental set-up described in section 5.3. Figure 6.1 shows the power spectral density plots for the serrated trailing-edges with $\Phi = 10°$,$\Phi = 30°$ and $\Phi = 50°$ at three different velocities on the left side and for trailing-edge models with constant serration angle and varying serration length of $H = 11mm$, $H = 33mm$ and $H = 55mm$ on the right side. The power spectral density is plotted on the y-axis against frequency on the x-axis. Welch's algorithm is used to compute the spectra and a reference value of $p_0 = 20\mu Pa$ defines the level of $0dB$ as discussed in section 4.1.3. For the sake of comparison, data for the straight trailing-edge is added to each graph.

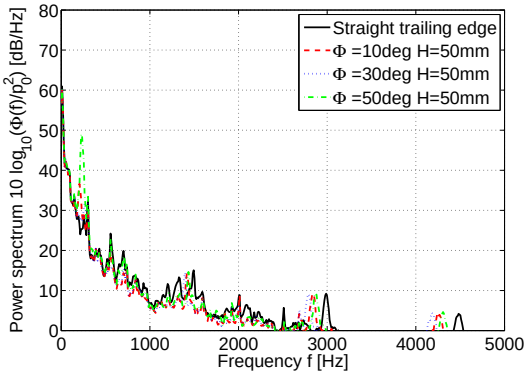

(a) constant $H = 50mm$, $U_{\inf} = 15m/s$

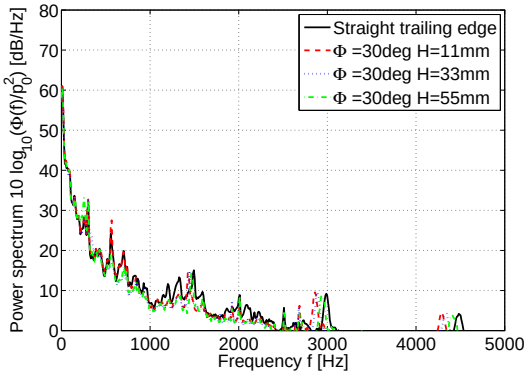

(b) constant $\Phi = 30°$, $U_{\inf} = 15m/s$

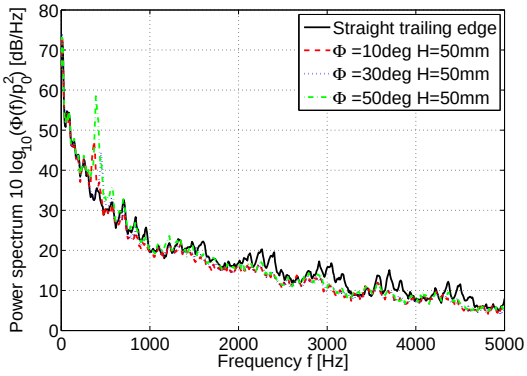

(c) constant $H = 50mm$, $U_{\inf} = 25m/s$

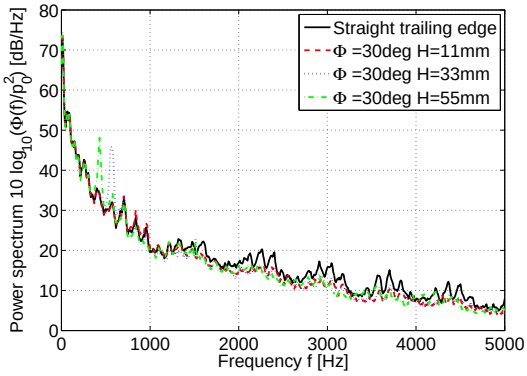

(d) constant $\Phi = 30°$, $U_{\inf} = 25m/s$

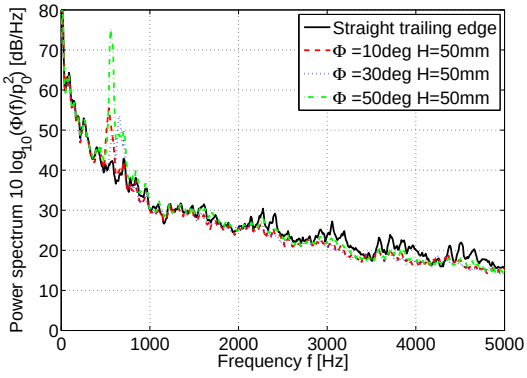

(e) constant $H = 50mm$, $U_{\inf} = 35m/s$

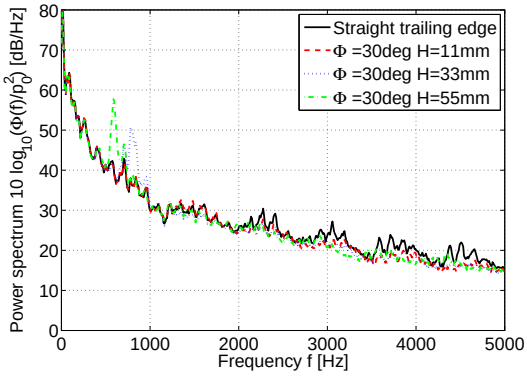

(f) constant $\Phi = 30°$, $U_{\inf} = 35m/s$

Figure 6.1: Noise power spectral density for different serrations and velocities

Most prominent feature in the spectra are the tonal peaks in the range from $250Hz$ to $1kHz$ which can be observed for all configurations except for $H = 33mm$ at $15m/s$ and for the shortest serration length $H = 11mm$ at all velocities, for which no distinct tonal peaks are present. Furthermore, a dependency of the frequency corresponding to the tonal peaks on the design parameters and the free-stream velocity can be observed, which will be treated in section 6.4.1. For now, it should be noted that the frequencies corresponding to the tonal peaks increase for smaller serration length and higher velocities, as predicted by the Strouhal dependency if the bluntness is assumed to be the appropriate length scale. As expected, these tonal peaks are a severe penalty for the performance of the serration design at hand with respect to overall noise reduction. The humps at multiples of the frequencies belonging to these peaks are presumably harmonics of the fundamental at the peak frequency.

From previous experiments and theoretical results presented in section 2.1.1 it is known that the sound pressure level of the broadband noise at the trailing-edge scales with approximately U^5, where U is the free-stream velocity. In the logarithmic plots shown in figure 6.1 this corresponds to a difference of $10log_{10}(U_1/U_2)^5 dB$ for frequencies exceeding $1kHz$, i. e. approximately $11dB$ between $15m/s$ and $25m/s$ and $7.6dB$ between $25m/s$ and $35m/s$, which matches the lower velocities but slightly underestimates the increase in the band sound pressure level for the higher velocities.

A better visualisation of the difference in noise levels is obtained by plotting the Third-Octave band power spectrum discussed in section 4.1.3. This processing has been performed for the data in figure 6.1 and the results are depicted in figure 6.2 showing the Third-Octave band power spectrum on the y-axis and the corresponding center frequencies on the x-axis. The difference of the serrated trailing-edges compared to the straight trailing-edge in terms of broadband noise becomes clear in the form of substantial reductions in the band from $1kHz$ to $5kHz$ for all serrated trailing-edge geometries as predicted by Howe's theory outlined in section 2.3. Reductions are on the order of $2 - 3dB$. Furthermore, it should be noted that by varying serration angles Φ depicted on the left side of figure 6.2 a marginal tendency of reduction in broadband noise level with decreasing serration angle can be observed while, as expected, this trend is absent for the graphs on the right side, where the serration angle is constant. Here, the noise levels in the broadband region coincide for varying serration length H.

Even for a serration angle of $\Phi = 50°$ a considerable reduction with respect to the straight trailing-edge broadband noise is observed. Due to the tonal peaks in the frequency band from $250Hz$ to $1kHz$ no tendency to reduction in overall sound pressure level for the serrated trailing-edge models with blunt parts could be detected as shown in figure 6.3, where the total sound pressure level is plotted against the design parameters. However, due to the absence of overall noise reduction alternatives such as flat plate attachments, as applied successfully by Oerlemans (2009), might be the preferred choice for practical applications.

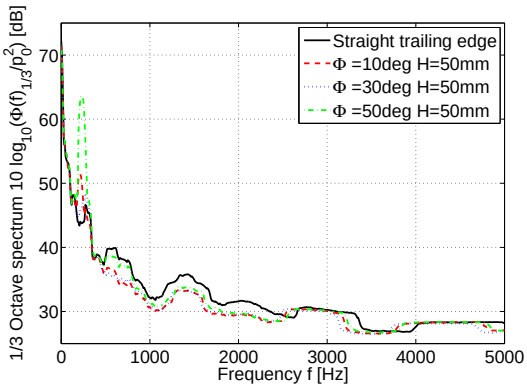

(a) Constant $H = 50mm$, $U_{\inf} = 15m/s$

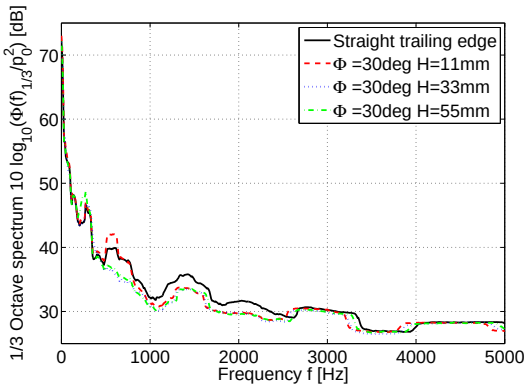

(b) Constant $\Phi = 30°$, $U_{\inf} = 15m/s$

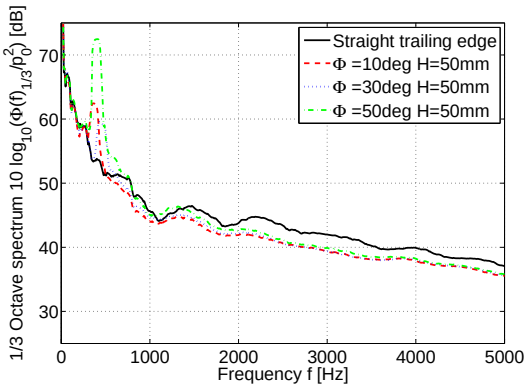

(c) Constant $H = 50mm$, $U_{\inf} = 25m/s$

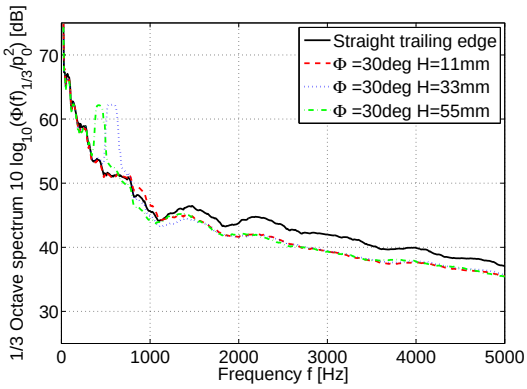

(d) Constant $\Phi = 30°$, $U_{\inf} = 25m/s$

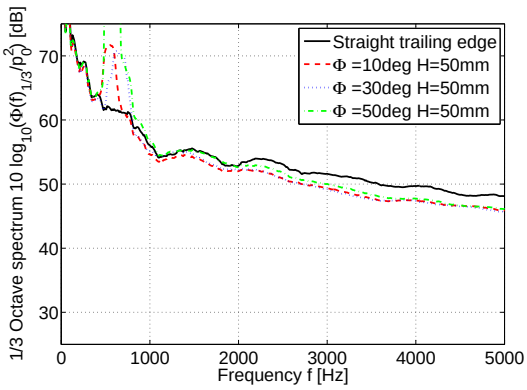

(e) Constant $H = 50mm$, $U_{\inf} = 35m/s$

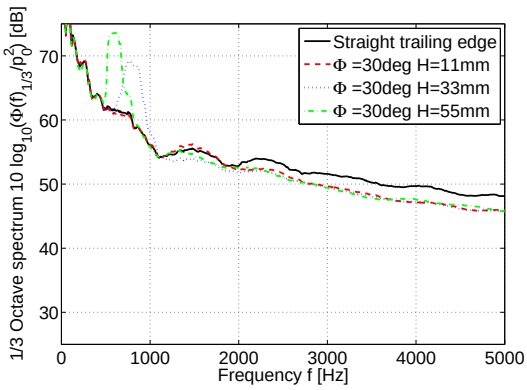

(f) Constant $\Phi = 30°$, $U_{\inf} = 35m/s$

Figure 6.2: Third-Octave band power for different serrations and velocities

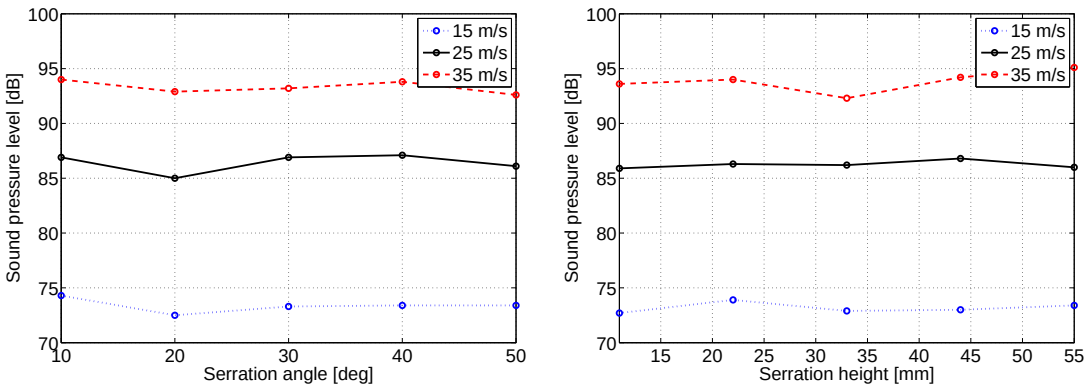

(a) Constant $H = 50mm$

(b) Constant $\Phi = 30°$

Figure 6.3: Total sound pressure level for different serrations and velocities

6.2 Characterization of the boundary layer

In this section the statistical properties of the boundary layer are determined. This serves the purpose to derive appropriate scaling parameters for non-dimensional quantities and to provide a reference for future experiments. In order to determine the appropriate order of the scaling parameters for the reference boundary layer at the straight trailing-edge, the two component PIV images recorded for the straight trailing-edge model are processed as described in section 5.4. Figure 6.4(a) shows the average velocity field in the vicinity of the trailing-edge.

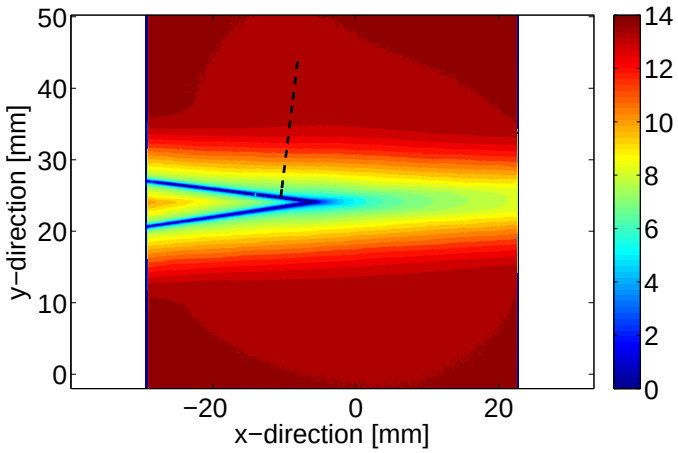

(a) Magnitude of average velocity field (m/s) for entire field of view

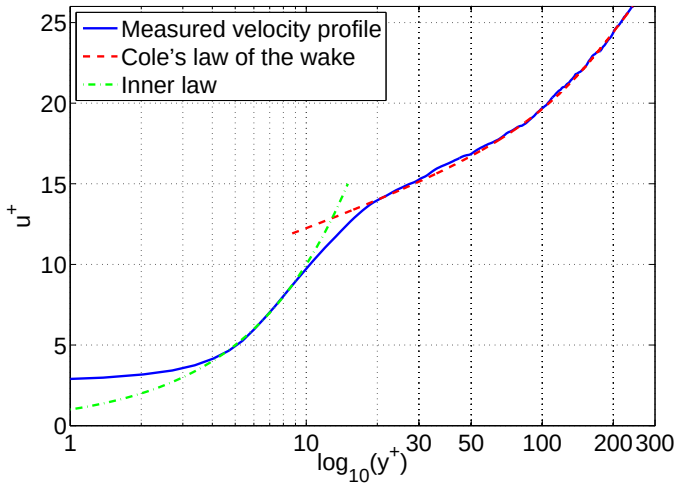

(b) Comparison of measured velocity profile and fit by Cole's law at $0.95c$

Figure 6.4: Boundary layer obtained by 2C-PIV, straight TE

The fitting procedure for the velocity profile in the outer region described in section 3.1 requires the boundary layer displacement thickness $\delta^\star$, the boundary layer thickness δ and the velocity outside of the boundary layer U_e provided in table 6.1 as input in order to determine the scaling parameters u_τ and δ_ν. Furthermore, the table lists the momentum thickness θ and the shape factor H. The boundary layer, displacement, momentum thickness and shape factor increase towards the trailing-edge, which is an indication of the adverse pressure gradient and transition to the wake.

Table 6.1: Boundary layer properties

$\frac{x}{c}$ [-]	δ [mm]	$\delta^\star$ [mm]	θ [mm]	H	U_e [m/s]
0.95	9.5	2.0	1.3	1.54	13.74
0.9625	10.2	2.2	1.4	1.55	13.65
0.975	11.0	2.4	1.5	1.58	13.58
0.9875	12.9	2.6	1.6	1.62	13.53

Table 6.2 presents the results for different locations in the vicinity of the trailing-edge. An example for the obtained fit in comparison to the measured velocity profile is shown in figure 6.4(b) for the location at $0.95c$. In the remainder of this report the values found for the location at $0.95c$ will be used for scaling operations.

The bluntness parameter defined in section 2.1.2 is estimated to be $\frac{t}{\delta^\star} \approx 5 \gg 0.3$ at the root of the serrations, indicating the dominance of shedding. Hence, as became apparent from the results presented in section 6.1 and the criterion in section 2.1.2 the influence of vortex shedding from the trailing-edge cannot be neglected.

Table 6.2: Scaling parameters

	Inner law		Cole's law of the wake	
$\frac{x}{c}$ [-]	u_τ [m/s]	δ_ν [mm]	u_τ [m/s]	δ_ν [mm]
0.95	0.498	0.030	0.547	0.027
0.9625	0.584	0.026	0.537	0.028
0.975	0.520	0.029	0.525	0.029
0.9875	0.437	0.034	0.529	0.028

At this point, one should note that the nominal extension of the interrogation volume of the tomographic experiments described in section 5.6 is $y = 0 - 8mm$. Due to border effects and illumination acceptable vectors are obtained in the region $y \approx 1.5 - 6.5mm$ as depicted in the context of the boundary layer structure in figure 6.5.

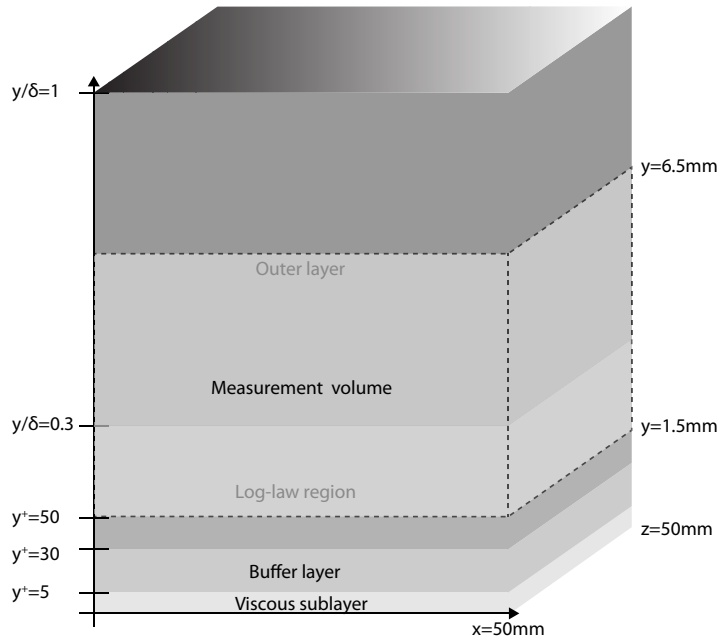

Figure 6.5: Location of measurement region inside turbulent boundary layer

6.3 Coherent structures

The coherent structures and motions have been reviewed in section 3.2 and can be identified in the instantaneous 3-dimensional velocity fields obtained by tomographic reconstruction. Data presented in this section was acquired and processed with the experimental set-up of the tomographic PIV system described in section 5.6. The Q-criterion of equation 3.6 is used to visualise vortical structures together with low-speed streaks of relatively low streamwise velocity. Some of the features described in chapter 3 can be observed in the boundary layer. For instance, figure 6.6 depicts an ejection process, a rapid upward movement of fluid, with the typical arrangement of low-speed streak and hairpin vortex. From left to right the sequence shows the hairpin on the back of a low-speed streak which grow while ejecting fluid. As the hairpin is stretched through the mean shear of the velocity profile and the induced upward motion of the fluid the ejection process seems to be intensified. Finally, the low-speed streak is lifted due to this induced upward motion. The ejection, visualised by a positive wall-normal velocity component, can virtually always be found in connection with growing vortices. Apart from the ejection process, the typical inclination of many hairpins and canes with respect to the wall can clearly be identified in the figure. The angle matches the value reported in literature with about $45° - 50°$. Several examples for the inclination of these structures can be seen in the following section.

6.3.1 Coherent structures near the trailing-edge

In this study a different shades are used to visualise the time development of coherent structures. Figure 6.7 shows an example of such sequences with a time separation of $\Delta t = 1/2700s$ between the instantaneous snapshots, corresponding to the inverse of the sampling frequency. The instantaneous snapshots are ordered in time from dark to light color.

Before examining the existence and behaviour of coherent structures at the serrated trailing-edge, the structures and events at the straight trailing-edge are explored to establish a basis for comparison. Figure 6.7 shows examples for the development of coherent structures in the interrogation volume over time. A number of clearly identifiable structures are marked for better recognition.

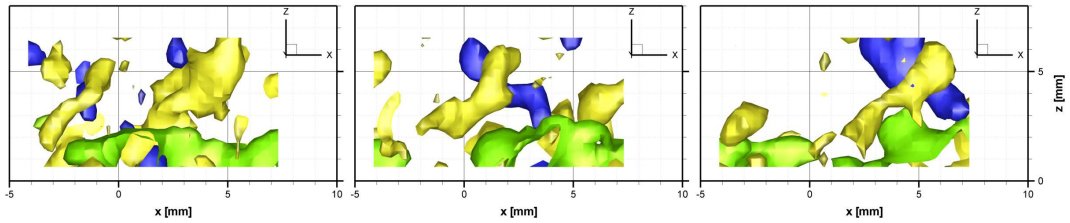

Figure 6.6: Ejection (purple, positive v) caused by hairpin vortex (yellow, $Q = 1 \cdot 10^6 \frac{1}{s^2}$) on low-speed streak (green, $U = 7.5m/s$), $\Delta t = \frac{1}{2700}s$

As mentioned before, within the boundary layer at least two types of vortical structures have to be discriminated: Hairpin and cane vortices. Cane vortices are incomplete, broken or asymmetric hairpins with or without head. The figures indicate that only few complete hairpins are swept towards the trailing-edge with the boundary layer but that the vast amount of structures seem to be of the second type. But the fact that they cannot be identified in the interrogation volume does not mean that they do not exist. First of all, there is a high chance that large canes appearing as counter-rotating pairs, which can be be visualised using the spanwise vorticity component, belong to large hairpin vortices of a scale exceeding the height of the measurement region depicted in figure 6.5. An example of such an incomplete hairpin is present in figure 6.7(a). The height of the interrogation volume nominally spans about 0.8δ, but is limited to about 0.5δ considering the quality of the reconstruction, which is insufficient to capture large structures of scales similar to the boundary layer thickness. Furthermore, hairpins might exist at scales smaller than the ones visible in the reconstruction or closer to the surface, which is supported by the observation that the heads of mature hairpins occasionally appear in the volume. As pointed out by Adrian (2007) cane vortices seem to be rule rather than exception.

Parameters of interest describing these structures are their typical dimensions, inclination with respect to the wall and the growth angle between the wall and the line connecting the heads of the vortices for a sequence of samples. The spanwise scale of hairpin structures, as they become visible in the interrogation volume, is about $2-3mm$ or about $0.2\delta-0.3\delta$ and increases as the structure convects downstream and is stretched. Inclination of the structures with respect to the wall can be observed is in general about 45° or slightly larger (see figure 6.7(a)).

The growth angle, which the structures are subjected to has been observed for a number of individual events. For the straight trailing-edge at zero angle of attack structures remote from the edge seem to experience slightly smaller growth angles than structures closer to the edge, in general about $5°-10°$. The growth angle is of interest, since it gives an indication of the temporal scale that these structures change with. To satisfy the hypothesis of frozen turbulence this scale should be comparable for locations upstream of and in the vicinity of the trailing-edge. It should be noted that it is in many cases impossible to distinguish whether a structure is actually growing or merely convecting and lifted since the lower part of the boundary layer with the aft part of the legs of these structures is not captured. An explanation for the slightly larger angles observed close to the trailing-edge could be the positive mean wall-normal component of the velocity due to the transition from the boundary layer to the wake.

Examples for the case of the serrated trailing-edge with $\Phi = 14°$ are displayed in figures 6.8. As expected from the distribution of Reynolds stresses the region in between individual serration shows higher values of Q and appears to be more populated with structures of relatively long spanwise coherence. In the case of the serrations it is possible to distinguish present structures based on their region of origin.

A relatively small number of fully developed or growing hairpins enters the volume with the boundary layer. In cases where these structures can be identified, they appear to grow at relatively small angles of about 5° similar to those observed for the straight trailing-edge

remote from the edge. As they travel over the edge they start to lose integrity and fall apart. The distance between the legs depends on the age of these structures, but the order seems to be similar to the hairpin vortices arriving with the boundary layer of the straight trailing-edge.

The second category comprises vortices, which originate close to the trailing-edge or enter the volume in between the serrations. In general, members of this category are easier to identify since the strength of the vortex is greater, which is reflected in a higher level of Q. Apart from the difference in strength, structures in this category show a longer spanwise coherence or equivalently a larger distance between the legs ($> 3mm$) and appear in many cases to be more uniform and coherent. Again, a difference can be made between vortices originating at the edge of the serrations and vortices appearing in between the serrations. The mechanism in both cases is believed to be shedding by separation or roll-up of vortices behind blunt parts of the trailing-edge, respectively. The latter will be treated again in section 6.4.2. The growth angle with respect to the extended surface of the airfoil is larger with values of $5° - 15°$. As explained above for the case of the straight trailing-edge the seemingly larger growth angle entails the ambiguity caused by the change in direction of the meanflow during transition to the wake, which could account for a difference of up to $7°$, especially in between the serrations where the curvature of the mean streamlines occurs earlier as will be shown later.

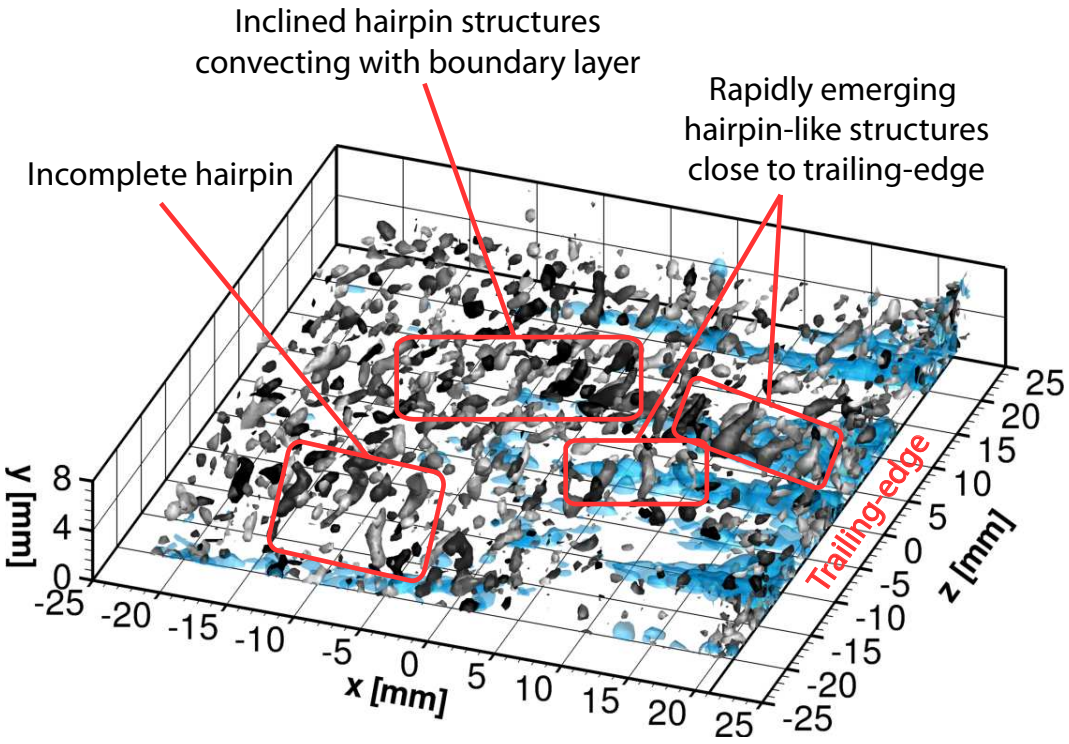

(a) 5 instances from dark to light color, $Q = 2.5 \cdot 10^6 \frac{1}{s^2}$ and low speed streaks $U = 6.5 \frac{m}{s}$ (blue)

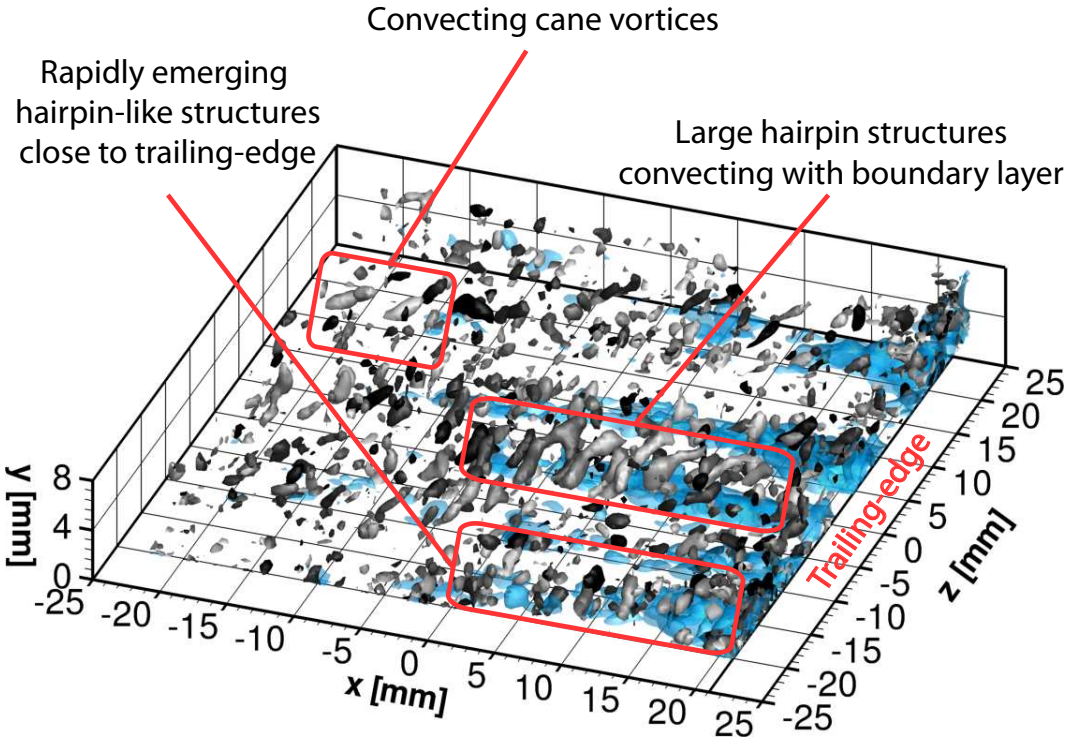

(b) 5 instances from dark to light color, $Q = 2.5 \cdot 10^6 \frac{1}{s^2}$ and low speed streaks $U = 6.5 \frac{m}{s}$ (blue)

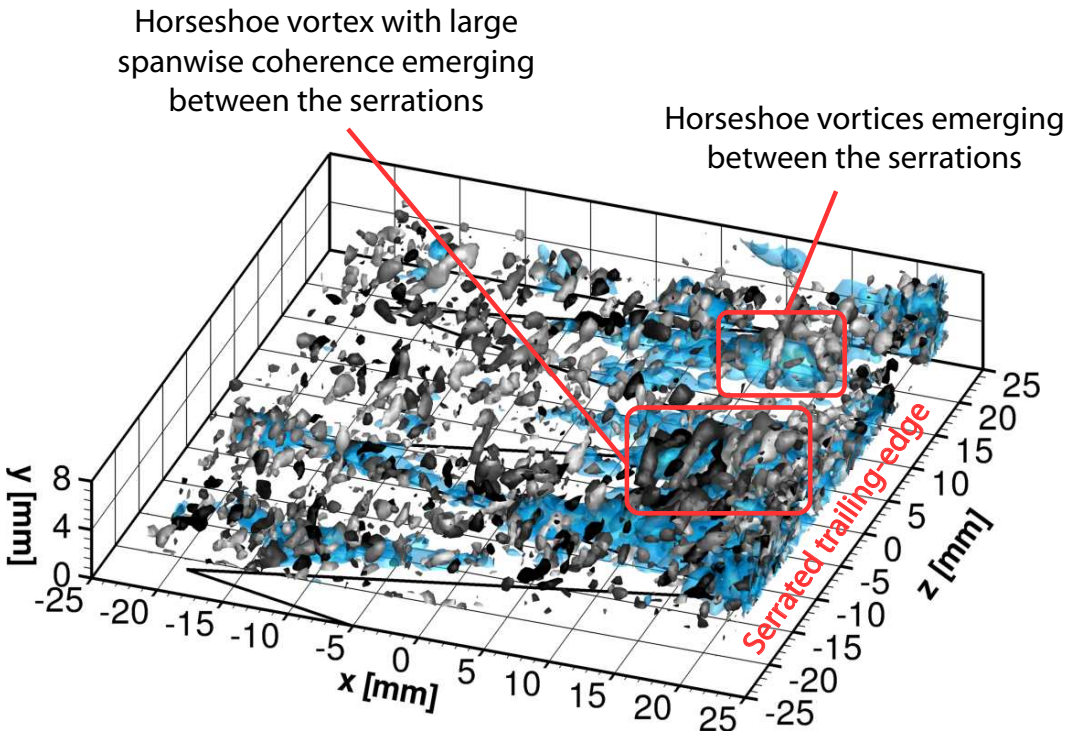

(a) 5 instances from dark to light color, $Q = 2.5 \cdot 10^6 \frac{1}{s^2}$ and low speed streaks $U = 6.5 \frac{m}{s}$ (blue)

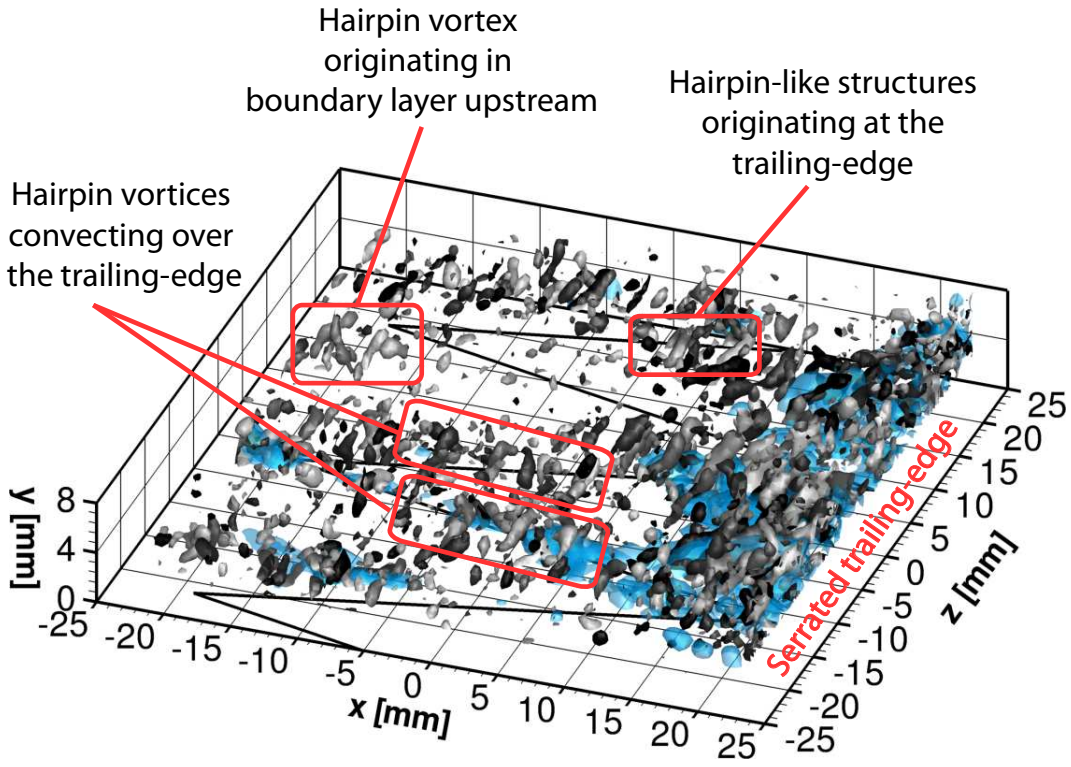

(b) 5 instances from dark to light color, $Q = 2.5 \cdot 10^6 \frac{1}{s^2}$ and low speed streaks $U = 6.5 \frac{m}{s}$ (blue)

Figure 6.8: Development of structures, serrations $\Phi = 14°$, $\Delta t = \frac{1}{2700} s$

6.3.2 Low-speed streaks and spanwise coherence length

Individual zones of low speed fluid can be identified throughout the boundary layer. As pointed out in chapter 2 in the viscous sublayer or, if induced by hairpins, in the regions remote from the wall as explained in chapter 3. In instantaneous images of the velocity field in a streamwise-spanwise plane low speed streaks are not always clearly defined and can bifurcate or overlap.

The spanwise coherence length of the streaks can be determined by means of the correlation coefficient of the velocity fluctuation in streamwise direction u' along a line in spanwise direction. This analysis has been conducted for serrated and straight trailing-edge and different locations in spanwise and streamwise direction. Figure 6.9 depicts the results for the correlation coefficient as a function of shift in spanwise direction. Assuming a repetitive pattern of similar low and high speed streaks in spanwise direction, the correlation coefficient becomes zero for a shift equal to $1/4\lambda_s$, where λ_s is the spanwise spacing between the centres of streaks of identical type.

The statistics in figure 6.9 have been obtained from a statistical data set of 500 independent velocity fields recorded at $100Hz$. For the case of the straight trailing-edge depicted on the right-hand side of the figure, the spanwise spacing is virtually independent of streamwise and wall-normal location and approximately equal to $\lambda_s \approx 4 \cdot 2.5mm \approx 10mm$ which corresponds to about $350\delta_\nu$ based on the viscous wall unit listed in table 6.2. Note that the mean spanwise spacing in literature is reported to be relatively constant at $100\delta_\nu$, which however relates to the sublayer where the low speed streaks are arguably more clearly defined and generated by a different mechanism than in remote parts of the boundary layer as described in section 3.2.

On the serrations of $\Phi = 14°$ the low-speed streaks show the same characteristics as for the straight trailing-edge from the root at $x = -20mm$ to the location $x = 20mm$. From this point on stronger mixing occurs, probably due to the shedding process and earlier transition to the wake. Depending on the height between $x = 0mm$ and $x = 10mm$ the correlation coefficient ceases to drop to zero, indicating zones of high spanwise coherence. The spanwise coherence is directly proportional to the emitted sound power and therefore the large spanwise coherence found for the serrations is expected to have a negative impact.

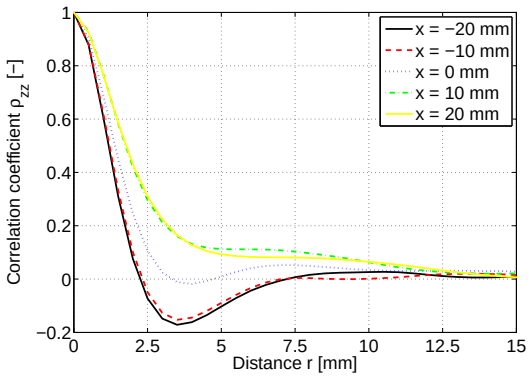

(a) Serrations $\Phi = 14°$, $y = 1.5mm$

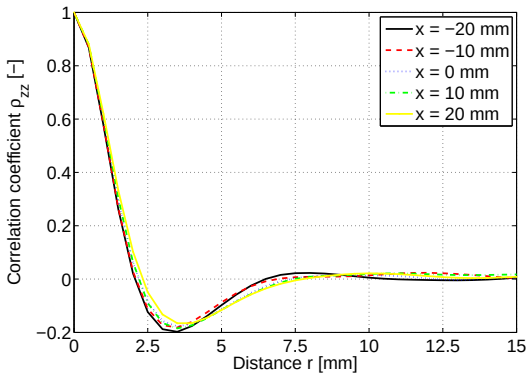

(b) Straight trailing-edge, $y = 1.5mm$

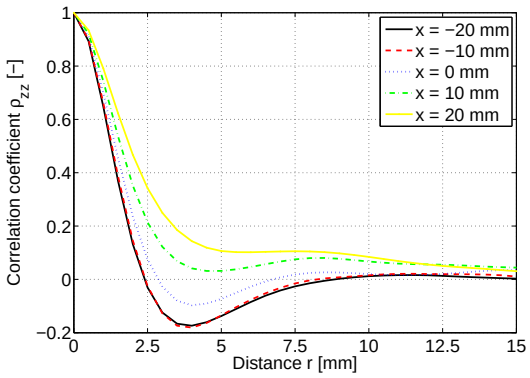

(c) Serrations $\Phi = 14°$, $y = 3.5mm$

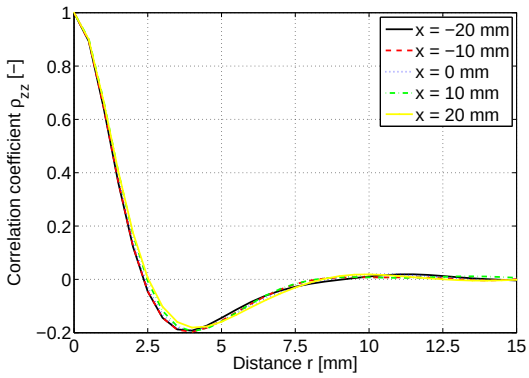

(d) Straight trailing-edge, $y = 3.5mm$

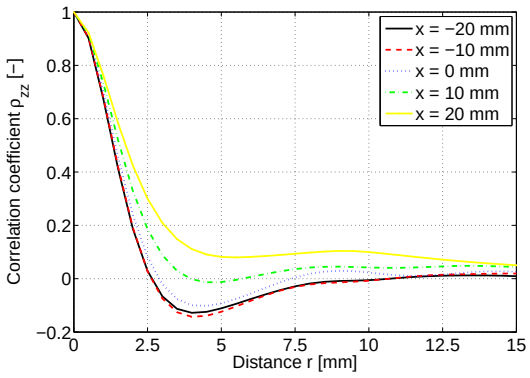

(e) Serrations $\Phi = 14°$, $y = 5.5mm$

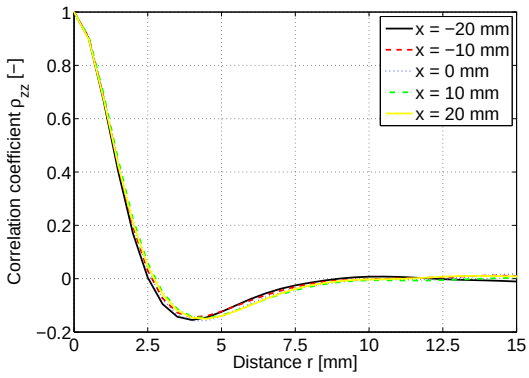

(f) Straight trailing-edge, $y = 5.5mm$

Figure 6.9: Comparison of spanwise coherence length for serrations and straight trailing-edge

6.4 Vortex shedding

This section presents the results for the generation of tonal noise in section 6.4.1 and the related shedding of vortical structures from blunt parts of the trailing edge in section 6.4.2.

6.4.1 Tonal noise

For the tonal noise, which was clearly audible during the experiments, it is attempted to determine the frequency and scaling parameters involved. As described in section 2.1 tonal noise is a result of vortex roll-up and shedding from the blunt part of a trailing-edge with vortices of defined size, convecting at a characteristic velocity. In the present case, the velocity scaling should be proportional to the freestream velocity or U_∞.

Figures 6.10(a) and 6.10(b) show the peak shedding frequencies f on the y-axis, the frequencies corresponding to the local maxima of the tonal noise in figure 6.1, and the serration length and serration angle on the x-axis, respectively. As figure 6.10(a) shows for frequencies of about $\Phi \approx 30°$ the peak frequency attains a maximum and decreases monotonously for greater or smaller angles. For low velocities the maximum variation is about 40%. Peak frequencies generally increase for greater velocities. Figure 6.10(b) shows a decrease in peak shedding frequency for greater serration length, and therefore greater trailing-edge bluntness, and the same dependency on the velocity.

Plot 6.12(a) shows additionally the peak shedding frequencies obtained from the stereoscopic PIV measurements described in section 5.5. The velocity fluctuation u' at a defined location was sampled and consecutively the spectrum was estimated using Welch's algorithm. Spectra obtained for serration angles of 14°, 32° and 45° at $U_\infty = 10m/s$ are shown in figure 6.11. As for the noise measurements the frequencies corresponding to the maximum values of the spectra are termed peak shedding frequencies. Note that for the serrations $\Phi = 14°$ in figure 6.11(a) two peaks are visible which are located relatively close to each other. At different locations in the flow field one or the other of these modes is dominating. The shedding frequencies determined through PIV follow the trend of the noise measurements to decrease for angles different from 30°.

A natural assumption for the length scale is the serration length H, which scales linearly with the amplitude $h = \frac{1}{2}H$ as well as with the trailing-edge bluntness $t = 2 \cdot \tan 7° H$ at the root of the serrations. Plots of the non-dimensional peak shedding frequencies in dependence of serration angle Φ and serration length H are depicted in figure 6.12. Here, the frequencies are normalised with fH/U_∞.

From both plots in figure 6.12 it becomes apparent that the velocity scaling parameter U_∞ can be used to collapse the data obtained for different velocities. The serration length H and therefore the serration amplitude amplitude h and the trailing-edge bluntness t do not appear to be the appropriate scaling parameters since the the non-dimensional frequency shows a dependence on the serration angle Φ as shown in figure 6.12(a). The peak frequencies of noise

measurements and PIV measurements appear to be in relatively good agreement. Deviations in the data might be attributed to the different conditions regarding wind tunnel facility, model, Reynolds number and most importantly the difference in serration length H, which is $H = 40mm$ for the models used during the PIV measurements. If the serration length or equivalently the maximum trailing-edge bluntness is not appropriate length scale the results cannot be expected to collapse.

Figure 6.12(b) suggest that for constant Φ the peak shedding frequency does not scale linearly with the serration length H.

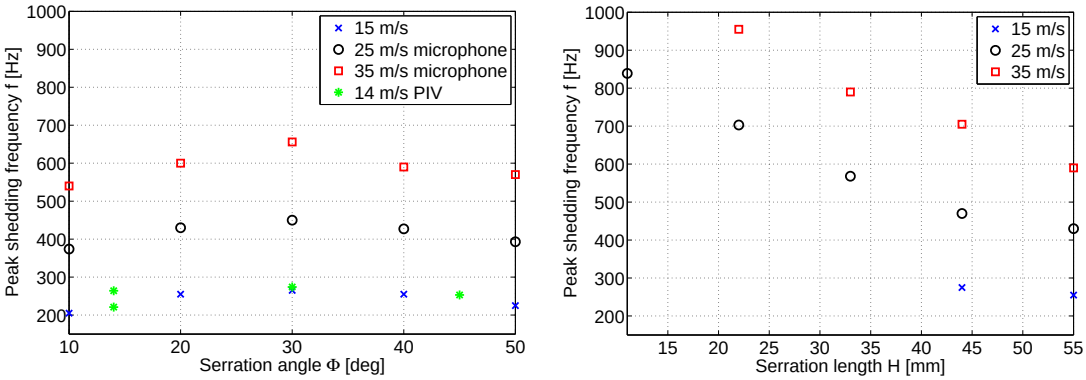

(a) Constant h (b) Constant $\Phi = 30°$

Figure 6.10: Tonal peak frequencies for different serrations and velocities

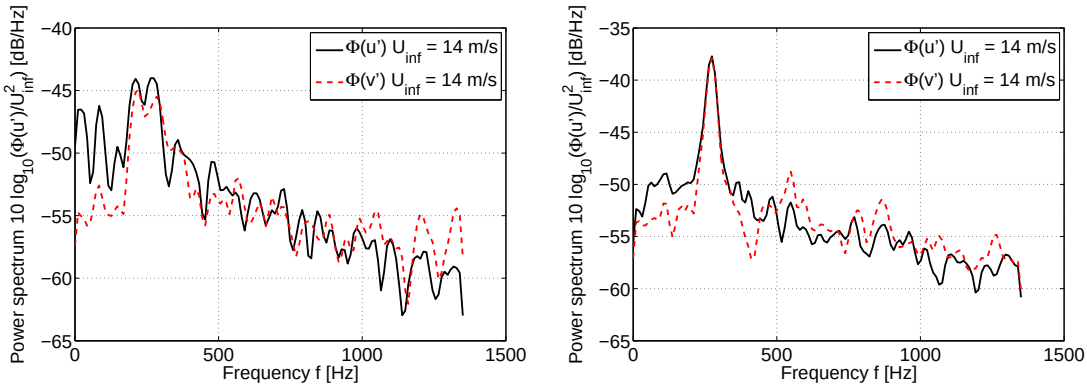

(a) $\Phi = 14°$ (b) $\Phi = 30°$

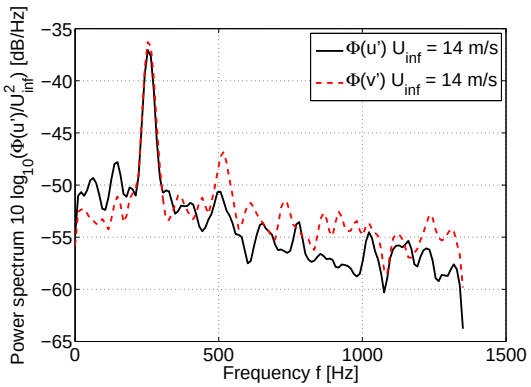

(c) $\Phi = 45°$

Figure 6.11: Power spectral density of u' and v'

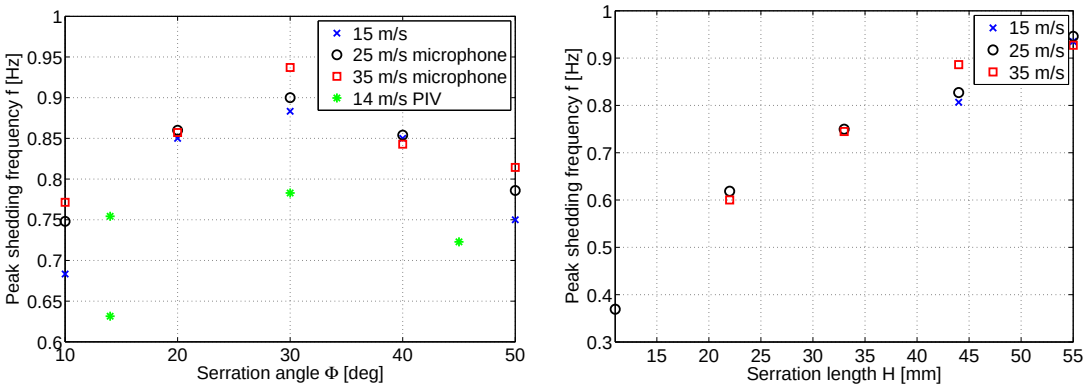

(a) Constant h

(b) Constant $\Phi = 30°$

Figure 6.12: Normalised tonal peak frequencies for different serrations and velocities

6.4.2 Horseshoe vortices between serrations

As described previously, apart from the relatively small coherent regions of Q, termed hairpin vortices, larger structures with considerable spanwise extent originating in between the serrations can be identified in sequences of time-resolved data. On one hand, these large structures have a shape similar to the hairpins in the boundary layer, showing a head and the indications of legs. On the other hand, the spanwise extent and the intensity of these vortices makes them clearly distinguishable from the smaller structures and therefore this kind of structure is termed horseshoe vortex in this work. This term is in line with the nomenclature of Jones and Sandberg (2010) for large spanwise vortical structures originating in the space between serrations.

Figure 6.13 shows three separate sequences of vortices involved in the shedding process, which in fact originate or roll up in the space between the serrations and enter the measurement volume at a later stage. Individual time instances within each sequence are indicated with different shades from dark to light and are recorded with a separation in time of $1/2700s$. The time separation between two independent sequences is $10 \cdot 1/2700s$, meaning that for this example vortex shedding occurs with a frequency of approximately $270Hz$.

As can be seen in figure 6.12, this is in agreement with the peak shedding frequency found by statistical analysis of the stereoscopic PIV data and the tonal peak found for noise measurements in a different facility and for a different model. These indications point towards the conclusion that these large structures with a long spanwise coherence are related to the dominating mode of the vortex shedding process.

An alternative mode to the occurrence of one horseshoe vortex of large spanwise coherence in the center of the space between the serrations is the (almost) simultaneous appearance of two smaller vortices at opposite edges in between two serrations as can be seen in figures 6.8(b). These alternating shedding modes might account for the width of the tonal peak as shown in figure 6.1.

It should be noted that the horseshoe vortices grow as they convect downstream between the serrations and that their spanwise extent at the location of the tips is close to the wavelength of the serrations. This might be an analogue to the large structures with spanwise coherence equal to the serration wavelength which were recently observed by Jones and Sandberg (2010) in a DNS for the case of an airfoil with serrated flat plate extension at an angle of attack.

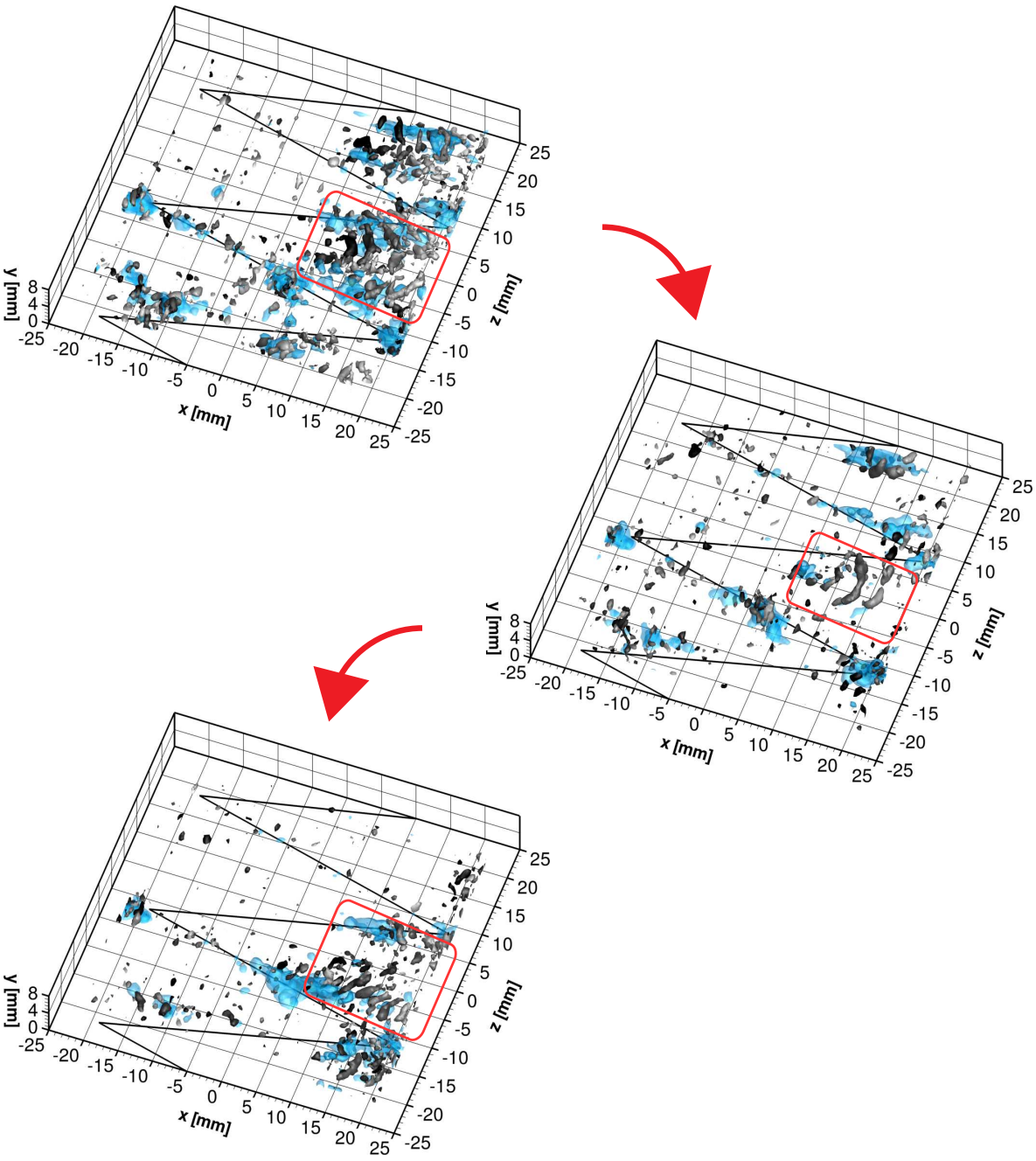

Figure 6.13: Three sequences showing vortex shedding at about $270Hz$ between the serrations. Low velocity $u = 5m/s$ (blue), $Q = 5 \cdot 10^6 \frac{1}{s^2}$ (instances from dark to light, $2700Hz$).

6.5 Surface pressure fluctuations

Additionally, the results of surface microphone measurements will be used to obtain the frequency pressure spectrum in section 6.5.1 and derive a characteristic convection velocity of the surface pressure field.

6.5.1 Surface pressure spectrum and coherence length

The complete wall pressure spectrum depends on three independent parameters, namely the wavenumber in streamwise k_1, the wavenumber in spanwise direction k_3, and the frequency ω as stated in Bull (1996), which is denoted by $\Phi_p(k_1, k_3, \omega)$. Since surface microphones can only be positioned at a number of discrete locations, it is impossible to record the complete pressure spectrum with a finite number of microphones.

Data used in this section has been acquired with the experimental set-up described in section 5.7 recording $200,000$ samples at $40kHz$ per run. From the time-varying data recorded by a single microphone the frequency dependent part of the pressure spectrum with k_1 and k_3 identically zero can be derived by computing the power spectrum. The spectra has been computed using Welch's method described in section 4.1.3. The cross-correlation values, or correlation coefficients, for a time separation of $\tau = 0s$ between multiple microphones aligned in one direction gives an indication of the wavenumber dependence.

Figure 6.14 shows the frequency spectra on the left-hand side and correlation coefficients on the right-hand side for the straight trailing-edge of the microphones arranged in spanwise and streamwise direction as described in section 4.1.3, respectively. Figure 6.14(a) shows the power spectra of the microphones in spanwise arrangement. The absence of individual, paramount peaks indicates that the frequency pressure spectrum is of broadband character. For frequencies exceeding $8kHz$ the data shows differences, which might be attributed to the different responses of the microphones at theses frequencies as shown in figure 5.14(b), although this should partially be accounted for during calibration. Furthermore, microphone 3 shows small negative deviations over the whole range of frequencies, which might be a result of a change in amplifier gain between calibration and measurement. Apart from the above mentioned deviations, the spectra seem to coincide fairly well and are uniform in spanwise direction.

Figure 6.14(b) shows the auto-correlation of the pressure signal of microphone 4 and the cross-correlations with the signals of microphones 1,2 and 3. It should be noted that the correlation coefficient for a time-shift of $\tau = 0s$ is virtually zero, indicating uncorrelated signals, for microphones 1 and 2, while microphone 3 shows a slight anti-correlation of about $\rho \approx -0.1$. It can be concluded that dominant coherent structures with influence on the wall pressure field, if existent, should have typical length scales smaller than the distance between two adjacent microphones $d \approx 7.5mm$.

Figure 6.14(c) shows the power spectra obtained from the microphones in streamwise arrange-

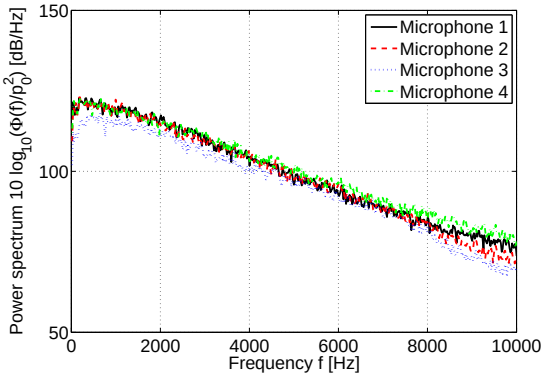

(a) Straight trailing-edge, power spectra of microphones in spanwise arrangement

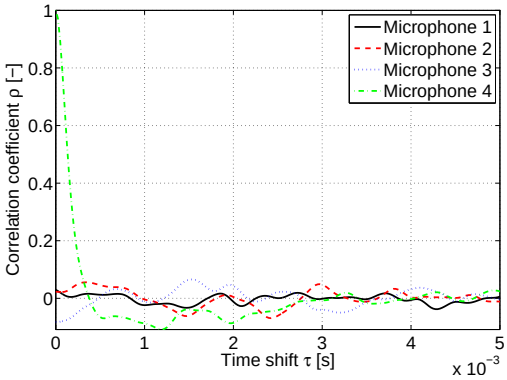

(b) Straight trailing-edge, cross-correlation with microphone 4 in spanwise direction

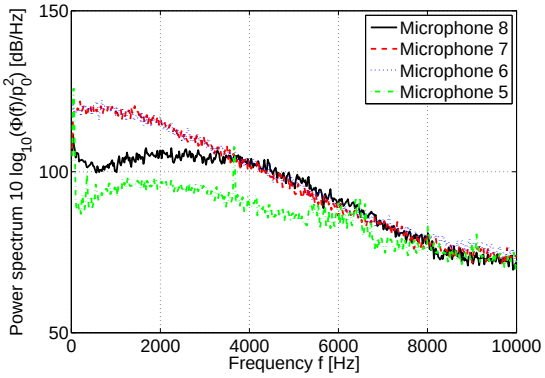

(c) Straight trailing-edge, power spectra of microphones in streamwise arrangement

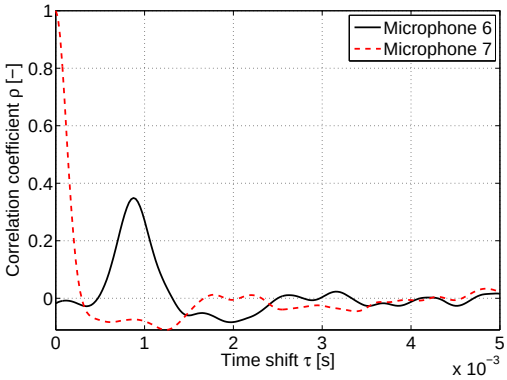

(d) Straight trailing-edge, cross-correlation with microphone 7 in streamwise direction

Figure 6.14: Results of surface microphone measurements, straight TE

ment. Since there is no particular reason for the pressure spectra to show large unsystematic variations, it can be concluded that microphones 5 and 8 did not work during the measurement. A reason might be a loose connection or damage caused by the clay applied to smooth the surface near the microphone cavities. The level seems to be slightly lower compared to figure 6.14(a), which might be attributed to a slight difference in the operating conditions. For the working microphones the shape of the spectra is of broadband character.

Due to the malfunction of the two microphones, the cross-correlation in streamwise direction could only be performed between microphones 6 and 7 and is shown in figure 6.14(d). The time separation between the peaks is measured to be $\Delta\tau = 0.875ms$ and a correlation coefficient of about $\rho \approx 0.4$ was obtained. Under the hypothesis of frozen turbulence, a correlation coefficient close to unity should be expected for small distances between the microphones. It is not entirely clear in how far this low correlation coefficient must be attributed to the supposedly low signal-to-noise ratio of the system, since this issue was not addressed explicitly.

Repeatability was checked by performing the experiment multiple times, yielding identical results for the time separation of the peaks. Assuming a distance of about $d \approx 7.5mm$ between the centres of the microphone cavities, the characteristic propagation velocity of the pressure field can be estimated as shown in equation 6.1 corresponding to about $U_c = 0.6U_\infty$, i. e. approximately 60% of the freestream velocity..

$$U_c = \frac{d}{\Delta\tau} \approx 8.6m/s \tag{6.1}$$

The time separation τ where the correlation coefficient of the auto-correlation for the signal of microphone 7 becomes negative in figure 6.14(d) is $\tau = 0.275ms$. For structures mainly responsible for the surface pressure fluctuations this should correspond to approximately half of the time needed to pass the microphone cavity. Assuming these structures travel at the characteristic speed U_c the order of the characteristic dimension of such a structure can be estimated by the expression in equation 6.2. Repeatability was again checked by multiple experiments.

$$L_{structure} \approx \frac{2\tau}{U_c} \approx 4.6mm \tag{6.2}$$

Typically, the size of hairpins is distributed over a range of scales, but hairpins found in the logarithmic region usually have extensions on the order of the boundary layer thickness or smaller. Therefore, from the point of view of coherent events it could be those particular structures, namely hairpins and canes in all their variations and shapes, that are mainly responsible for the convective part of the pressure spectrum on the surface. Furthermore, this result indicates that surface pressure fluctuations are not significantly correlated to low-speed streaks or regions of low-speed fluid in the outer region of the boundary layer since these structures have typical extensions on the order of or exceeding the boundary layer thickness δ, which is in this case approximately $10mm$ as listed in table 6.1.

Results for the series of serrated trailing-edge models obtained through a similar procedure as described above are shown in figure 6.15. On the left-hand side the spectra for all three models are plotted with the microphones arranged as shown in figure 5.15(b) while on the right-hand side the corresponding cross-correlations are shown. Microphone 3 shows again slightly lower levels which, as reported for the straight trailing-edge, might be connected to a change in amplifier gain between calibration and experiment.

Comparing the spectra to the results obtained for the straight trailing-edge in figure 6.14 the most prominent difference is the peak in the low frequency band which becomes more pronounced for larger serration angles. This dominant fluctuation frequency in the pressure spectra can be linked to the shedding process by comparing the frequencies to the characteristics of the audible tonal noise identified in figure 6.10(a). For the serration angle of $\Phi = 14°$ in figure 6.15(a) the peak frequency is about $235Hz$, for $\Phi = 32°$ in figure 6.15(c) it is $275Hz$

and for $\Phi = 45°$ in figure 6.15(e) it is $255Hz$. These frequencies approximately match the results of the stereoscopic PIV experiment and the frequencies of the tonal noise and shedding. Furthermore, comparing the spectra obtained for the different serration designs, a systematic shift towards higher levels for increasing bluntness becomes apparent, especially for higher frequencies. This might motivate the conclusion that the vortex shedding changes the wall pressure field more than simply superimposing fluctuations at the shedding frequency.

This leads to the conclusion that bluntness of the trailing-edge has an influence on the pressure spectrum upstream of the trailing-edge eliminating the validity of the important theoretical assumption of frozen turbulence near the blunt trailing-edge, unless this modification is merely a superposition. This reasoning is underlined by the cross-correlation plots depicted on the right-hand side of figure 6.15. The relatively high peaks show that a correlation of the pressure exists even in spanwise direction. Large structures, such as vortices produced through the roll-up process during vortex shedding as a consequence of instabilities in the boundary layer, provide a reasonable explanation and will be investigated in section 6.4.2. For larger serration angles this correlation becomes more pronounced and also the peak in the auto-correlation show longer coherence in time implying the existence of larger structures.

6.5.2 Pressure-velocity cross-correlation

After having examined the occurrence and character of coherent structures in the previous sections and with the knowledge about the wall pressure at a number of discrete points in section 6.5.1, it is of interest to investigate correlations between flow field variables connected to these structures and the pressure field. A simple method yielding first indications is to correlate the measured velocity at the locations of microphones and at a certain height to the measured pressure field. For this purpose, prior to sampling the time resolution of the velocity field originally recorded at $2.7kHz$ is increased using the time super-sampling procedure of Scarano and Moore (2010) by a factor of 5, yielding a frequency of $13.5kHz$. On the other hand, the pressure time-series acquired at $40kHz$ with the surface microphones is down-sampled to the same frequency. Since the frequency response of the microphones declines at these frequencies as shown in figure 5.14(b) information in the signal is conserved. In an irrotational field one would expect to find high pressures at locations of low velocity in accordance with Bernoulli, which should yield a clear correlation between the streamwise velocity fluctuation u' and the pressure fluctuations p' measured by the microphone. However, this assumption does not apply in the viscous boundary layer.

Figures 6.16 and 6.17 show the cross-correlation coefficients for the straight trailing-edge, as shown in equation 4.6, and for all three velocity components at the locations of the microphones and $y = 2mm \approx 0.2\delta$, with the wall pressure p' as a function of the time shift. It should be noted that microphone 1 in figure 6.16(a) did not deliver useful data. The correlation coefficients of the signals is in general very low, showing peaks at about $\rho \approx 0.2$, which was to be expected since the flow is not irrotational flow. A marking feature in figures 6.16(d), 6.17(a), 6.17(b), and 6.17(c) is the relatively high correlation of the wall-normal v' component at a time-shift of approximately $\tau = 0s$. This might point to a correlation between spanwise oriented vortices, such as the heads of hairpin vortices, and the wall pressure fluctuations.

The correlation coefficients for the serrated trailing-edge $\Phi = 14°$ are plotted in figure 6.18 and show significant differences compared to the straight trailing-edge. As shown in figure 5.15(b) the microphones are arranged along the edge of one serration with microphone 4 being located closest to the root and conversely microphone 1 closest to the tip of the serration.

Figure 6.18(a) shows a considerably higher peak value for the correlation coefficient of about 0.5 at $\tau = 0s$ for microphone 1, which decreases in the direction of the root to the low values seen for the straight trailing-edge as shown by figures 6.18(b), 6.18(c) and 6.18(d). Also in this case the highest peaks occur for the correlation with the wall-normal velocity component v', indicating the dominance of spanwise vortical structures on the local wall pressure field.

Focussing at the correlation of p' and v' in figure 6.18(a), one should note that the time separation between two individual peaks is about $4ms$ which corresponds to a frequency of $250Hz$. This frequency is contained in the frequency band identified as shedding frequencies. It can be concluded that the shedding process has a large influence on the low frequency part of the pressure and velocity field upstream of the trailing-edge.

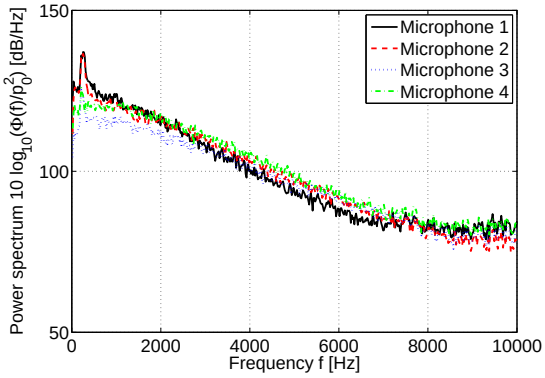

(a) Serrations $\Phi = 14°$, power spectra

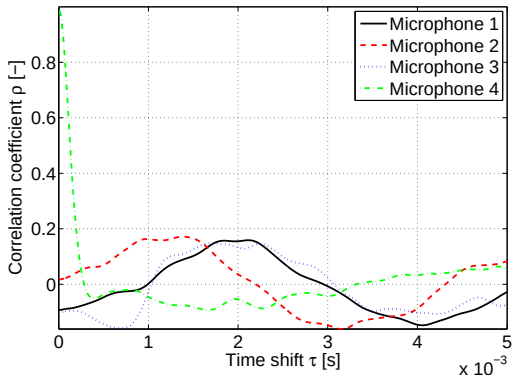

(b) Serrations $\Phi = 14°$, cross-correlation with microphone 4

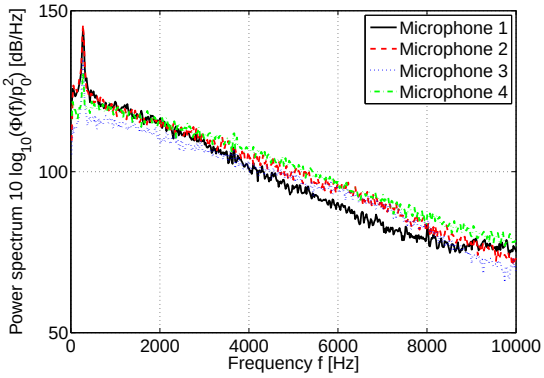

(c) Serrations $\Phi = 32°$, power spectra

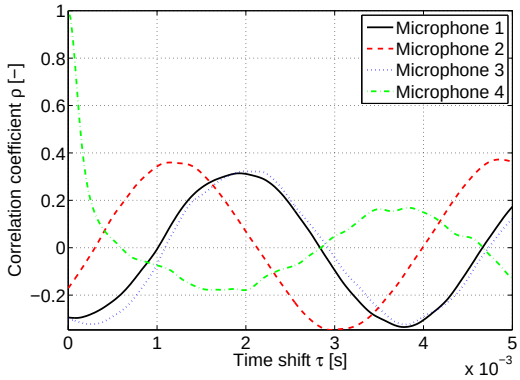

(d) Serrations $\Phi = 32°$, cross-correlation with microphone 4

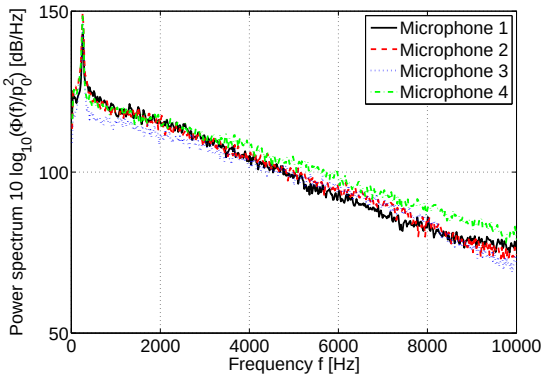

(e) Serrations $\Phi = 45°$, power spectra

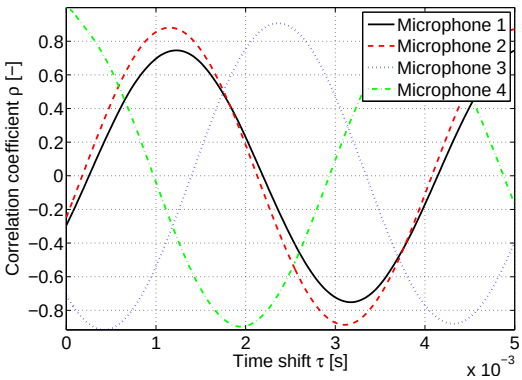

(f) Serrations $\Phi = 45°$, cross-correlation with microphone 4

Figure 6.15: Results of surface microphone measurements for serrations

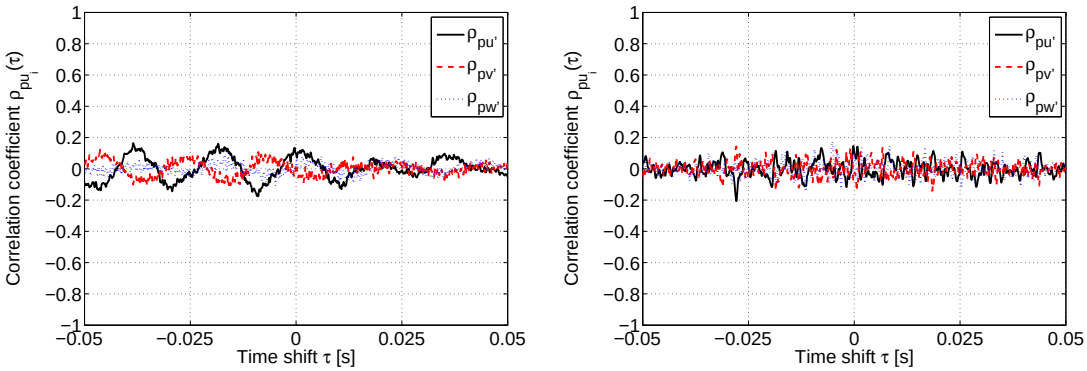

(a) Microphone 1

(b) Microphone 2

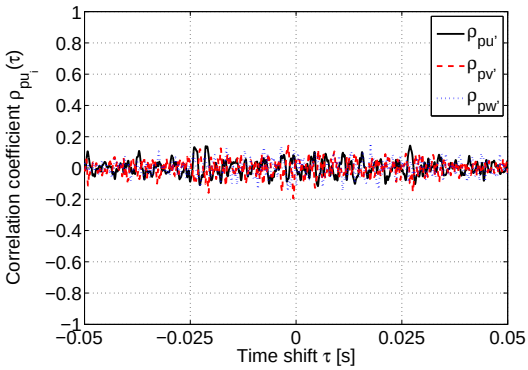

(c) Microphone 3

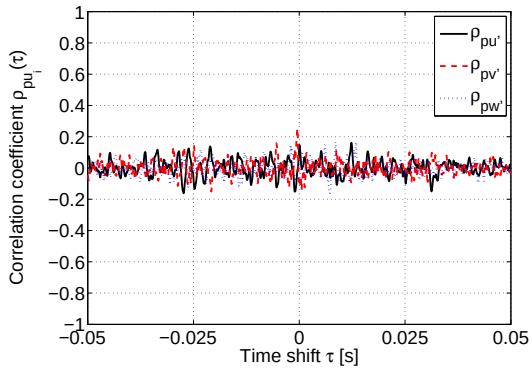

(d) Microphone 4

Figure 6.16: Pressure fluctuation cross-correlated with velocity component at $y = 2mm$, straight TE spanwise

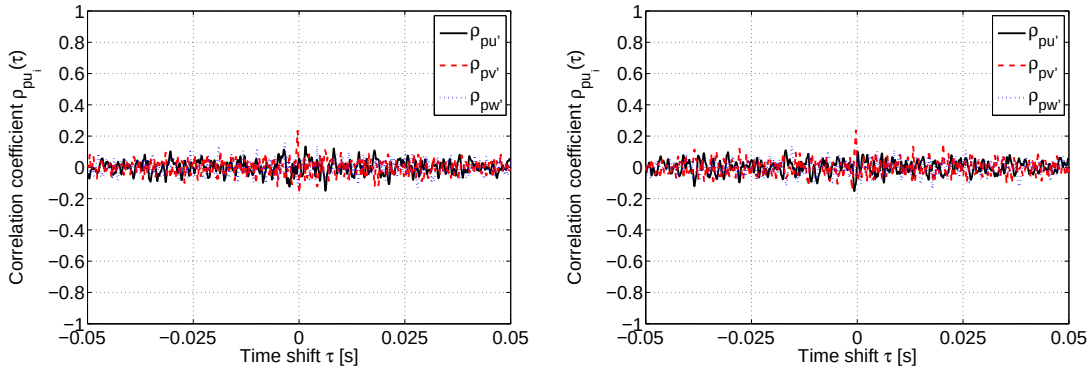

(a) Microphone 5

(b) Microphone 6

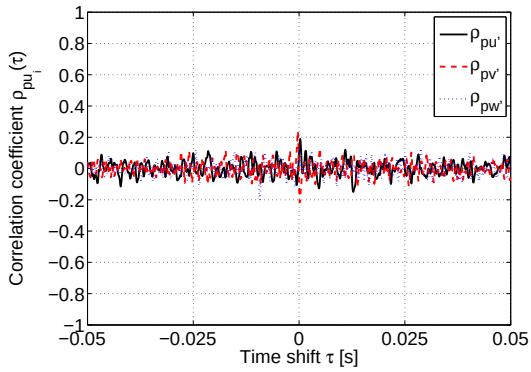

(c) Microphone 7

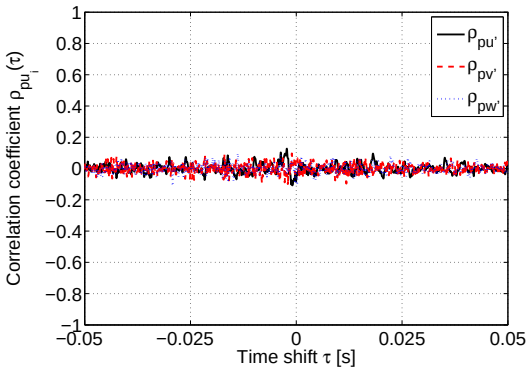

(d) Microphone 8

Figure 6.17: Pressure fluctuation cross-correlated with velocity component at $y = 2mm$, straight TE streamwise

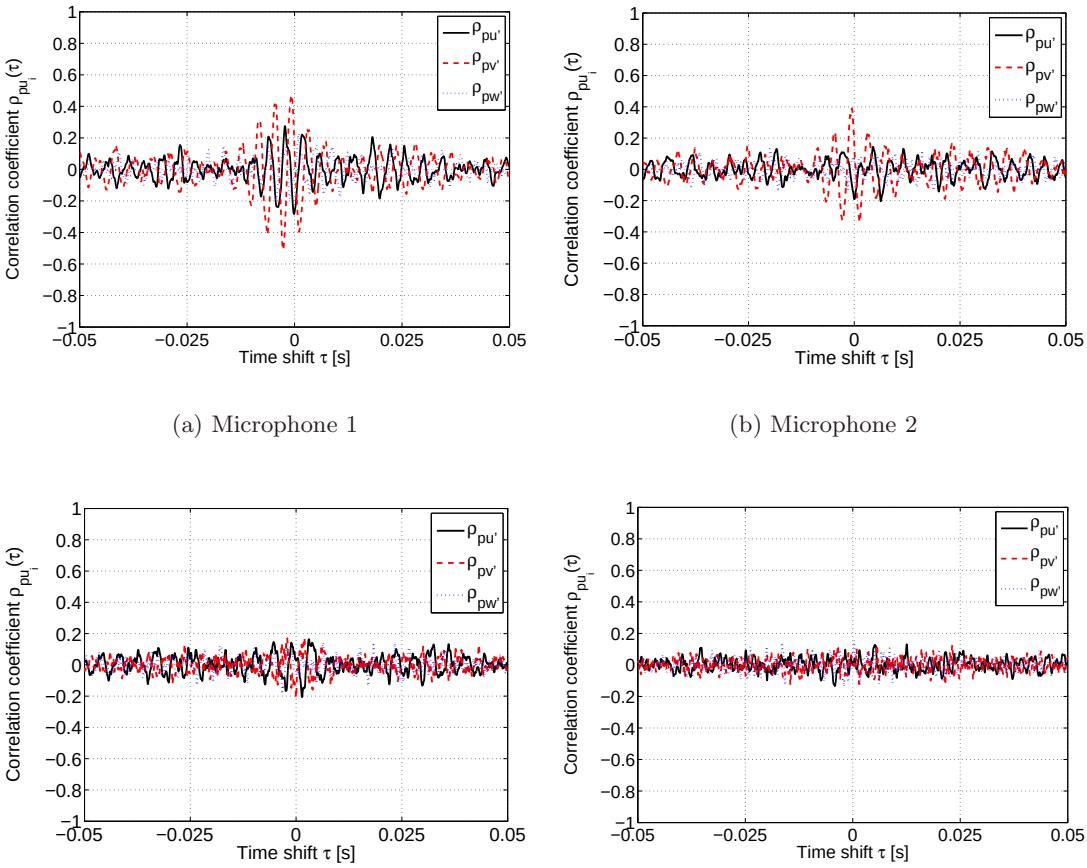

(a) Microphone 1

(b) Microphone 2

(c) Microphone 3

(d) Microphone 4

Figure 6.18: Pressure fluctuation cross-correlated with velocity component at $y = 2mm$, serrated TE

6.6 Statistical description of flow

This section gives a statistical description of the mean flow including the mean velocity field in section 6.6.1 below and the Reynolds stresses in section 6.6.2. Data used in this section has been recorded using the tomographic PIV set-up described in section 5.6. Statistics of the velocity field in this section have been obtained by averaging 500 statistically independent vector fields recorded at a sampling rate of $100Hz$.

6.6.1 Mean velocity field

The mean flow field over the serrations is compared to the flow field over the straight trailing-edge. Slices of the average velocity field are plotted for all three velocity components in figure 6.19.

Figures 6.19(a) and 6.19(b) show the streamwise component of the velocity for the serrated trailing-edge and for the straight trailing-edge, respectively. It should be noted that the velocity contours close to the wall are substantially different, in the sense that they are uniform in spanwise direction for the straight trailing-edge and symmetric about the root or tip locations for the serrated trailing-edge. In the space in between the serrations the fluid shows a slightly higher velocity compared to the same streamwise location on the surface of the serrations. On top of the serrations the flow experiences opposing forces and decelerates due to the presence of the adverse pressure gradient and viscous forces related to the no-slip condition. As the flow travels over the edge to enter the free space in between the serrations the no-slip condition disappears, delaying the deceleration of the flow towards the wake. With increasing distance from the wall the difference diminishes and the velocity field for the serrated trailing-edge becomes more uniform in spanwise direction, which is presumably a manifestation of the decreasing influence of the viscous forces connected to the wall boundary condition away from the wall.

The wall-normal velocity component is depicted in figures 6.19(c) and 6.19(d), respectively. This component is close to zero for close to the surface of the airfoil, as prescribed by the boundary condition for a non-permeable wall. As the flow reaches the free space in between the serration it experiences a relatively strong downwash, which can be explained with the discontinuation of this boundary condition. The flow plunges into the free space in between the serrations and further downstream recovers to adapt to the flow conditions and direction in the wake, i. e. parallel to the freestream. For this reason and since the measurement volume is inclined with respect to the freestream, the wall-normal velocity components becomes positive further downstream. The adaptation occurs earlier in the space between the serrations than at the locations of the tips. With increasing height the above mentioned features are still visible, but weaker than for locations closer to the wall, and the condition of the straight trailing-edge is approached.

Figures 6.19(e) and 6.19(f) show the spanwise component of the velocity at $y = 1.5mm$. It should be noted that even the the results for the straight trailing-edge in figure 6.19(f)

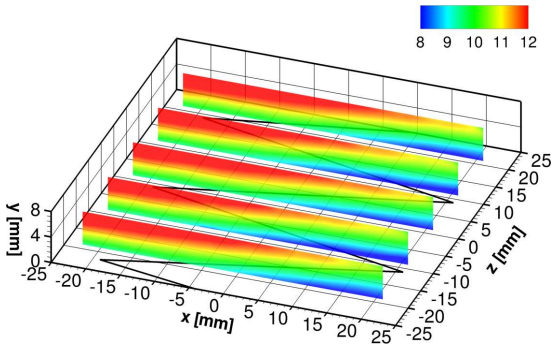

(a) $\Phi = 14°$, mean velocity in x-direction (m/s)

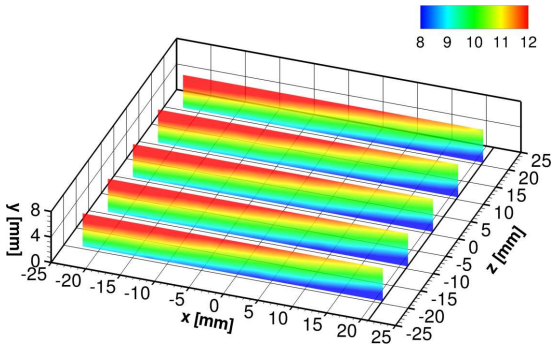

(b) Straight TE, mean velocity in x-direction (m/s)

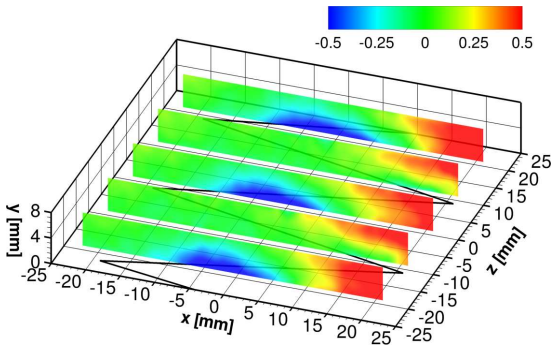

(c) $\Phi = 14°$, mean velocity in y-direction (m/s)

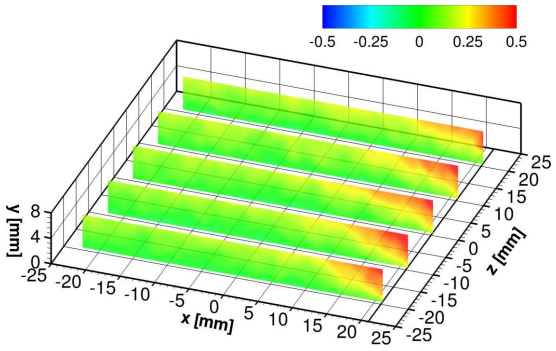

(d) Straight TE, mean velocity in y-direction (m/s)

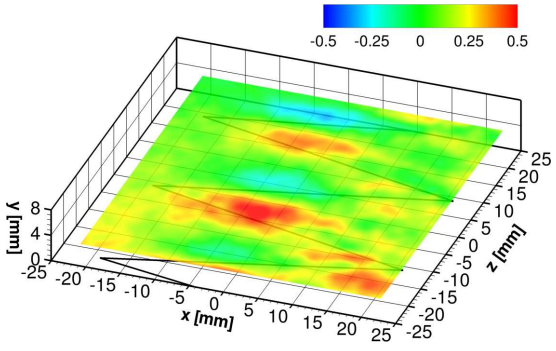

(e) $\Phi = 14°$, mean velocity in z-direction (m/s), $y = 15mm$

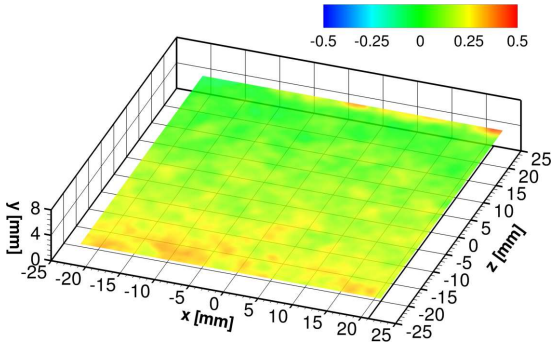

(f) Straight TE, mean velocity in z-direction (m/s), $y = 15mm$

Figure 6.19: Comparison of meanflow velocity for serrated and straight trailing-edge

show a small, non-uniform positive component which was not expected given the symmetry of the problem. Considering a maximum spanwise velocity of $w \approx 0.4m/s$ and a minimum streamwise velocity component of $u \approx 8m/s$ this deviation accounts at maximum for an

angle of 3° with respect to the freestream direction. This spanwise velocity component is also visible at the locations remote from the surface and therefore presumably not related to the geometry of the surface, but to a slight misalignment of the model or an influence of the shear layers developing at the tunnel exit.

Figures 6.19(e) and 6.19(f) show the general tendency of a small positive spanwise flow component. In the case of the serrated trailing-edge, positive and negative spanwise velocity components at opposite edges of the serrations can be identified, which indicates a curvature of the streamlines towards the serration edges. This behaviour might be attributed to the absence of the no-slip condition and therefore higher mean flow velocity over the free space in between the serrations as described before. This in turn might lead to a pressure difference with a favourable pressure gradient pointing in the outward normal direction with respect to the edges of the serrations, causing a small local curvature.

6.6.2 Reynolds stresses

The Reynolds stress tensor is often considered in aero-acoustical applications since it has been shown by Lighthill (1952) and others to be connected to the generation of sound. It enters the source terms of acoustic analogies through the Lighthill stress tensor and the source itself is of quadrupole nature. In contrast, the dominant noise sources in the edge diffraction problem are of dipole nature as outlined in chapter 2 motivating the difference by a factor of M_∞^2 in source strength. Therefore, quadrupole sources such as the Reynolds stress terms regarded as direct noise sources are of minor importance for low Mach number flows considered here. However, Reynolds stresses can also give indications with respect to the presence of coherent vortical structures and turbulence production. Figures 6.20 shows the diagonal components of the Reynolds stress tensor, computed by means of equation 6.3 from the tomographic recording described in section 5.6 for the serrated trailing-edge $\Phi = 14°$.

$$R_{xy} = \rho_0 \frac{1}{N} \sum_{1}^{N} u_i' v_i' \tag{6.3}$$

It should be noted that the field of view shows exclusively the boundary layer region for the straight trailing-edge where the Reynolds stresses are slightly lower compared to the near-wake region where the turbulent boundary layers from both sides of the airfoil interact. A different situation is encountered for the case of the serrated trailing-edge: Higher values of various component of the Reynolds stress tensor indicate an increased activity between the serrations as expected which is partially due to the shedding process from the blunt parts of the edge. Outliers in the data such as in figure 6.20(a) are caused by relatively strong reflections from the shiny surface of a microphone.

Figure 6.20 shows that the diagonal components of the stress tensor attain their highest values in the last third of the cavity between the serrations and in the vicinity of the edge, i. e. at the discontinuity of the wall boundary condition. Especially figure 6.20(a), showing the

streamwise component, indicates a high activity in this region which might be connected to the roll-up of vortices. Figure 6.20(b) shows the wall-normal component of the Reynolds stresses to increase in downstream direction in the free space between the serrations. Furthermore, the activity is uniform over the width of the free space except for the regions close to the serration edges. This distribution indicates the presence of vortical structures over the whole width of the free space. Figure 6.20(c) shows the spanwise component of the Reynolds stresses and indicates the highest activity around the edges in the last third of the serrations. This might indicate the existence of wall-normal vortical structures.

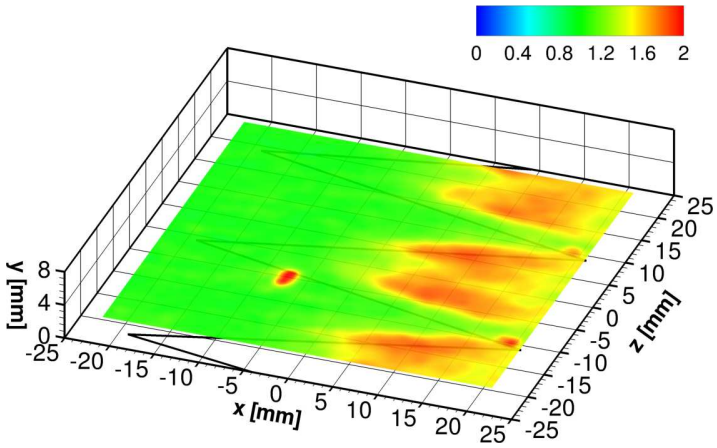

(a) $\Phi = 14°$, RMS of mean velocity in x-direction (m/s), $y = 15mm$

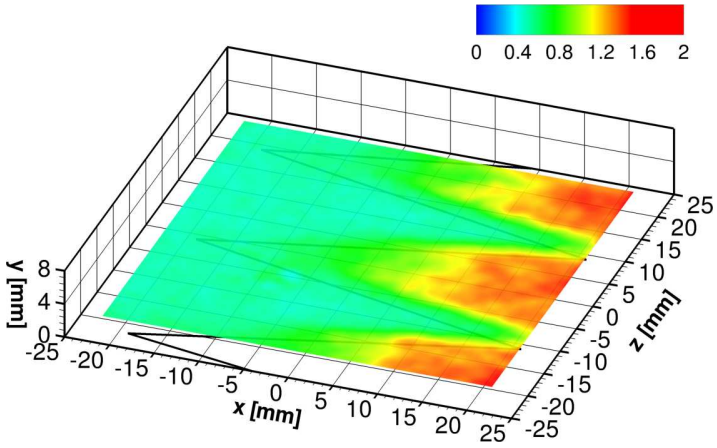

(b) $\Phi = 14°$, RMS of mean velocity in y-direction (m/s), $y = 15mm$

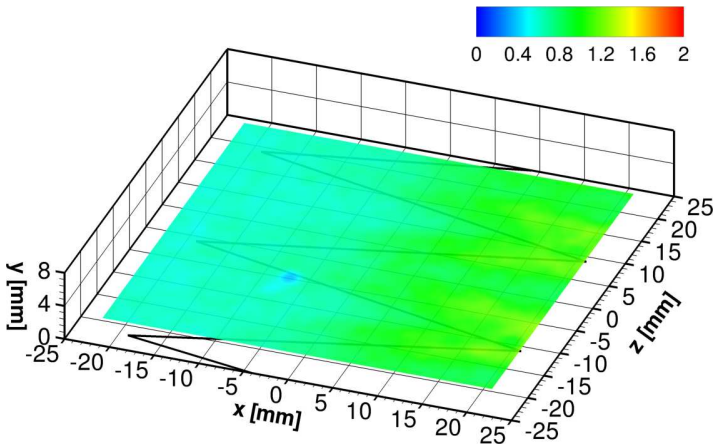

(c) $\Phi = 14°$, RMS of mean velocity in z-direction (m/s), $y = 15mm$

Figure 6.20: RMS of meanflow velocity for serrated trailing-edge

Chapter 7

Conclusion

On one hand, acoustic measurements have indicated that the noise spectra for sawtooth serrations with at the partially blunt trailing-edge of a NACA 0012 airfoil show a reduction in noise level for frequencies exceeding $1kHz$, which is in accordance with Howe's theory of trailing-edge noise. On the other hand, tonal narrowband noise associated to the shedding of vortices from the blunt parts of the trailing-edge eliminates these noise reduction benefits. A decrease in total sound pressure level is not observed. On the basis of this particular case the use of serrations cut into the profile of the airfoil, where parts of the trailing-edge become blunt, cannot be recommended.

For the visualization of vortical structures in the flow the Q-criterion has been used and applied to the velocity data, which was obtained by tomographic PIV. Coherent structures, which are observed in the adverse pressure gradient boundary layer relatively close to the trailing-edge, show a relatively fast growth rate compared to previous results. Most structures with origin in the boundary layer upstream of the trailing-edge appear in the form of canes which are incomplete or asymmetric hairpin structures, but also individual vortices, so-called canes, inclined with respect to the wall at about 45° are observed. Complete hairpin structures can always be associated with a region of relatively low velocity between their legs. Figure 7.1 shows an illustration of these vortices and other events at the serrated trailing-edge of a NACA 0012.

Large coherent structures appearing close to the trailing-edge or in between the serrations dominate in terms of vorticity level and clearly show the shape of hairpins or horseshoes. Most of these structures show a relatively large spanwise coherence. For instance, large horseshoe vortices, which appear relatively regularly at the frequency of the tonal noise, can posses spanwise extensions on the order of the distance between two individual serrations. A second mode of shedding shows smaller vortices which seem to be shed from the trailing-edge instead of originating from the space between the serrations. Both events are indicated in figure 7.1.

Surface pressure measurements underline the dominating effect of these horseshoe vortices

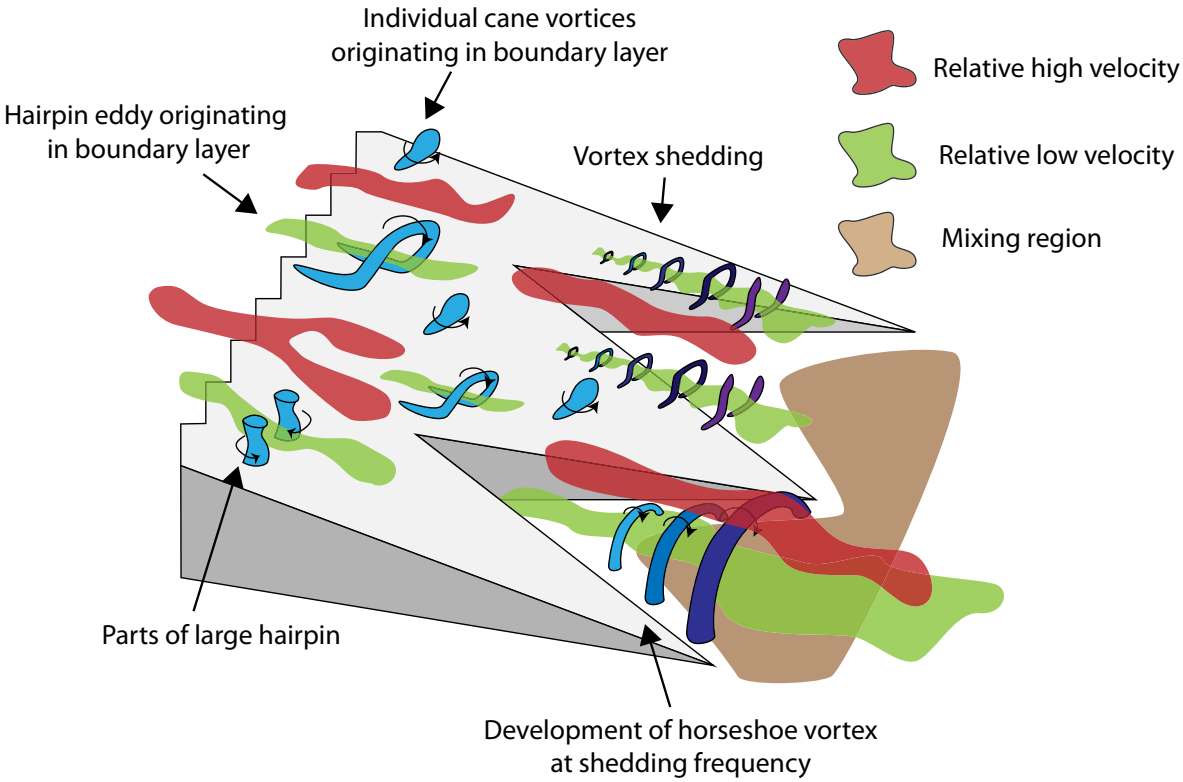

Figure 7.1: Coherent structures at the serrated trailing-edge of a NACA 0012

on the pressure spectrum upstream of the trailing-edge. The measured surface pressure fluctuations correlate to the wall-normal velocity with periodicity of the shedding frequency. Due to the domination of the pressure spectrum by these events, a reduction of the overall sound pressure level cannot be expected, since predictions are based solely on the convection of a turbulent boundary layer over the trailing-edge and blunt trailing-edge noise is not taken into account. The reduction in broadband noise might also be related to a redistribution of energy within the turbulence spectrum through shedding.

For the future, it might be of interest to focus research on the serrated flat plate attachments, which do not experience the penalty of generating additional blunt trailing-edge noise. Models for relating surface pressure spectra near the trailing-edge to the far-field noise exist. It may be worthwhile to investigate in how far information obtained through PIV measurements can replace the surface pressure spectra. Alternative formulations of the acoustic analogy are based on the velocity field and can be used to estimate the far-field noise. Their usability in combination with tomographic PIV has not been evaluated to date.

Bibliography

R. J. Adrian. Hairpin vortex organization in wall turbulence. *Physics of Fluids*, 19(4), 2007.

R. J. Adrian and Z. C. Liu. Observation of vortex packets in direct numerical simulation of fully turbulent channel flow. *Journal of Visualization*, 5(1):9–19, 2002.

R. J. Adrian, C. D. Meinhart, and C. D. Tomkins. Vortex organization in the outer region of the turbulent boundary layer. *Journal of Fluid Mechanics*, 422(1):1–54, 2000.

W. K. Blake. *Mechanics of flow-induced sound and vibration, complex flow-structure interactions (Applied Mathematics and Mechanics, vol 17)*. Academic Press, first edition, 1986.

A. J. Bohn. Edge noise attenuation by porous-edge extensions. AIAA Paper 76-0080, 1976.

K. A. Braun, N. J. C. M. van der Borg, A. G. M. Dassen, A. Gordner, and R. Parchen. Noise reduction by using serrated trailing edges. European wind energy conference, Dublin, 1997.

K. A. Braun, N. J. C. M. van der Borg, A. G. M. Dassen, F. Doorenspleet, A. Gordner, J. Ocker, and R. Parchen. Serrated trailing edge noise. European wind energy conference, Nice, March 1999.

M. K. Bull. Wall-pressure fluctuations beneath turbulent boundary layers: Some reflections on forty years of research. *Journal of Sound and Vibration*, 190(3):299–315, 1996.

D. M. Chase. The character of the turbulent wall pressure spectrum at subconvective wavenumbers and a suggested comprehensive model. *Journal of Sound and Vibration*, 112:125–147, 1987.

M. S. Chong, A. E. Perry, and B. J. Cantwell. A general classification of three-dimensional flow fields. *Physics of Fluids A*, 2(5):765–778, 1990.

T. Dassen, R. Parchen, J. Bruggeman, and F. Hagg. Results of a wind tunnel study on the reduction of airfoil self-noise by the application of serrated blade trailing edges. European Union Wind Energy Conference and Exhibition Gothenburg, May 1996.

W. Dobrzynski. Almost 40 years of airframe noise research: What did we achieve? *Journal of Aircraft*, 47(2):353–367, March 2010.

G. E. Elsinga. *Tomographic particle image velocimetry and its application to turbulent boundary layers*. PhD thesis, Delft University of Technology, 2008.

J. E. Ffowcs Williams and L. H. Hall. Aerodynamic sound generation by turbulent flow in the vicinity of a scattering half plane. *Journal of Fluid Mechanics*, 40:657–670, 1970.

M. R. Fink. Model tests of airframe noise reduction concepts. AIAA Paper 80-0979, 1980.

M. Gruber, P. Joseph, and T. Chong. Experimental investigation of airfoil self noise and turbulent wake reduction by the use of trailing edge serrations. 16th AIAA/CEAS Aeroacoustics Conference, Stockholm, June 2010.

M. R. Head and P. Bandyopadhyay. New aspects of turbulent boundary-layer structure. *Journal of Fluid Mechanics*, 107:297–338, 1981.

M. Herr and W. Dobrzynski. Experimental investigations in low-noise trailing-edge design. *AIAA JOURNAL*, 43(6):1167–1175, June 2005.

M. S. Howe. *Theory of Vortex Sound*. Cambridge University Press, first edition, 2003.

M. S. Howe. A review of the theory of trailing edge noise. *Journal of Sound and Vibration*, 61(3):437–465, 1978.

M. S. Howe. Aerodynamic noise of a serrated trailing edge. *Journal of Fluids and Structures*, 5:33–45, 1991a.

M. S. Howe. Noise produced by a sawtooth trailing edge. *Journal of the Acoustic Society of America*, 90(1):482–487, 1991b.

M. S. Howe. *Acoustics of fluid-structure interactions*. Cambridge University Press, first edition, 1998.

J. C. R. Hunt, A. A. Wraya, and P. Moin. Eddies, stream, and convergence zones in turbulent flows. Center for Turbulence Research Report CTR-S88, p. 193, 1988.

J. Jeong and F. Hussain. On the identification of a vortex. *Journal of Fluid Mechanics*, 285: 69–94, 1995.

L. Jones and R. Sandberg. Numerical investigation of airfoil self-noise reduction by addition of trailing-edge serrations. 16th AIAA/CEAS Aeroacoustics Conference, Stockholm, June 2010.

R. Lerch, G. Sessler, and D. Wolf. *Technische Akustik*. Springer Berlin Heidelberg, first edition, 2009.

M. J. Lighthill. Ueber eine besondere art der tonerregung. *Proceedings of the Royal Society A*, 211(1107):564–587, 1952.

K. Mau and W. Dobrzynski. Anordnung zur minderung des aerodynamischen lärms an einem vorflügel eines verkehrsflugzeuges. German Patent DE10157849A1, 2003.

S. Oerlemans. *Detection of aeroacoustic sound sources on aircraft and wind turbines*. PhD thesis, University of Twente, 2009.

S. Oerlemans, M. Fisher, T. Maeder, and K. Kögler. Reduction of wind turbine noise using optimized airfoils and trailing-edge serrations. 14th AIAA/CEAS Aeroacoustics Conference, May 2008.

S. B. Pope. *Turbulent flows*. Cambridge University Press, sixth printing edition, 2009.

A. Powell. On the aerodynamic noise of a rigid flat plate moving at zero incidence. *Journal of Sound and Vibration*, 31:1649–1653, 1959.

M. Raffel, C. E. Willert, S. T. Wereley, and J. Kompenhans. *Particle Image Velocimetry, a practical guide*. Springer Berlin Heidelberg, second edition, 2006.

S. W. Rienstra and A. Hirschberg. An introduction to acoustics. Lecture notes, Eindhoven University of Technology, 2004.

S. K. Robinson. Coherent motions in the turbulent boundary layer. *Annual Review of Fluid Mechanics*, 23:601–639, 1991.

M. Roger. Fundamentals of aeroacoustics. VKI Lecture Series 2009-03, Brussels, March 2009.

F. Scarano and P. Moore. An advection model to increase the time-resolution of piv time-series. 15th International Symposium on Applications of Laser Techniques to Fluid Mechanics, Lisbon, 2010.

A. Schröder, U. Dierksheide, J. Wolf, M. Herr, and J. Kompenhans. Investigation on trailing-edge noise sources by means of high-speed piv. 12th International Symposium on Applications of Laser Techniques to Fluid Mechanics, Lisbon, July 2004.

C. R. Smith and S. P. Metzler. The characteristics of low-speed streaks in the near-wall region of a turbulent boundary layer. *Journal of Fluid Mechanics*, 129:27–54, 1983.

C. R. Smith, G. K. Patterson, and J. L. Zakin. A synthesized model of the near-wall behavior in turbulent boundary layers. The 8th Symposium on Turbulence, Rolla, 1984.

V. Strouhal. Ueber eine besondere art der tonerregung. *Annalen der Physik und Chemie. Neue Folge*, V(10):216, 1878.

I. L. Ver. Noise of jet engine test cells. Jet Engine Test Cell Meeting, Naval Facilities Engineering Command, Alexandria, 1987.

F. M. White. *Viscous Fluid Flow*. McGraw-Hill International Edition, third edition, 2006.

J. C. Yu and C. K. W. Tam. An experimental investigation of the trailing edge noise mechanism. American Institute of Aeronautics and Astronautics Paper No. 77-1291, 1977.